MICROFLUIDIC TWO-PHASE BIOCHEMICAL REACITON SYSTEMS FOR DNA ANALYSIS

by

Fang Wang

A dissertation submitted in partial fulfillment
of the requirements for the degree of
Doctor of Philosophy
(Chemical Engineering)
in The University of Michigan
2010

Doctoral Committee:

Professor Mark A. Burns, Chair
Professor David T. Burke
Professor Ronald G. Larson
Professor Henry Yee-Neen Wang

To my parents and my husband

ACKNOWLEDGEMENTS

The moment that I have been waiting for more than five years finally comes. It is the time for me to sit down and acknowledge everyone who helped me through my Ph.D. First, I would like to offer my sincerest thanks and deepest appreciation to my advisor, Prof. Mark A. Burns. Mark has been a great mentor and guided me through my research projects. He provided extensive research freedom and opportunities. He has encouraged me whenever I had difficulties and felt frustrated during my studies. The discussions that I had with him are always inspiring and lead to the fine thoughts behind the experiment phenomena. His broad knowledge and kind personality have been the part of the driving force for me to move forward throughout my Ph.D. life both academically and personally.

Moreover, I would like to thank my dissertation committee members for their guidance and support through my dissertation. Prof. Ronald Larson is one of the most dedicated scientific researchers I have ever met. I also appreciate his generosity for letting me use the equipment in his lab so extensively. Prof. David Burke not only offered tremendous technical help on the reaction biochemistry, but also kept inspiring me by insightful discussions. I also want to thank Prof. Henry Wang for all the discussions in several different aspects of my dissertation.

I would like to extend my thanks to current and previous Burns research group members and a special thank you to Brian Johnson, our lead research engineer. Brian is

my go-to person, and he has helped me tremendously with fabrication, electronics and experimental set-ups. I would also like to thank previous research staffs in our group, Dylan, K.C., Ken, Zafar and Razi. They did such a great job in maintaining the clean room for the Burns group. Furthermore, I want to thank our previous group members, Ming, Rohit, Frank, Nimisha, Jen, Prasanna, Kyung, Minsoung, Papiya and Akshat, all of whom are great people. In addition, I extend my thanks to current members, Dustin, Sean, Jihyang, Ramsey, Irene and Eric for keeping such wonderful group dynamic and making my life at graduate school so enjoyable. I will sincerely miss the time we spent together in the lab and office.

Furthermore, my appreciation goes to the people in LNF, especially Greg, Matt, Ning and Onnop for their assistance in the area of fabrication. They have taught me many knowledge and skills unattainable through regular classes, and their help has expedited my processes.

My thanks are also extended to friends from other research groups, especially Abhishek and SungJin. Abhi has always been a good listener when I felt depressed and wanted to talk to someone. I also enjoyed working with SungJin, and appreciate his help on my research projects.

I would like to thank all the departmental staffs, especially Susan Hamlin, Connie Bacus, Jane Wiesner, Clair O'Connor, Shelley Fellers, Harald Eberhart and Mike Africa for their constant help.

I would like to thank my Chinese folks in the CSG-ChE group, especially Hongliang, Fan, Zuowei, Zhicheng, Xiaoyin, Xue, Zhenyu, Yu, Hao, Jie, Gang, Hui, Keliang, Mengnan and Shanpeng. I also want to thank some of my Chinese friends who

have left Ann Arbor, Jianli, Lin, Guangjun, Bei and Qiang. We had so many interesting lunch discussions and wonderful activities. They have brought so much joy and lovely warmth to my life at Ann Arbor.

I want to give my special thanks to Li Xu, who has been my best friend for the past five years. To me, she is also like my sister. She is always there for me whenever I need her. I could not be more lucky and blessed to have such a wonderful friend.

I would like to thank my parents and my brother. They have always believed in me and offered unconditional backing. I would also like to thank my in-laws who have always desired my success and happiness.

Finally, I thank my dearest husband, Weixian, for his continued love and support, and for being the greatest part of my life.

TABLE OF CONTENTS

LIST OF FIGURES

LIST OF TABLES

CHAPTER 1

INTRODUCTION

Motivation

As the starting point for many molecular biology procedures, DNA analysis has been applied in a variety of fields, including genetic diagnostics and therapy, agriculture and food engineering, forensic identification, energy production as well as environmental monitoring and remediation. Technologies and resources generated by the Human Genome Project (HGP) and other genomics research further boost the demand of DNA analysis. Besides the research and scientific benefits, the profit brought by the DNA-based analytical technologies and products are projected to exceed $45 billion by 2009[1].

DNA analysis involves different types of biochemical reactions such as DNA amplification (*i.e.*, polymerase chain reaction (PCR)), restriction digestion, ligation and hybridization, with basic procedures such as preparation of sample and reagent mixture as well as control of temperature profile. Traditionally, these reactions are carried out in benchtop instruments, which requires large lab space, long turnaround time and intensive labor. Although the reaction volume, which is usually in the range of tens of microliters, is much smaller than most chemical reactions, the consumption of sample and reagents remains rather high, considering the application of DNA analysis in the high throughput format and the unavoidable sample loss during sample preparation. These limitations in

the conventional platforms continue to post challenges in achieving rapid and inexpensive DNA analyses for their wide disseminated applications.

With the advances in microfluidics and microfabrication technology, micro total analysis (μ-TAS), also known as "lab-on-a-chip", was proposed in early 1990s[2], and has been enthusiastically embraced by researchers wishing to miniaturize the entire DNA analysis process from benchtop instruments onto microfluidic devices. In the miniaturized device, the reaction volume can be easily reduced to nanoliter or even less, thus reducing the consumption of samples and reagents. Temperature control in the reactions can also benefit from the small thermal mass of the microdevices to achieve fast heat transfer and shorter reaction time. Moreover, using microfabrication techniques, the microsystems integrated with all the DNA analysis components can be produced massively, thus reducing the manufacture cost and making the systems more amenable for point-of-care testings.

Because of the critical role of biochemical reactions in DNA analysis, major efforts were first spent on developing bioreaction microdevices. Among all those reactions, PCR in a microfluidic platform draws most of the interests, because PCR is the key step in many DNA-based analyses and can also be readily complemented with various molecular biology formats. A number of PCR microsystems have been developed with two major formats: batch-based systems where the reaction mixture remains in the stationary chamber during temperature cycling[3-4]; continuous-flow-based systems where the reaction mixture flows through different temperature zones with the hold time at each temperature step controlled by the flow rates[5-6]. Researchers have also been working on integrating PCR with other analysis components such as sample preparation, fluid

handling and product detection in microsystems in order to extract genetic information from raw biological samples efficiently, conveniently and inexpensively[7-10].

However, there are also some technical challenges to be faced in the miniaturized systems, mainly stemming from the micro format itself. The surface-to-volume (S/V) ratio of a microsystem is much higher than that of a benchtop instrument. Because of the high S/V ratio, the adsorption on the device surface could cause a significant amount of reagent and sample loss, and cross-contamination that affects the analysis sensitivity and efficiency[11-13]. Moreover, dispersion in the microsystems due to either the low Reynolds number or the parabolic velocity profile could lead to dilution and cross-contamination of the reagents and samples. Evaporation is another critical issue since most reactions in DNA analysis require high temperature. Without any sealing strategies, the evaporation loss could reach 40% to 100% of the reaction volume, given that the initial reaction volume is already very small (in nanoliters or less)[14]. A variety of sealing agents and microvalves have been used to reduce or prevent evaporation, but they also increase the complexity of fabrication and operation especially for the integrated systems[7, 15-19].

In the past decade, two immiscible liquid phases in droplet format (*i.e.*, one liquid phase (the dispersed phase) is encapsulated in the other liquid phase (the continuous phase)) has aroused increasingly interest in microfluidics field. Traditionally, droplets are generated by directly agitating the immiscible fluids, but the droplets tend to aggregate in bulk and the size of the droplets is not uniform[20-21]. In a microfluidic platform, the droplet size and generation frequency can be well controlled by adjusting the channel geometry and fluid flow rates[22-23] or using electrohydrodynamic (EHD) approaches such as electrowetting-on-dielectric (EWOD)[24] and dielectrophoresis (DEP)[25]. Moreover, droplet

manipulations including merging, splitting, sorting and mixing, can be achieved more controllably and easily in microsystems because of the deterministic nature of the microfluidic flow and the driving source for the flow[26-30].

Combining the fluidic elements for droplet generation and manipulation, droplet microfluidics offers great advantages in carrying out chemical and biochemical reactions. In a droplet-based microsystem, individual droplets function as separate microreactors with well-controlled reaction volume ranging from micro- to femtoliter. The continuous phase surrounding the droplets provides easy and clean transportation of the reaction solution, prevents cross talking between the adjacent droplets and the solute adsorption onto the channel surfaces. Moreover, dispersion can be significantly reduced and mixing of reagents can be completed much faster in the droplets. While using aqueous-in-oil droplets, the continuous oil phase also prevents the evaporation loss during high temperature reactions.

The microfluidic droplet-based systems have been applied to a number of reactions and assays. Nanoparticle synthesis is one of the most demonstrated chemical applications[31,32]. The droplet-based microsystem has also been proposed for the kinetic studies of the chemical synthesis, taking advantage of the easy droplet manipulation and transportation[32]. Biological applications such as cell cultivation and analysis[33], protein expression[34], DNA/RNA amplification[35], and biological fluid assays[36] have been implemented in the droplet-based microsystems. Since the droplet size and generation frequency as well as the compositions within the droplets can be well controlled, the droplet-based microsystem is also ideal for conducting high throughput screening and analysis. In fact, the system has been used to screen the conditions for protein

crystallization[37]. Moreover, in nature, chemical and biological operations are carried out in micron-sized spaces such as cells and their organelles. The size of droplets generated in microsystems can easily go down to pico- to femtoliter, so these droplets can be used to mimic in *vivo* reactions and molecular processes. For example, molecular evolution has been studied with droplets serving as cell-like compartments[38].

Although so far major efforts on the application of droplet-based microsystems have been focused on using multiple monodisperse pico- to femtoliter sized droplets, there are limitations with such small droplets like non-uniform encapsulation and lack of products for downstream processes if needed. On the contrary, some applications do require larger (nano- to microliter) droplets. For example, in many DNA-based diagnoses, the concentration of target molecules in patient samples is often very low (less than 10^6 copies/mL). It is not practical to conduct such assays using small droplets since only thousands or even millions of droplets will contain one target molecule. Moreover, very few studies have been done on characterizing the performance of the droplet-based chemical and biochemical reactions, and indeed the reaction parameters may need to be adjusted from those used in the single-liquid-phase microreactions. Relying on controllable droplet merging, splitting and mixing, the droplet microfluidics provides a perfect platform for complex and integrated analyses (*e.g.*, multi-step reactions involved in many DNA analyses), with no partition components such as microvalves required. Moreover, the droplet generation and manipulation are mostly controlled manually by monitoring the fluid flow with certain type of imaging technique, so the system operation relies on cumbersome and expensive accessory instruments. Integrating liquid monitoring components into the droplet-based microsystem not only can simply the system setup and

operation, but also provides the capability of system automation, thus making the microsystem perform more efficiently and more user-friendly towards the ultimate goal of point-of-care analysis and diagnosis.

Organization of the dissertation

The goal of this dissertation is to investigate and develop techniques to improve the performance of biochemical microreactions and simplify the fabrication and operation of the microsystems. In Chapter 2 we presented microfluidic valveless devices that reduce evaporative loss during single-liquid-phase thermal bioreactions by relying on the principle of diffusion-limited evaporation. Both theoretical and experimental results demonstrate that the sample evaporative loss can be reduced by more than 20 times using long narrow diffusion channels on both sides of the reaction region. The driving force for liquid evaporation is reduced to further suppress the evaporation by two additional techniques: decreasing the interfacial temperature using thermal isolation and reducing the vapor concentration gradient by replenishing water vapor in the diffusion channels. Both thermal isolation and vapor replenishment techniques can limit the sample evaporative loss to approximately 1% of the reaction content.

In Chapter 3 we characterized the performance of PCR in a microfluidic two-liquid-phase device. Aqueous-in-oil droplets with a volume range of 5-250nL can be formed on-chip reproducibly, and PCR in the droplets shows amplification efficiencies comparable to benchtop reactions with no evaporation loss. A higher polymerase concentration is required in the reaction droplet while the optimal Magnesium ion

concentration is the same for both on-chip and benchtop systems. The optimal hold time is 9 and 30 seconds for denaturation and annealing/extension in thermal cycling, respectively. No clear trend has been found for the relationship between the amplification yield and the droplet size because of the possible reagent adsorption on the chamber walls or the liquid-liquid interface. The droplet-based PCR can also be monitored in real time with FRET probes, and provide amplification with a cycle threshold of ~10 cycles earlier than the benchtop instruments.

In Chapter 4 we developed a droplet-based bioreaction microsystem with automated droplet generation and confinement. On-chip electronic sensing is employed to track the position of the droplets by sensing the oil/aqueous interface in real time. The sensing signal is also used to control the pneumatic supply for moving as well as automatically generating four different nanoliter-sized droplets. The actual droplet size is very close to the designed droplet size with a standard deviation less than 3% of the droplet size, and the droplet generation can be 5 times faster than in manual operation. Droplets can also be automatically confined in the reaction region with feedback pneumatic control and digital or analog sensing. As an example bioreaction, PCR has been successfully performed in the automated generated droplets. Although the amplification yield was reduced with the droplet confinement, especially while using the analog sensing method, adding additional reagents effectively alleviated this inhibition.

In Chapter 5 we used a droplet-based microfluidic platform to perform on-chip droplet generation, merging and mixing for applications in multi-step reactions. Submicroliter-sized droplets can be produced separately from three identical droplet-generation channels and merged together in a single chamber. Three different mixing

strategies were used for mixing the merged droplet. For pure diffusion, the reagents were mixed in approximately 10 minutes. Using flow around the stationary droplet to induce circulatory flow within the droplet, the mixing time was decreased to approximately one minute. The shortest mixing time (10 sec) was obtained with bidirectional droplet motion between the chamber and channel, and optimization could result in a total time of under one second. We also tested this on-chip droplet generation and manipulation platform using a two-step thermalcycled bioreaction: nested TaqMan® PCR. With the same concentration of template DNA, nested TaqMan® PCR in a well-mixed merged droplet shows a cycle threshold of ~6 cycles earlier than that in the diffusively mixed droplet, and ~40 cycles earlier than the droplet-based regular (single-step) TaqMan® PCR.

Although the studies presented in this dissertation are based on different two-phase (*i.e.*, air-liquid or liquid-liquid) microsystems, through these studies, useful means have been provided to improve the performance of biochemical microreactions with simplified system fabrication and operation. In air-liquid based microsystems, the valveless strategies have offered the capability of reducing the evaporation loss and the complexity of device fabrication and operation. In liquid-liquid (aqueous-in-oil droplets) based microsystems, the characterization studies have specifically addressed the dependence of the reaction efficiency on the key droplet-based reaction parameters; the automation of the droplet-based microsystems relying on electronic sensing have improved the efficiency and robustness of the microsystem operation; the combination of droplet generation, merging and mixing in the microsystem has demonstrated its application for two-step biochemical reactions, facilitating the miniaturization of more complex and integrated DNA analysis in a simple microfluidic platform.

References

1. Consulting Resources Corporation *Newletter*, Spring 1999.
2. A. Manz, N. Graber and H. M. Widlmer, *Sens. Actuator B-Chem.*, 1990, **1**, 244-248.
3. A. T. Woolley, D. Hadley, P. Landre, A. J. DeMello, R. A. Mathies and M. A. Northrup, *Anal. Chem.*, 1996, **68**, 4081-4086.
4. P. Wilding, M. A. Shoffner and L. J. Kricka, *Clin. Chem.*, 1994, **40**, 1815-1818.
5. M. U. Kopp, A. J. De Mello and A. Manz, *Science*, 1998, **280**, 1046-1048.
6. M. Hashimoto, M. L. Hupert, M. C. Murphy and S. A. Soper, *Anal. Chem.*, 2005, **77**, 3243-3255.
7. R. Pal, M. Yang, R. Lin, B. N. Johnson, N. Srivastava, S. Z. Razzacki, K. J. Chomistek, D. Heldsinger, R. M. Haque, V. M. Ugaz, P. Thwar, Z. Chen, K. Alfano, M. Yim, M. Krishnan, A. O. Fuller, R. G. Larson, D. T. Burke, and M. A. Burns, *Lab Chip*, 2005, **5**, 1024-1032.
8. R. G. Blazej, P. Kumaresan and R. A. Mathies, *Proc. Natl. Acad. Sci. U.S.A.*, 2006, **103**, 7240-7245.
9. P. Liu, T. S. Seo, N. Beyor, K.-J. Shin, J. R. Scherer and R. A. Mathies, *Anal. Chem.*, 2007, **79**, 1881-1889.
10. N. Thaitrong, N. M. Toriello, N. D. Bueno and R. A. Mathies, *Anal. Chem.*, 2009, **81**, 1371-1377.
11. M. A. Shoffner, J. Cheng, G. E. Hvichia, L. J. Kricka and P. Wilding, *Nuclei Acids Research,* 1996, **24**, 375-379.

12. R. A. M. Receveur, F. W. Lindermans and N. F. de Rooij, *J. Micromech. Microeng.,* 2007, **17**, R50-R80.

13. M. Krishnan, D. T. Burke and M. A. Burns, *Anal. Chem.*, 2004, **76**, 6588-6593.

14. F. Wang, M. Yang and M. A. Burns, *Lab Chip*, 2008, **8**, 88-97.

15. L. C. Waters, S. C. Jacobson, N. Kroutchinina, J. Khandurina, R. S. Foote and J. M. Ramsey, *Anal. Chem.*, 1998, **70**, 158.

16. C. G. Koh, W. Tan, M. Q. Zhao, A. J. Ricco and Z. H. Fan, *Anal. Chem.*, 2003, **75**, 4591-4598.

17. D. S. Yoon, Y. S. Lee, Y. Lee, H. J. Cho, S. W. Sung, K. W. Oh, J. Cha and G. Lim, *J. Micromech. Microeng.*, 2002, **12**, 813.

18. T. Thorsen, S. J. Maerkl, S. R. Quake, *Science*, 2002, **298**, 580.

19. R. Pal, M. Yang, B. N. Johnson, D. T. Burke and M. A. Burns, *Anal. Chem.*, 2004, **76**, 3740.

20. J. Komatsu, S. Matsuura, K. Takashima, S. Katsura and A. Mizuno, *J. Biotechnol.*, 2003, **102**, 117-124.

21. M. Nakano, N. Nakai, H. Kurita, J. Komatsu, K. Takashima, S. Katsura, and A. Mizuno, *J. Biosci. Bioeng.*, 2005, **99**, 293-295.

22. T. Thorsen, R. W. Roberts, F. H. Arnold and S. R. Quake, *Phys. Rev. Lett.*, 2001, **86**, 4163-4166.

23. S. L. Anna, N. Bontoux, and H. A. Stone, *Appl. Phys. Lett.*, 2003, **82**, 364-366.

24. M. G. Pollack, R. B. Fair and A. D. Shenderov, *Appl. Phys. Lett.*, 2000, **77**, 1725-1726.

25. T. B. Jones, *J. Electrost.*, 2001, **51-52**, 290-299.

26. D. R. Link, S. L. Anna, D. A. Weitz and H. A. Stone, *Phys. Rev. Lett.*, 2004, **92**, 054503-1-054503-4.

27. F. Sarrazin, L. Prat, N. D. Miceli, G. Cristobal, D. R. Link and D. A. Weitiz, *Chem. Eng. Sci.*, 2007, **62**, 1042-1048.

28. X. Niu, S. Gulati, J. B. Edel, and A. J. deMello, *Lab Chip*, 2008, **8**, 1837-1841.

29. M. R. Bringer, C. J. Gerdts, H. Song, J. D. Tice and R. F. Ismagilov, *Phil. Trans. R. Soc. Lond.* A, 2004, **362**, 1087-1104.

30. D. R. Link, E. Grasland-Mongrain, A. Duri, F. Sarrazin, Z. Cheng, G. Cristobal, M. Marquez and D. A. Weitz, *Angew. Chem. Int. Ed.*, 2006, **45**, 2556-2560.

31. L.-H. Hung, K. M. Choi, W.-Y. Tseng, Y.-C. Tan, K. J. Shea and A. P. Lee, *Lab Chip*, 2006, **6**, 174-178.

32. I. Shestopalov, J. D. Tice and R. F. Ismagilov, *Lab Chip*, 2004, **4**, 316-321.

33. M. He, J. S. Edgar, G. D. M. Jeffries, R. M. Lorenz, J. P. Shelby and D. T. Chiu, *Anal. Chem.*, 2005, **77**, 1539-1544.

34. A. Huebner, M. Srisa-Art, D. Holt, C. Abell, F. Hollfelder, A. J. deMello and J. B. Edel, *Chem. Commun.*, 2007, 1218-1220.

35. N. R. Beer, B. J. Hindson, E. K. Wheeler, S. B. Hall, K. A. Rose, I. M. Kennedy and B. W. Colston, *Anal. Chem.*, 2007, **79**, 8471-8475.

36. V. Srinivasan, V. K. Pamula and R.B. Fair, *Lab Chip*, 2004, **4**, 310-315.

37. B. Zheng, J. D. Tice, S. Roach and R. F. Ismagilov, *Angew. Chem. Int. Ed.*, 2004, **43**, 2508-2511.

38. P. S. Dittrich, M. Jahnz and P. Schwille, *ChemBioChem.*, 2005, **6**, 811-814.

CHAPTER 2

MICROFABRICATED VALVELESS DEVICES FOR THERMAL BIOREACTIONS BASED ON DIFFUSION-LIMITED EVAPORATION

Introduction

Many reactions used for biochemical analysis are temperature-controlled and require relative high operating temperatures. One of the most well known thermal reactions is the polymerase chain reaction (PCR), an enzyme-catalyzed DNA amplification cycles through three different temperatures (denaturation (~94^{o}C), annealing (~55^{o}C) and extension (~72^{o}C)). Sanger cycle sequencing is another thermocycling reaction (~95^{o}C, ~55^{o}C, ~60^{o}C) that utilizes the termination function of dideoxynucleotide triphosphates (ddNTPs) on DNA chain enlongation.[1] Ligase chain reaction (LCR) and ligase detection reaction (LDR), techniques used to detect single base mutations, both require elevated temperatures. [2] Restriction of DNA strands into shorter fragments for DNA analysis is an isothermal reaction but still requires temperatures up to ~75^{o}C. Traditionally, these biochemical assays have been carried out in bench-top equipment (*e.g.*, themocyclers) and, although there are many potential applications, the techniques have not been widely disseminated, particularly for point-of-care applications.

In recent years, microfabrication technologies have paved the way for the development of rapid and inexpensive bioreaction systems. A miniaturized bioreaction

system presents several advantages over the bench-top equivalent: reduced reagent, labor and equipment costs, decreased reaction time, reduced risk of contamination, and simplified sample handling. There are two major types of miniaturized bioreaction systems: batch-based systems where the stationary reaction solution is heated or thermocycled inside a reaction chamber by either external heaters [3-16] or integrated on-chip heaters, [17-24] and continuous flow-based systems where the sample flows through certain temperature zones with well-defined flow rates. [25-30] Other novel approaches, such as on-chip rotary reaction, [31] noncontact infrared-mediated reaction, [32-34] electrokinetically synchronized reaction, [35] electrowetting-based reaction [36] and Rayleigh-Bénard convection-based reaction [37,38] have also been reported. Recent trends in miniaturized bioreaction systems are to integrate bioreactions with sample preparation, fluidic handling, and product detection to produce systems that can rapidly, conveniently, and economically extract information from raw biological samples with greatly reduced cost. [4,7,11,12,17-20,23,39]

One technical challenge in miniaturizing bioreaction systems is preventing or reducing evaporative loss during thermocycling. Although mineral oils, [4-16,10,26] adhesive tapes [19,22] and silicone rubber gaskets [21] have all been used in miniaturized bioreaction devices, most integrated systems reported so far have used microvalves to prevent evaporative loss. These microvalves seal the reaction chamber using pneumatically or mechanically actuated diaphragms, [7-9,11,15,17-18,40-43] thermally actuated phase-change pistons, [12,19,39,44] or polyacrylamide gels.[19] Because all microvalves need to provide some kind of physical confinement and most require some kind of actuations to operate, they often add complexity to the microfabrication and fluidic operations. In addition, simple

microfluidic assays are often open or unsealed systems to allow the introduction and/or the withdrawal of fluids. Therefore, a simple technique to reduce the evaporative loss without valves is highly desirable for microfluidic reaction systems.

We have fabricated microfluidic devices that use diffusion-limited evaporation mechanisms to suppress liquid loss during thermal reactions. Eliminating the use of microvalves, oil or gaskets, the basic design uses long narrow diffusion channels in the fluidic network to slow down the diffusion of water vapor through the channel openings. The vapor evaporation rate can be further reduced by decreasing the driving force for liquid evaporation. This reduction is achieved either by decreasing the sample interfacial pressure using thermal isolation or by decreasing the vapor concentration gradient using vapor replenishment.

Theory and Design principles

The principle of valveless reaction devices is based on the concept of diffusion-limited evaporation. In the design, the input and output channels to the heated reaction chamber provide a resistance that decreases the evaporation rate from the reaction fluid (see Figure 2.1(a)). Vapor that evaporates from the reaction solution meniscus must diffuse through the microchannels before it can escape through sample loading holes into the ambient environment. The evaporation rate is limited by this vapor diffusion rate since the phase change at the liquid surface (*i.e.*, liquid to vapor) is quite rapid and there is no convective flow of air in the channel.

The diffusion-limited evaporation rate can be evaluated using mass transfer equations. At any given time, there is a vapor-pressure gradient along the diffusion path, from the equilibrium interfacial vapor pressure at the liquid meniscus to the ambient vapor pressure at the outlets. As evaporation proceeds, the sample interface recedes in the channel, resulting in an increased diffusion length over time. According to Fick's law, the total diffusion flux of vapor N_A in the channel (in the x direction) is determined by

$$N_A = -\frac{PD_v}{RT(1-y)}\frac{dy}{dx}, \tag{2.1}$$

where P is the total pressure; y is the mole fraction of vapor ($y = \frac{p_A}{P}$ and p_A is the partial vapor pressure); D_v is vapor diffusivity in air; T is liquid interfacial temperature; and R is the ideal gas constant. Integrating equation (2.1), we obtain the total diffusion flux of vapor at any given moment,

$$N_A = \frac{PD_v}{RTx}\ln\frac{P-p_v}{P-p_0}, \tag{2.2}$$

where x is the diffusion length (*i.e.*, the distance between the sample interface and the loading holes); p_0 and p_v are the ambient and sample interfacial vapor pressures, respectively. Assuming a pseudo-steady-state condition (*i.e.*, the sample interface recedes slowly), the diffusion flux also equals the amount of water leaving the liquid meniscus,

$$N_A = \frac{\rho_w}{M_w}\frac{dx}{dt}, \tag{2.3}$$

where M_w and $\rho_w$are the molecular weight and density of water, respectively. Combining equation (2.2) and (2.3), and integrating from $t = 0$ to $t = t_F$, we obtain the

distance from the sample interface to the sample access hole as a function of time at a constant temperature:

$$x_F^2 - x_0^2 = \frac{2PM_w D_v t_F}{\rho_w R T_i} \ln\left(\frac{P - p_0}{P - p_v}\right), \tag{2.4}$$

where x_0, x_F are the initial and final diffusion lengths, respectively; T_i is sample interfacial temperature; and t_F is the reaction time.

For a thermocycling reaction, equation (2.4) must be modified to include periodically changed sample interfacial temperatures, T_i, and reaction time, t_F. The vapor pressure, p_v, and vapor diffusivity, D_v, also need to be changed periodically because they are temperature dependent. [45,46] For example, three sets of T_i, p_v, t_F and D_v are needed for PCR that consists of three-step thermocycling. The total evaporative volume loss during a three-step thermocycling reaction, V_{loss}, is then calculated using equation (2.5),

$$V_{loss} = 2A_c\left(x_F - x_0\right) = 2A_c\left(\sqrt{n\sum_{j=1}^{3}\frac{2PM_w D_{vj} t_{Fj}}{\rho_w R T_{ij}} \ln\left(\frac{P - p_0}{P - p_{vj}}\right) + x_0^2} - x_0\right), \tag{2.5}$$

where T_{ij}, p_{vj}, t_{Fj} and D_{vj} are the sample interfacial temperature, vapor pressure, reaction time and vapor diffusivity at different thermocycling steps, respectively; n is the number of cycles; and A_c is the cross-section area of the diffusion channel. In this equation, variables such as t_{Fj}, n, M_w and ρ_w are determined by the reaction protocols, and p_0 is negligible compared to the atmosphere pressure P. Therefore, the variables that we can adjust to reduce V_{loss} in the microfabricated devices are the initial diffusion length x_0 that is associated with the channel length L, the channel cross-section area A_c, and the

sample interfacial temperature T_{ij}. The temperature near the sample interface also determines the interfacial vapor pressure p_{vj} and the vapor diffusivity D_{vj}.

Materials and Methods

Device design and fabrication

The long-armed device with thermal isolation contains a 4mm long, 2mm wide and 100μm deep reaction chamber with a rough volume of 800nL, and two 1cm long, 200μm wide and 20μm deep channels connected to the reaction chamber. The reaction chamber is surrounded by a 1μm thick and 1mm wide silicon nitride diaphragm. The device with vapor replenishment consists of a serpentine reaction channel (designed volume of 500nL) with two 5mm long and 100μm wide straight channels on either end. All channels in this device are 50μm deep except that there are two 150μm deep liquid stop structures near the T-junctions in the water channels.

The devices are assembled by bonding silicon and glass substrate components. The fluid networks are fabricated in a glass wafer using two photolithography and two-step wet chemical etching due to the non-uniform depth. The detailed procedure for photolithography and wet etching have been outlined elsewhere.[32] In the fabrication process of the thermally isolated long-armed device, the first lithography is carried out to only pattern the deeper features (*i.e.*, the reaction chamber), followed by etching away the exposed metal film. The remaining photoresist is then stripped away. The second lithography is carried out to pattern the whole fluid network. The glass wafer is then etched to generate the reaction chamber with a depth of 80μm in hydrofluoric acid (49%,

CMOS grade; J.T.Baker, Philipsburg, NJ). After removing the metal film that protects the channels, the second glass etching is conducted to an additional depth of 20μm. Then the remaining photoresist and metal film are removed. The fabrication of fluid network in the vapor-replenished device follows a similar procedure, except that the etching depth in each etching step is different according to the design. Sample access holes are drilled by a homemade electrochemical discharge drilling system. Finally, the glass wafer is coated with 5μm parylene in a parylene coating system (PDS-2010 LABCOTER®2, SCS Cookson Electronics, Indianapolis, IN), and diced to yield the individual devices.

Silicon fabrication process of the vapor-replenished device is the same as described in previous work.[38] Silicon fabrication of the thermally isolated long-armed device begins with depositing a 1μm thick low stress silicon nitride on a silicon wafer (<100>, 500μm thick) by low pressure chemical vapor deposition (LPCVD). The lithography and liftoff for the heaters and sensors have also been described in previous work.[38] To thermally isolate the reaction chamber, another lithography is carried out on the backside of the silicon wafer. The exposed silicon nitride layer is then removed by CF_4/CHF_3 plasma RIE process. Next, a deep reactive ion etching (DRIE) process is carried out to selectively remove the silicon substrate and thus obtain a 1μm thick silicon nitride diaphragm.

The procedure to assemble the glass-silicon device has also been described in detail elsewhere.[38] Briefly, Individual silicon devices are fixed on the custom designed printed circuit board (PCB, Advanced Circuits, Aurora, CO), and then wire bonded (Kulicke & Soffa 4124 Ball Bonder) using 1.0 mil gold wire. Next, the assembly is coated with 5μm parylene. The silicon and glass components are visually aligned and

then bonded using UV curable optical glue. Finally, the wirebonds are encapsulated with a non-fluorescent epoxy (EP939; Thermoset, Indianapolis, IN).

Instrumentation

The setup for reaction temperature control consists of a DC power supply (B+K Precision Model 1760, Yorba Linda, CA), two data acquisition (DAQ) boards (National instruments PCI 6031E and PCI-6704, Austin, TX), two connector blocks (National instruments SCB-100 and SCB-68, Austin, TX), a signal conditioning circuit, a computer and two LabVIEW programs (National instruments, Austin, TX). The temperature sensors are calibrated by heating the device in a convection oven and recording the temperature-resistance data in a LabVIEW program. The slope and intercept from a linear fit of the temperature and resistance data is read into the control algorithms that use a proportional-integral (PI) module to control temperature. The heaters are connected to the power supply through the signal conditioning circuit that boosts the supply voltage from the computer with an op-amp gain of 3. During the experiments, the device is placed on a copper block that sits on a probe station chuck at room temperature. Lab air supply, controlled by a pressure regulator (Matheson Gas Products Inc, Irving, TX, Model Number 3701), provides the pneumatic pressure used for fluidic operations.

PCR amplification and analysis

PCR amplification of the Influenza viral strain A/LA/1/87 DNA samples is performed on the devices. The hemaggultinin gene (HA1) region of influenza viral RNA is reverse transcribed, amplified, ligated into pGEM-T vector, and cloned into *E. coli*.

The cloned plasmid is used to synthesize RNA *in vitro* with T7 RNA polymerase. The RNA samples are then subject to reverse transcription to produce the DNA samples that are used in the device. The reaction mixture consists of 2ng/μL DNA template, 0.2mM each dNTP, 60mM Tris-HCl, 15mM NH_4SO_4, 1.5mM $MgCl_2$, 0.3mM each primer, and Taq DNA polymerase 50units/mL (Invitrogen, Carlsbad, CA). The sequences of forward and reverse primers are 5'-GTTTGTTTCTCTGGTACATTCCGC-3' and 5'-CAACTGTTACCCTTATGATGTGCC-3', respectively. A DNA fragment of 690bp is amplified. The thermocycling protocol used by the on-chip PCR consists of 30 cycles of 94°C for 5s, 55°C for 10s, 72°C for 20s, and 72°C for 30s after 30 cycles. The reaction solution is then collected and analyzed on a 1% agarose gel electrophoresis prestained with ethidium bromide.

Results and Discussions

Based on the principle of diffusion-limited evaporation, three approaches are proposed to reduce the sample evaporative loss in a microfluidic device during thermal reactions. First, long channels with small cross sections at both ends of a reaction chamber increase the diffusion path of the evaporated vapor, greatly reducing the vapor diffusion rate. Second, a thin silicon nitride diaphragm surrounding a reaction chamber thermally isolates the high-temperature reaction region from the rest of the device, significantly lowering the temperature and vapor pressure at the liquid interface as well as the driving force for evaporation. Third, a pure water meniscus, pinned at the edge of a deep pit that connects to the diffusion channel, is heated synchronously with the reaction

chamber to increase the vapor concentration in the diffusion channel and therefore decrease the concentration gradient (*i.e.*, the driving force for evaporation). Each of these techniques is described in the following sections.

Diffusion channel geometry and initial diffusion length

For thermal reactions in microfluidic systems such as PCR, evaporative loss can be significant compared to the reaction volume if valves or seals are not used. Figure 2.1(b) shows the evaporative loss (V_{loss}) during thermocycling as a function of the amount of liquid that is initially present in the reactor. For these experiments, we used a simple reactor design consisting of a straight channel with uniform cross-section area (Figure 2.1(a)). The evaporative loss is measured by heating the entire channel using the PCR protocol mentioned previously. As shown in Figure 2.1(b), the evaporative loss (V_{loss}) in a straight uniform channel during thermocycling (30 cycles of 94°C for 5s, 55°C for 10s, 72°C for 20s) is approximately 40% ~100% of the original reaction volume (V_{PCR}).

Using equation (2.5), we also calculated the relative sample evaporative loss (V_{loss}/V_{PCR}) in a uniform channel with different channel lengths (L) and initial diffusion lengths (x_0) when the channel is thermocycled. The temperatures used in the cycling, and the vapor pressure and diffusivity at different temperatures are listed in Table 1. The results in Figure 2.1(c) show that with the same fractional filled length ($(L-2x_0)/L$), the evaporative loss is reduced dramatically by increasing the channel length (*i.e.*, the length of the diffusion regions). For a certain percentage of sample evaporative loss, the optimal initial diffusion length and the minimal channel length can be determined using Figure

2.1(c). For example, to keep the evaporative loss to no more than 10%, the channel should be at least 4cm long with a fractional filled length of 0.5 (*i.e.*, x_0=1cm on both ends). The plot also indicates that in most cases, designing the channel so that the reaction solution fills it half way ($(L-2x_0)/L=0.5$) will result in less relative evaporative loss than if the channel is filled completely ($(L-2x_0)/L=1$) or hardly at all ($(L-2x_0)/L \le 0.1$). In fact, although the absolute value of evaporative loss is very small when the channel is almost empty, V_{loss}/V_{PCR} is still large due to the small initial reaction volume.

In addition to the channel length and initial diffusion length, the cross-section area of the channel also affects the V_{loss}/V_{PCR} ratio as predicted in Figure 2.1(d). In this calculation using equation (2.5), we divide the channel into three regions: a reaction region with the cross-section area A_r, and two diffusion regions on either end of the reaction region with the cross-section area A_c. The results show that the smaller the value of A_c/A_r is, the less the evaporative loss will be, implying that narrow diffusion channels with large reaction chambers are preferred. Note that actual evaporation rates may increase in narrow channels due to the increased extent of liquid film wetting on the channel wall.[48]

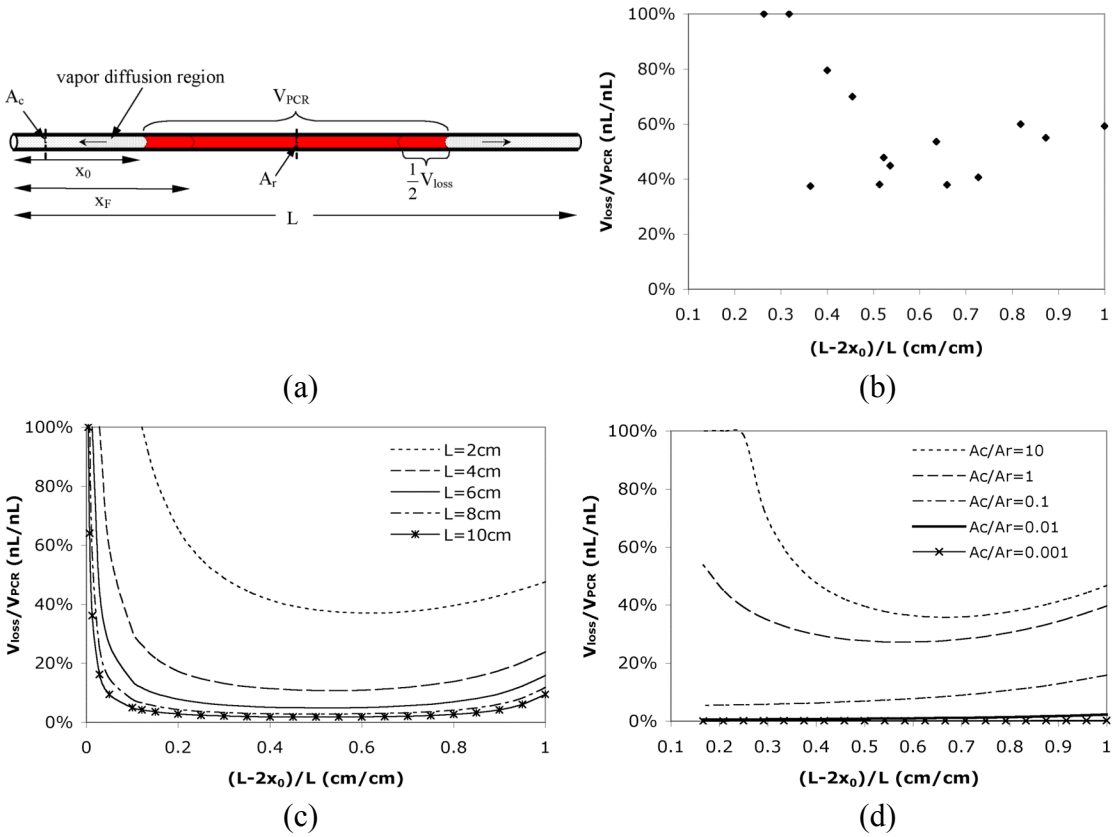

Figure 2.1 (a) Schematic of the simple reactor. x_0 is the initial diffusion length; x_F is the final diffusion length; A_c is the cross-section area of the diffusion path; A_r is the cross-section area of the reaction region; L is the total length of the channel. (b) Experimental relative evaporative loss V_{loss}/V_{PCR} in a 2cm straight uniform channel with varying fractional filled length $(L-2x_0)/L$. (c) Calculated relative evaporative loss V_{loss}/V_{PCR} in a straight uniform channel with different channel length. (d) Calculated relative evaporative loss V_{loss}/V_{PCR} in a channel-chamber-channel design with different cross-section area ratio A_c/A_r. The total length of the channels and chamber is 2.4cm and the reaction chamber is 0.4cm long.

Driving force for liquid evaporation

Thermal isolation

In addition to controlling the design geometry, the evaporative loss can be further reduced by reducing the liquid interfacial temperature using thermal isolation. As is known, the driving force for liquid evaporation is the difference between the interfacial

vapor pressure p_v and the ambient vapor pressure p_0. p_v is strongly associated with the interfacial temperature T_i, and thus decreasing T_i will decrease p_v and the driving force for liquid evaporation. In order to obtain low interfacial temperature, excellent thermal isolation is required because in most microfabricated reactors the low temperature region at the sample interface is very close to the high temperature region in the reaction chamber. Similar to what has been demonstrated previously, [47] a low stress silicon nitride diaphragm surrounding the reaction chamber can be used to produce good thermal isolation characteristics, resulting in a lower sample interfacial temperature that helps to suppress evaporation (Figure 2.2).

The interfacial temperature, T_i, during a thermal bioreaction is predicted using steady-state heat transfer simulations. Both devices that we simulated contain a long-armed chamber (*i.e.*, a large reaction chamber with two long narrow channels on both ends). In addition, the chamber in one device is thermally isolated with a thin diaphragm as depicted in Figure 2.2(a). As was demonstrated before, [47] the temperature throughout the device without thermal isolation is significantly higher than with thermal isolation. This temperature difference is mostly due to a more than three orders of magnitude difference in the thermal conductivities of silicon and air (150 W/m·K *vs.* 0.026 W/m·K).

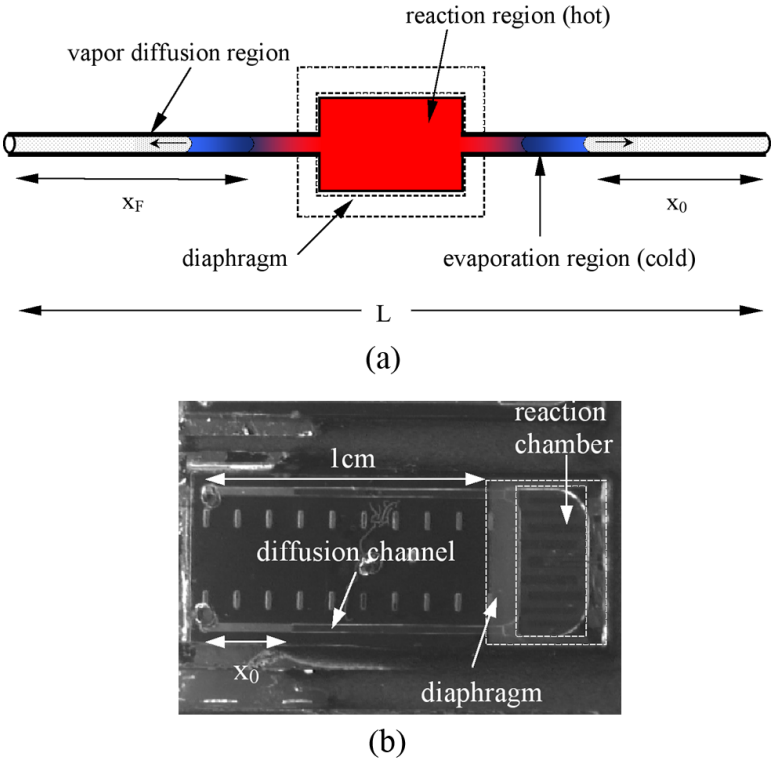

Figure 2.2 (a) Schematic of the long-armed device with thermal isolation. The color gradient conceptually represents the temperature gradient. (b) Picture of the microfabricated device.

To investigate the evaporative loss in a long-armed device with thermal isolation, the relative evaporative loss (V_{loss}/V_{PCR}) is calculated theoretically and experimentally. The theoretical V_{loss}/V_{PCR} ratios are calculated using equation (2.5) and the simulation results of interfacial temperature (listed in Table 2.1). The experimental V_{loss}/V_{PCR} ratios are measured during the reaction in a long-armed device with and without thermal isolation. Both theoretical and experimental V_{loss}/V_{PCR} ratios are plotted in Figure 2.3(a). The plot indicates that the experimental data fit fairly well with the theoretical results, and that the thermally isolated device significantly reduces the evaporative loss compared to the device without thermal isolation. In most cases, with $(L-2x_0)/L<0.83$ (*i.e.*,

$x_0 > 2mm$), the evaporative loss in the device without thermal isolation is more than 5 folds higher than that in the thermally isolated device.

The gel electrophoresis of PCR products collected from the thermally isolated devices shows that most on-chip PCR exhibits similar amplification efficiency to the off-chip positive control (Figure 2.3(b)). No byproduct bands have been detected from both on-chip and off-chip PCR and the yield (brightness analysis) of amplification increases with the reduction of the evaporative loss. This result is understandable since evaporative loss changes not only the reaction volume, but also the sample and reagent concentrations. However, amplification from different template DNAs requires different optimal concentration and thermocycling conditions. Thus, the effect of reducing the evaporative loss on the PCR yield may vary for other DNA samples.

A potential problem associated with this thermal isolation device is that part of the reaction solution (*i.e.*, the sample in the long narrow channels) will not be amplified because it does not experience the desired thermocycling temperatures. However, the results in Figure 2.3(b) indicate that the unreacted sample volume in the channels will not significantly affect the overall PCR fidelity and efficiency because the narrow channels have limited volume of extra solution (less than 10% of the total reaction volume).

Table 2.1 Interfacial temperature, vapor pressure, vapor diffusivity and reaction time used in the calculations

PCR steps	variables	uniform straight channel	long-armed device without thermal isolation	long-armed device with thermal isolation
denaturation	T_{i1}	367K (94°C)	360 K (87°C)	313 K (40°C)
	p_{v1}	81447 Pa	62660 Pa	7375 Pa
	D_{v1}	3.62×10^{-5} m^2/s	3.50×10^{-5} m^2/s	2.74×10^{-5} m^2/s
	t_{F1}	5 s	5 s	5 s
annealing	T_{i2}	328K (55°C)	325 K (52°C)	303 K (30°C)
	p_{v2}	15737 Pa	14000 Pa	4240 Pa
	D_{v2}	2.97×10^{-5} m^2/s	2.92×10^{-5} m^2/s	2.59×10^{-5} m^2/s
	t_{F2}	10 s	10 s	10 s
extension	T_{i3}	345K (72°C)	340 K (67°C)	308 K (35°C)
	p_{v3}	33944 Pa	28000 Pa	5626 Pa
	D_{v3}	3.25×10^{-5} m^2/s	3.16×10^{-5} m^2/s	2.66×10^{-5} m^2/s
	t_{F3}	20 s	20 s	20 s

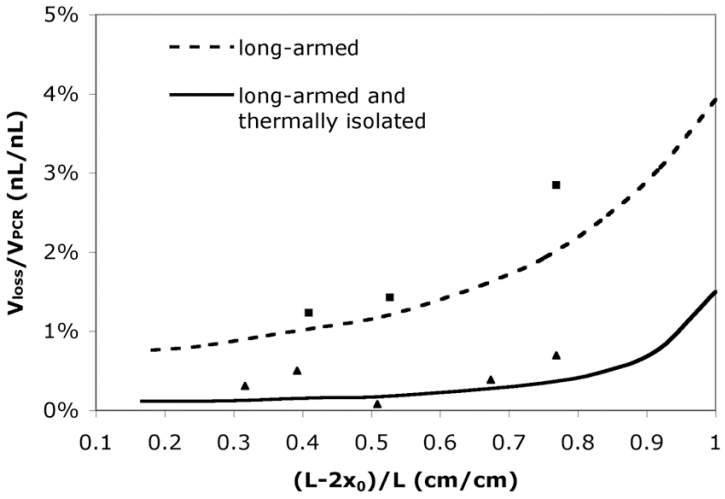

(a)

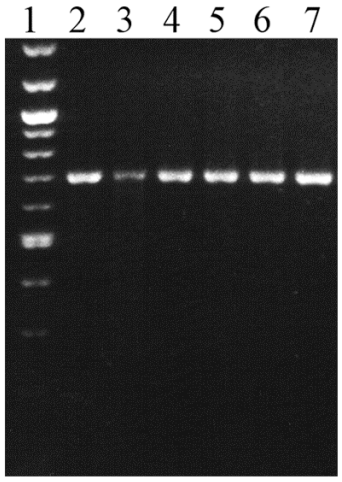

(b)

Figure 2.3 (a) Calculated and experimental relative evaporative loss V_{loss}/V_{PCR} as a function of the fractional filled length $(L-2x_0)/L$. The cross-section areas of reaction chamber A_r and diffusion channel A_c used in the calculation and experiment are 0.2mm^2 and 0.004mm^2, respectively. ■ experimental data in a long-armed device without thermal isolation ; ▲ experimental data in a long-armed device with thermal isolation. (b) Gel electrophoresis of PCR products in the long-armed device with thermal isolation. Lane 1, the 100bp DNA ladder. Lane 2-lane 6, on-chip PCR products. The extra sample volumes in the channels are 7.2%, 6.1%, 4.1%, 2.7% and 1.8% of the reaction volume, respectively. The corresponding values of relative evaporative loss and fractional filled length refer to the experimental data points (from right to left) shown in (a). Lane 7, a positive PCR control carried out in a commercial thermocycler. Lane 3 exhibits lower fluorescent intensity due to sample volume loss during the sample collection process.

To facilitate the reduction of evaporative loss while assuring the reaction efficiency, some key design factors need to be optimized. The width of the silicon nitride diaphragm is one factor that can significantly affect the interfacial temperature. As shown in Figure 2.4(a), a wider diaphragm is expected to provide better thermal isolation and further reduce the evaporative loss. This improvement, however, becomes negligible when the diaphragm is wider than 1.5mm. In addition, larger diaphragms may require longer fabrication time and are sometimes more difficult to handle, implying an optimal width between 1mm and 1.5mm. According to the previous discussions, complete removal of the silicon under the reaction chamber will provide better thermal isolation because it further reduces the heat conduction between the chamber and the rest part of the device.[47] However, heat transfer simulations reveal that in such a design the temperature uniformity in the reaction chamber will be poor compared to the current design in which the chamber is supported by silicon.

The reaction volume also plays an important role in designing long-armed devices with thermal isolation. The result in Figure 2.4(b) indicates that the difference of evaporative loss in a long-armed device with and without thermal isolation is much more prominent for a smaller reaction volume (or smaller cross-section area of reaction chamber). In the current design with a relatively large reaction volume (~800nL), even a device containing long diffusion channels without thermal isolation can reduce the evaporative loss to less than 4%. However, if the reaction chamber volume is reduced to 100nL, the evaporative loss is 20% when $(L-2x_0)/L = 0.83$ (*i.e.*, $x_0 = 2mm$) in the device without thermal isolation, while only 4% in a thermally isolated device. Therefore, it is more advantageous to use a thermally isolated device for small volume reactions.

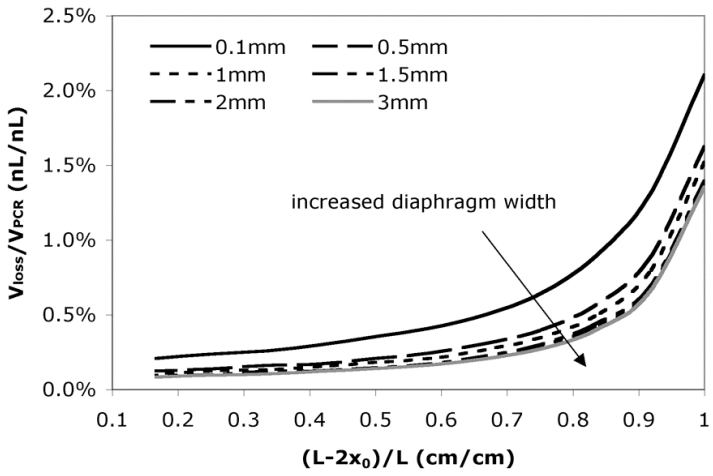

(a)

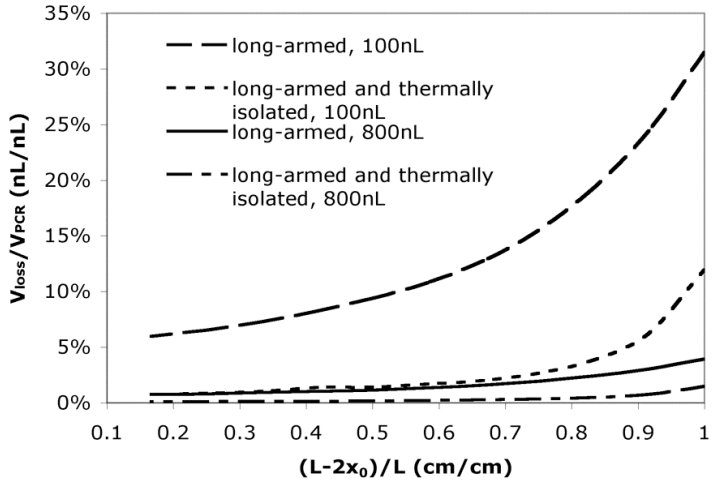

(b)

Figure 2.4 (a) The relative evaporative loss in a thermally isolated long-armed device with different diaphragm width. (b) The relative evaporative loss V_{loss}/V_{PCR} for different reaction volume in a long-armed device with and without thermal isolation.

Vapor replenishment

The driving force for liquid evaporation (*i.e.*, the water vapor concentration gradient) can also be reduced using vapor replenishment. Vapor generated at a pinned water meniscus on both sides of the reaction channel can be used to offset vapor lost from the reaction volume (Figure 2.5(a)). This pinned meniscus increases the water vapor concentration near the reaction solution meniscus, thus reducing the vapor concentration

gradient in the channel. The key feature in this design is the liquid stop fabricated by etching a deep pit near the T-junction (Figure 2.5(b)). The principle of liquid stop is based on the surface energy change when the cross-section of capillary enlarges abruptly.[49] The liquid stop not only prevents the mixing of the reaction solution with the water reservoirs during fluidic operation, but also defines the location of the water meniscus and thus the vapor source.

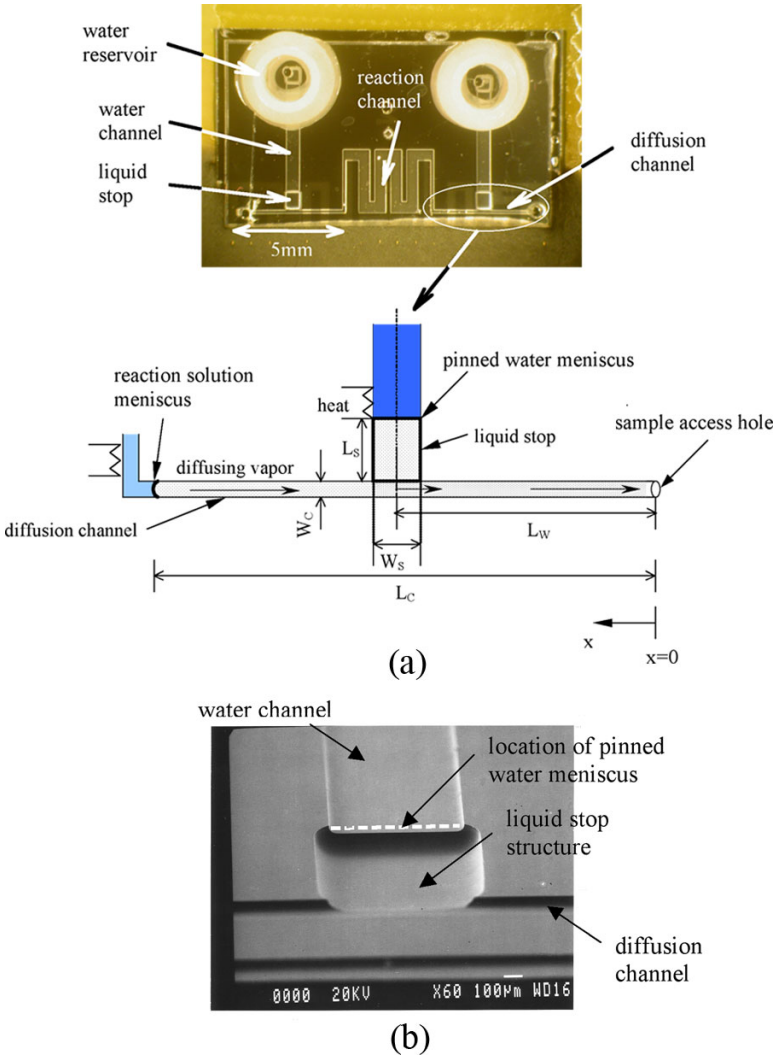

Figure 2.5 (a) Picture of the device with vapor replenishment. L_w is the distance from the sample access hole to the centerline of liquid stop; L_c is the distance from the sample access hole to the reaction solution meniscus; W_c is the width of the diffusion channel; L_s and W_s are the length and width of the liquid stop, respectively. (b) A SEM image of the liquid stop structure.

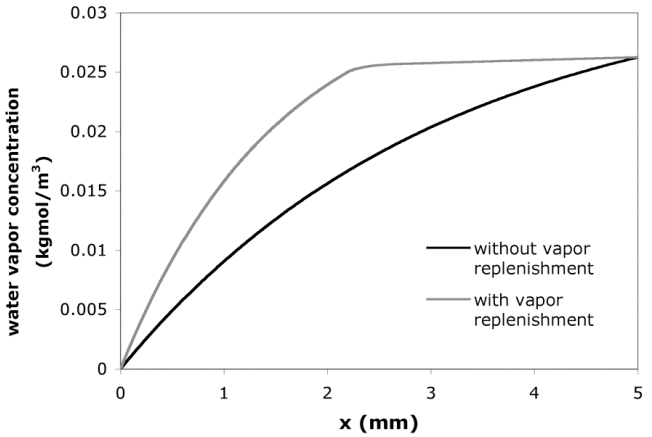

(a)

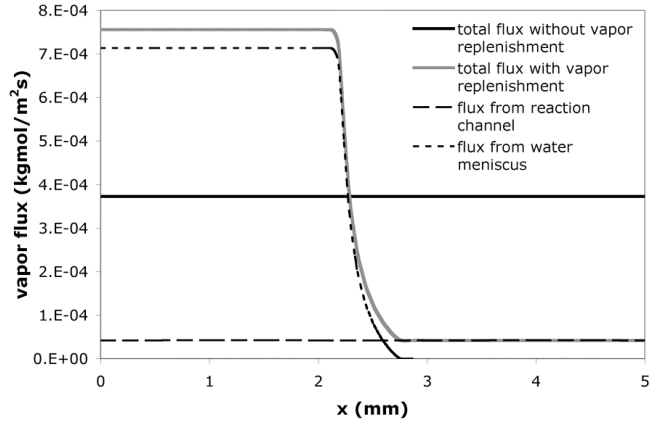

(b)

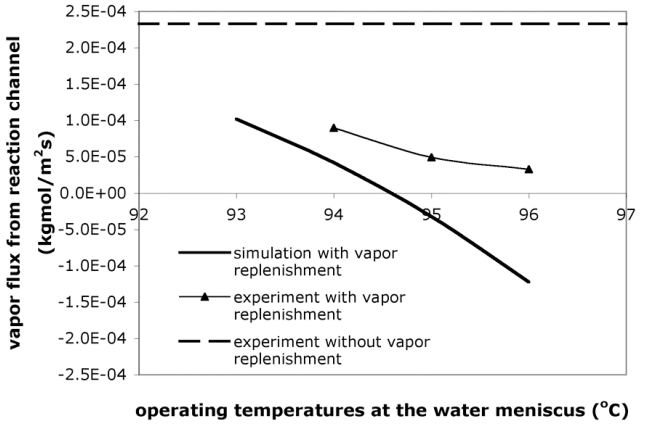

(c)

Figure 2.6 (a) Vapor concentration and (b) vapor flux along the centerline of the diffusion channel in the simulation results. L_c= 5mm; W_c= 100μm; L_s=1mm; W_s= 0.6mm. L_c, W_c, L_s and W_s are defined in the captions of Figure 2.5(a). (c) Vapor flux from the reaction channel with different operating temperatures at the pinned water meniscuses. Note that a positive flux represents an inbound flux (toward the sample access hole) while a negative flux represents an outbound flux (toward the reaction solution meniscus).

Steady-state mass transfer simulations confirm the reduction of water vapor concentration gradient and flux in the diffusion channels using vapor replenishment. The results of concentration and flux values along the centerline of the diffusion channel when the reaction solution is at 94°C are plotted in Figure 2.6(a) and 6(b). Without vapor replenishment, the vapor concentration decreases from the reaction solution meniscus ($x = 5mm$) to the sample access hole ($x = 0mm$) (Figure 2.6(a)), while the total vapor flux is constant along the channel (Figure 2.6(b)). The results in Figure 2.6(a) also indicate that adding vapor into the diffusion channel reduces the vapor concentration gradient between the liquid stop and the reaction solution meniscus and thus the driving force for liquid evaporation. Clearly the vapor replenishment increases the total vapor flux from the liquid stop to the sample access hole ($0 < x < 2.5mm$), but decreases the flux from the reaction volume ($2.5mm < x < 5mm$) in comparison to a constant flux in a straight channel design (Figure 2.6(b)).

Both simulation and experimental results demonstrate that the operating temperatures at the pinned water meniscus significantly affect the water vapor flux, as shown in Figure 2.6(c). In fact, when the operating temperature is higher than 95°C and the reaction temperature remains at 94°C, theory predicts that water vapor will condense at the reaction solution meniscus. Experimental results show the same trend as the theory but the experimental fluxes are positive for all temperature points tested. This difference could be due to the assumption in the simulations –fixed reaction solution meniscus position – that does not match the real reaction conditions. Moreover, the reaction solution meniscus may be heated above 94°C due to thermal crosstalk from the heated (*i.e.*, above 95°C) water meniscus, a situation that can be eliminated with proper device

design. On-chip PCR with different water-meniscus operating temperatures produced similar amplification efficiency to off-chip positive controls (data not shown). In addition, similar to the results obtained in the thermally isolated device, no byproducts have been detected, and less evaporative loss also leads to higher amplification yield.

Design factors such as the geometry and location of the liquid stop play an important role in minimizing the vapor flux and the evaporative loss. As shown in Figure 2.7(a), the total vapor flux from the reaction solution meniscus decreases with decreasing liquid stop length. A shorter liquid stop reduces the distance between the vapor source (the pinned water meniscus) and the T-junction in the diffusion channel, thus increasing the vapor concentration at the T-junction. This increase will decrease the vapor concentration gradient between the reaction solution meniscus and the T-junction, resulting in less vapor flux from the reaction solution. A wider liquid stop (*i.e.*, a larger surface area of the pinned water meniscus) also facilitates the reduction of vapor flux from the reaction solution by increasing the vapor concentration at the T-junction (Figure 2.7(b)). Moreover, the lowest total flux from the reaction solution is achieved when the liquid stop intersects the diffusion channel at the midpoint (Figure 2.7(c)).

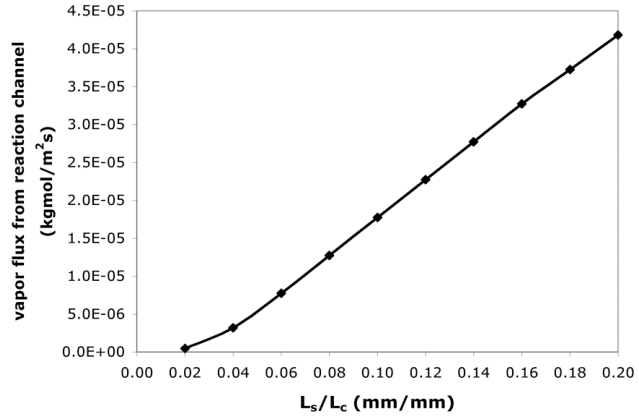

(a)

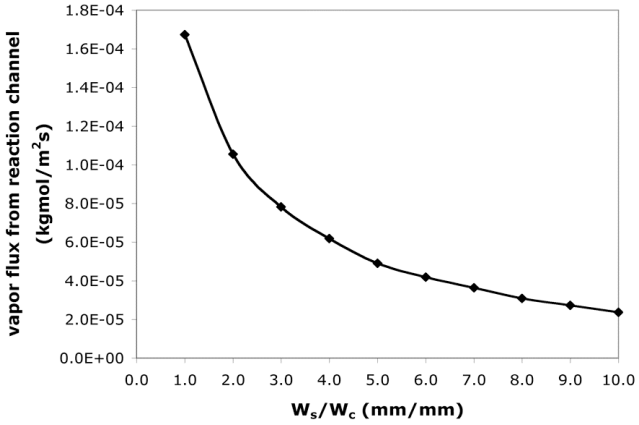

(b)

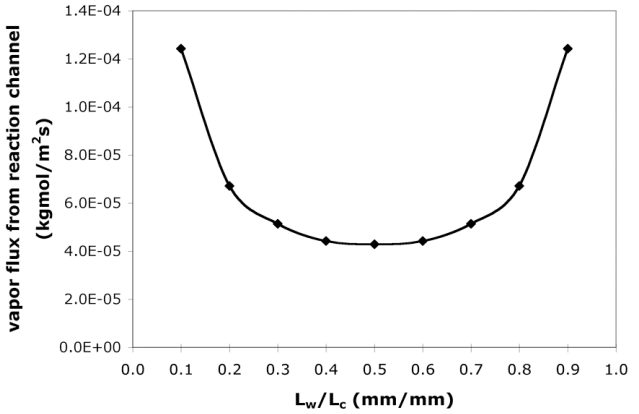

(c)

Figure 2.7 Simulation results of vapor fluxes from the reaction channel (a) when different length of the liquid stop is used; (b) when different width of the liquid stop is used; (c) when the location of the liquid stop varies with L_s=1mm and W_s= 0.6mm. All the simulations use 94°C as the operating temperature at the water meniscus, L_c= 5mm and W_c= 100μm. L_c, W_c, L_w, L_s and W_s are defined in the caption of Figure 2.5(a).

Conclusions

We have developed valveless strategies to reduce the sample evaporative loss during microfluidic thermal reactions using the principle of diffusion-limited evaporation. The microchannels on both sides of the reaction region provide long narrow diffusion paths that reduce the evaporation rate. Decreasing the driving force for evaporation by either increasing the thermal isolation of the reaction chamber or by increasing the concentration of water vapor in the diffusion channel will also limit the evaporation. Both theoretical and experimental results demonstrate that the proposed strategies can effectively reduce the evaporation rate during thermocycling and successfully perform PCR without using microvalves. Although PCR has been taken as an example to demonstrate the capability of the devices, the novel miniaturized methodologies provided by these devices can also be applied in microfluidic devices for other chemical and biochemical reactions. Moreover, these methodologies can be readily integrated into more advanced devices such as integrated analysis systems.

References

1. F. Sanger, S. Nicklen and A. R. Coulson, *Proc. Natl. Acad. Sci. U.S.A.*, 1977, **74**, 5463-5467.
2. F. Barany, *Proc. Natl. Acad. Sci. U.S.A.*, 1991, **88**, 189-193.
3. A. T. Woolley, D. Hadley, P. Landre, A. J. DeMello, R. A. Mathies and M. A. Northrup, *Anal. Chem.*, 1996, **68**, 4081-4086.
4. L. C. Waters, S. C. Jacobson, N. Kroutchinina, J. Khandurina, R. S. Foote and J. M. Ramsey, *Anal. Chem.*, 1998, **70**, 158-162.
5. L. C. Waters, S. C. Jacobson, N. Kroutchinina, J. Khandurina, R. S. Foote and J. M. Ramsey, *Anal. Chem.*, 1998, **70**, 5172-5176.
6. J. Khandurina, T. E. Mcknight, S. C. Jacobson, L. C. Waters, R. S. Foote and J. M. Ramsey, *Anal. Chem.*, 2000, **72**, 2995-3000.
7. R. C. Anderson, X. Su, G. J. Bogdan and J. Fenton, *Nucleic Acids Res.*, 2000, **28**, e60-e60.
8. E. T. Lagally, P. C. Simpson and R. A. Mathies, *Sensor Actuat. B*, 2000, **63**, 138-146.
9. E. T. Lagally, I. Medintz and R. A. Mathies, *Anal. Chem.*, 2001, **73**, 565-570.
10. J. W. Hong, T. Fujii, M. Seki, T. Yamamoto and I. Endo, *Electrophoresis*, 2001, **22**, 328-333.
11. P. K. Yuen, L. J. Kricka, P. Fortina, N. J. Panaro, T. Sakazume and P. Wilding, *Genome Res.*, 2001, **11**, 405-412.

12. Y. Liu, C. B. Rauch, R. L. Stevens, R. Lenigk, J. Yang, D. B. Rhine and P. Grodzinski, *Anal. Chem.*, 2002, **74**, 3063-3070.

13. Y. S. Shin, K. Cho, S. H. Lim, S. Chung, S. J. Park, C. Chung, D. C. Han and J. K. Chang, *J. Micromech. Microeng.*, 2003, **13**, 768-774.

14. L.-M. Fu and C.-H. Lin, *Biomed. Microdevices*, 2007, **9**, 277-286.

15. R. G. Blazej, P. Kumaresan and R. A. Mathies, *Proc. Natl. Acad. Sci. U.S.A.*, 2006, **103**, 7240-7245.

16. J. Cheng, M. A. Shoffner, K. R. Mitchelson, L. J. Kricka and P. Wilding, *J. Chromatogr. A*, 1996, **732**, 151-156.

17. E. T. Lagally, C. A. Emrich and R. A. Mathies, *Lab Chip*, 2001, **1**, 102-107.

18. E. T. Lagally, J. R. Scherer, R. G. Blazej, N. M. Toriello, B. A. Diep, M. Ramchandani, G. F. Sensabaugh, L. W. Riley and R. A. Mathies, *Anal. Chem.*, 2004, **76**, 3162-3170.

19. C. G. Koh, W. Tan, M. Q. Zhao, A. J. Ricco and Z. H. Fan, *Anal. Chem.*, 2003, **75**, 4591-4598.

20. R. H. Liu, J. N. Yang, R. Lenigk, J. Bonanno and P. Grodzinski, *Anal. Chem.*, 2004, **76**, 1824-1831.

21. D. S. Yoon, Y. S. Lee, Y. Lee, H. J. Cho, S. W. Sung, K. W. Oh, J. Cha and G. Lim, *J. Micromech. Microeng.*, 2002, **12**, 813-823.

22. Z. Zhao, Z. Cui, D. Cui and S. Xia, *Sensor Actuat. A*, 2003, **108**, 162-167.

23. I. Rodriguez, M. Lesaicherre, Y. Tie, Q. Zou, C. Yu, J. Singh, L. T. Meng, S. Uppili, S. F. Y. Li, P. Gopalakrishnakone and Z. E. Selvanayagam, *Electrophoresis*, 2003, **24**, 172-178.

24. H. Wang, J. Chen, L. Zhu, H. Shadpour, M. L. Hupert and S. A. Soper, *Anal. Chem.*, 2006, **78**, 6223-6231.

25. M. Hashimoto, M. L. Hupert, M. C. Murphy and S. A. Soper, *Anal. Chem.*, 2005, **77**, 3243-3255.

26. D. S. Lee, S. H. Park, H. Yang, K. H. Chung, T. H. Yoon, S. J. Kim, K. Kim and Y. T. Kim, *Lab Chip*, 2004, **4**, 401-407.

27. M. U. Kopp, A. J. De Mello and A. Manz, *Science*, 1998, **280**, 1046-1048.

28. P. J. Obeid, T. K. Christopoulos, H. J. Crabtree and C. J. Backhouse, *Anal. Chem.*, 2003, **75**, 288-295.

29. N. Park, S. Kim and J. H. Hahn, *Anal. Chem.*, 2003, **75**, 6029-6033.

30. M. Hashimoto, P. C. Chen, M. W. Mitchell, D. E. Nikitopoulos, S. A. Soper and M. C. Murphy, *Lab Chip*, 2004, **4**, 638-645.

31. J. Liu, M. Enzelberger and S. Quake, *Electrophoresis*, 2002, **23**, 1531-1536.

32. R. P. Oda, M. A. Strausbauch, A. F. R. Huhmer, N. Borson, S. R. Jurrens, J. Craighead, P. J. Wettstein, B. Eckloff, B. Kline and J. P. Landers, *Anal. Chem.*, 1998, **70**, 4361-4368.

33. A. F. R. Huhmer and J. P. Landers, *Anal. Chem.*, 2000, **72**, 5507-5512.

34. B. C. Giordano, J. Ferrance, S. Swedberg, A. F. R. Huhmer and J. P. Landers, *Anal. Biochem.*, 2001, **291**, 124-132.

35. J. Chen, M. Wabuyele, H. Chen, D. Patterson, M. Hupert, H. Shadpour, D. Nikitopoulos and S. A. Soper, *Anal. Chem.*, 2005, **77**, 658-666.

36. M. G. Pollack, P. Y. Paik, A. D. Shenderov, V. K. Pamula, F. S. Dietrich and R. B. Fair, *μTAS*, 2003, 619-622.

37. M. Krishnan, V. M. Ugaz and M. A. Burns, *Science*, 2002, **298**, 793-793.

38. E. K. Wheeler, W. Benett, P. Stratton, J. Richards, A. Chen, A. Christian, K. D. Ness, J. Ortega, L. G. Li, T. H. Weisgraber, K. Goodson and F. Milanovich, *Anal. Chem.*, 2004, **76**, 4011-4016.

39. R. Pal, M. Yang, R. Lin, B. N. Johnson, N. Srivastava, S. Z. Razzacki, K. J. Chomistek, D. Heldsinger, R. M. Haque, V. M. Ugaz, P. Thwar, Z. Chen, K. Alfano, M. Yim, M. Krishnan, A. O. Fuller, R. G. Larson, D. T. Burke, and M. A. Burns, *Lab Chip*, 2005, **5**, 1024-1032.

40. P. K. Yuen, L. J. Kricka and P. Wilding, *J. Micromech. Microeng.*, 2000, **10**, 401-409.

41. W. H. Grover, A. M. Skelley, C. N. Liu, E. T. Lagally and R. A. Mathies, *Sensor Actuat. B-Chem.*, 2003, **89**, 315-323.

42. T. Thorsen, S. J. Maerkl, S. R. Quake, *Science*, 2002, **298**, 580-584.

43. J. Liu, C. Hansen and S. R. Quake, *Anal. Chem.*, 2003, **75**, 4718-4723.

44. R. Pal, M. Yang, B. N. Johnson, D. T. Burke and M. A. Burns, *Anal. Chem.*, 2004, **76**, 3740-3748.

45. R. H. Perry and D. W. Green, *Perry's Chemical Engineers' Handbook*, 1997, **7th ed.**, 2-49.

46. C. J. Geankoplis, *Transport Processes and Unit Operations*, 1993, **3rd ed.**, 396.

47. M. Yang, R. Pal and M. A. Burns, *J. Micromech. Microeng.*, 2005, **15**, 221-230.

48. S. Jin and K. S. Breuer, *IMECE*, 2003, 44135.

49. P. F. Man, C. H. Mastrangelo, M. A. Burns and D. T. Burke, *MEMS '98*, Heidelberg, Germany, 1998, pp. 45-50.

CHAPTER 3

PERFORMANCE OF NANOLITER-SIZED DROPLET-BASED MICROFLUIDIC PCR

Introduction

In recent years, droplet-based multiphase microfluidics has been emerging as a promising approach for fundamental and applied research in chemical and biological analyses. Droplet formation with sizes from femto- to microliter in a microfluidic system can be well controlled by adjusting the channel geometry and fluid flow rates (*e.g.*, T-junction[1-3] as well as flow focusing[4-5], or using electrohydrodynamic (EHD) methods such as dielectrophoresis (DEP)[6-7] and electrowetting on dielectric (EWOD)[8-10]. Other techniques for generating and actuating droplets using microfabricated pneumatic chopper[11-12], surface acoustic wave (SAW)[13], and electromagnetic force[14-15] have also been reported. In addition, droplet manipulations including breakup[16-17], fusion[18-22], mixing[20, 23-24] and sorting[25-26] have been studied to further exploit the droplet-based microsystems. With the development of techniques for droplet generation and manipulation, droplet-based microfluidics offers the capability to form and isolate controllable reaction volumes, achieve rapid mixing of reagents, and increase the reaction throughput. Droplet-based microsystems have been developed to perform a variety of chemical and biological reactions and analytical processes, such as nanoparticle

synthesis[19, 27-28], biological fluids analysis[29], cell analysis[30-32], protein expression[33-34] and crystallization[35], and genetic analysis[13-15, 31-32, 36-40].

As one crucial technique in most genetic analyses, the polymerase chain reaction (PCR) has been extensively investigated in miniaturized single-phase system, in order to achieve rapid and inexpensive analyses[41]. Droplet-based PCR not only offers the capability of reducing the reactor volume, but also provides the potential to alleviate the problems commonly found in single-phase PCR microsystems, such as evaporation loss and non-specific surface adsorption. In a single-phase PCR microsystem without any sealing components, evaporation loss could be 40% to 100% of the reaction volume[42]. Using sealing agents reduces the evaporation, but increases the fabrication and operation complexity. Most reported on-chip droplet-based PCR were performed in monodisperse picoliter droplets[37-38]. These systems have shown the ability to detect a single copy of nucleic acid molecule in a complex background, indicating applications such as detection of low concentrations of disease-associated mutations. Moreover, such a small droplet size (*i.e.*, reactor volume) significantly decreases the diffusion distance and thereby reduces the total reaction time, allowing earlier detection of target molecules in high-throughput.

A potential problem in picoliter droplet-based PCR is that the possible nonuniform encapsulation of template molecules (especially long templates) and reagents could lead to nonuniform amplification in monodisperse droplets. However, a statistical analysis of the amplified targets should be able to circumvent this problem as long as the droplet density and spacing are appropriate. Another problem with amplification in picoliter-sized droplets is that, for cases where downstream processes (e.g., restriction

digestion, and hybridization) need to be performed, sufficient product molecules may not be available. In addition, in many PCR-based diagnoses, the initial target molecule concentrations in patient samples are so low that analysis in picoliter-sized droplets is not possible. For example, in the early diagnosis of HIV, the concentration of HIV RNA in the HIV-infected patient samples usually ranges only from 10^2 to 10^6 copies/mL[43-44]. Thus, only one of several thousand or even million picoliter-scale droplets will contain one copy of the target molecule. Larger droplets (nano- to microliter) have to be employed in these cases to increase the chances of detecting the infectious agent. In all cases, though, an understanding of the performance of droplet-based PCR is necessary to properly design and operate such microfluidic systems.

In this chapter, we have performed PCR in the aqueous-in-oil droplets generated using sequential injection mode in a microfluidic device with on-chip heating and temperature control. The on-chip electronics allows rapid transition between temperature points and accurate detection of reaction conditions. Unlike the previous studies that are focused on demonstrating a droplet-based microsystem for PCR, we have also provided in-depth studies of the performance of droplet-based PCR by investigating the effect of reaction parameters, including polymerase concentration, Mg^{2+} concentration, hold time at each temperature step, template DNA concentration and droplet size. With the optimized reaction parameters, our system demonstrates the capability of monitoring the amplification in real time and providing faster detection than the benchtop instruments. Our characterization studies will also aid in the design and operation of similar droplet-based microsystems for use in portable point-of-care diagnosis.

Materials and Methods

Device fabrication

The fluid network is fabricated on a glass wafer using photolithography and wet chemical etching. The detailed procedure have been outlined elsewhere[45]. Briefly, a thin metal film (500Å Cr/ 2500Å Au) is deposited and patterned on the glass wafer. The glass wafer is then etched to the desired depth in hydrofluoric acid (49%) (CMOS grade; J.T. Baker, Philipsburg, NJ). Next, the photoresist is striped and the metal layer is removed. The glass wafer is then diced to obtain individual dies. The heaters and resistance temperature detectors (RTDs) are fabricated on a silicon wafer with a 5000Å thick silicon oxide layer. Firstly, photoresist is patterned on the silicon wafer using photolithography. Next, 700Å Chromium and 450Å gold are evaporated on the silicon wafer. The wafer is then left in acetone (CMOS grade; J.T. Baker, Philipsburg, NJ) to liftoff unwanted metal. The diced individual silicon dies are fixed on the custom designed printed circuit board (PCB, Advanced Circuits, Aurora, CO), and then wire bonded (Kulicke & Soffa 4124 Ball Bonder) using 1.0 mil gold wire. Finally, the silicon and glass components are visually aligned and then bonded using UV curable optical glue.

Instrumentation

The setup for reaction temperature control consists of a DC power supply (B+K Precision Model 1760, Yorba Linda, CA), two data acquisition (DAQ) boards (National instruments PCI 6031E and PCI-6704, Austin, TX), two connector blocks (National instruments SCB-100 and SCB-68, Austin, TX), a signal conditioning circuit, a computer and two LabVIEW programs (National instruments, Austin, TX). The RTDs are

calibrated by heating the device in a convection oven and recording the temperature-resistance data in a LabVIEW program. The slope and intercept from a linear fit of the temperature and resistance data are read into the control algorithms that use a proportional-integral (PI) module to control temperature. The precision of temperature control is ± 0.2^{o}C. The heaters are connected to the power supply through the signal conditioning circuit that boosts the supply voltage from the computer with an op-amp gain of 3. During the experiments, the device is placed on a copper block that sits on a probe station with temperature maintained at 10^{o}C.

Lab air supply controlled by a regulator (VSO-EP; Parker, Cleveland, OH) provides the pneumatic pressure used to form the droplet in the microdevice. Pressure or vacuum is applied through syringes connected to each port on the device. The Pulsing of pressure or vacuum is controlled by a set of three-way solenoid valves (Numatech, Wixom, MI). Opening and closing of the solenoid valves are operated through a combination of a DC power supply (Electro Industries, Model Digi 35A) and a relay board (Model ER-16; National Instruments, Austin, TX). Functioning of the relay board is controlled through a LabVIEW program and a Digital I/O card (National Instrument PCI-DIO-96, Austin, TX).

PCR amplification

The PCR mixture consists of λDNA template (Invitrogen, Carlsbad, CA) with the concentration ranging from 3.5ng/μL to 3.5x10^{-4}ng/μL, dNTPs (0.2mM each dATP, dGTP, dCTP and 0.4mM dUTP), 10mM Tris-HCl (pH 8.3), 50mM KCl, 0.01mM EDTA, 3.5mM $MgCl_2$, 0.9μM each primer, 0.25μM probe, 0.01units/μL AmpErase UNG, and

0.175units/μL AmpliTaq Gold® DNA polymerase (Applied Biosystems, Foster City, CA). The sequences of forward and reverse primers are 5'-CATCAAAGCCATGAACAAAGCA-3' and 5'-TCAGCAACCCCGGTATCAG-3', respectively. The sequence of probe is 5'6FAM-CCGCGCTGGATGA-3'MGBNFQA. This size of the target product is 56bp. The thermocycling protocol used in most of the on-chip droplet-based PCR consists of 50°C for 2min, 95°C for 10min, followed by 16 cycles of 95°C for 9s and 60°C for 30s. PCR grade mineral oil (Sigma Aldrich, St. Louis, MO) is used as the continuous oil phase.

Fluorescence detection and analysis

An inverted fluorescence microscope (Nikon Eclipse TE2000-U) with a 2x objective (Nikon) is used to monitor fluorescence of the reaction droplet. An X-cite Series 120 lamp (EXFO Life Science Divisions, Ontario, Canada) with FITC filter is used as the excitation source. The fluorescence images are captured using a digital CCD camera (Photometrics Cascade 512F; Roper Scientific, Tucson AZ) with a 500ms exposure time. The relative fluorescence intensity is used to quantify the amplification yield in the droplet, which is calculated by scaling the fluorescence intensity of the droplet by that of the reference area on the device. Data analysis is done by MetaVue Software.

Results and Discussions

PCR in single submicroliter droplet

Single droplets with a volume range of ~5-250nL were formed reproducibly in a microfabricated device. The device design includes a 45-degree junction followed by a neck region (220μm wide and 60μm long) between the junction and the main channel (400μm wide and 3mm long) (Figure 3.1(a)). The reaction chamber downstream of the main channel is 1mm wide and 2.5mm long, and the entire fluid network is 100μm deep. A sequential injection mode is employed to form single large droplets (Figure 3.1(b)-(e)) by first filling the device with mineral oil using capillary forces and then injecting the aqueous reaction solution into the device using pulsed pressure (~4 psig, on for 15 ms, off for 1 sec). The pulsing is turned off once the oil/aqueous interface reaches the desired position in the main channel or the reaction chamber. Next, pulsed pressure (~4 psig, on for 15 ms, off for 1 sec) is applied through the oil inlet to break the aqueous stream in the neck region and then push the droplet into the reaction chamber while simultaneously pushing the rest of the aqueous solution back to the reservoir.

The droplet size is dependent on the position of the oil/aqueous interface in the direction toward the outlet and can easily be controlled by adjusting the strength and frequency of the pulsed pressure. The pressure is applied to individual liquid phases sequentially and thus no balance of the flow rates is necessary. The droplet size is also quite reproducible. For example, when forming 20 droplets with a designed size of 150nL, the average of the actual droplet size is 149.92nL with a standard deviation of

8.45nL. The entire procedure for forming droplets of various sizes (~5-250nL; Figure 3.2) takes less than 10 sec.

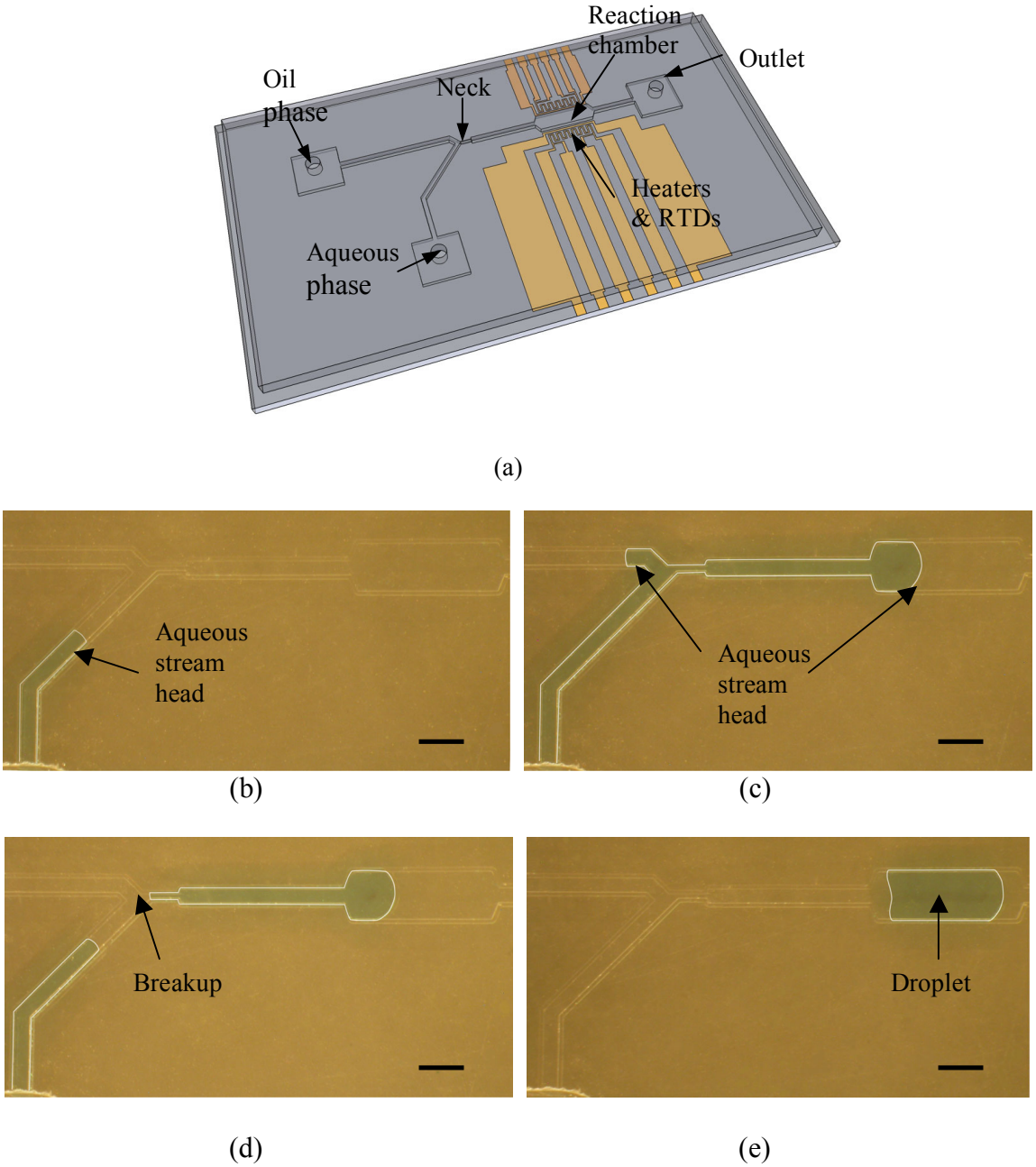

Figure 3.1 (a) Schematic of the device design. (b)-(e) Formation process of single submicroliter droplet. All the scale bars represent 800μm.

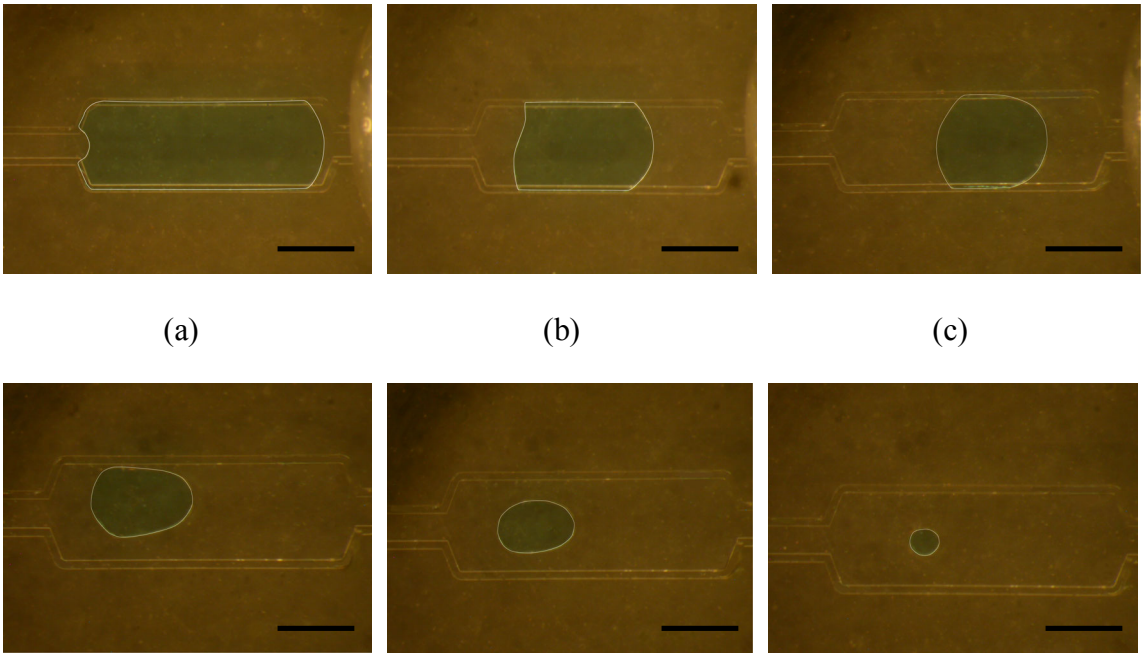

(a) (b) (c)

(d) (e) (f)

Figure 3.2 On-chip formed different sized single droplet: (a) ~225nL; (b) ~125nL; (c) ~80nL; (d) ~40nL; (e) ~26nL; (f) ~5nL. All the scale bars represent 800μm.

PCR of λDNA has been successfully performed in the droplets using on-chip metal heaters and RTDs (Figure 3.1(a)). With FRET probes included in the reaction mixture, the amplification can be detected *in situ* using fluorescent microscopy. As shown in Figure 3.3, the relative fluorescence intensity of the reaction droplet increases significantly (from 1.007 to 1.464) after 40 cycles of PCR. No volume loss of the reaction solution has been observed as measured using the droplet area in the fluorescent images. This result reveals that the droplet-based microsystem can effectively prevent evaporation during high temperature reactions by encapsulating the reaction solution into the continuous oil phase, eliminating the need for mechanical microvalves.

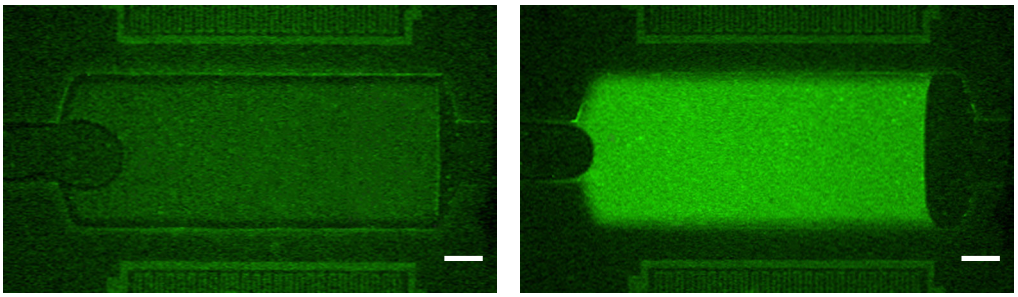

(a) (b)

Figure 3.3 Fluorescence images of the reaction droplet (a) before PCR and (b) after 40 PCR cycles. The template λDNA concentration is 3.5ng/μL (~6.69×10^7 copies/μL). The droplet size is ~225nL. The scale bar represents 250μm.

Effect of reaction parameters on performance of droplet-based PCR

For a multi-component reaction such as PCR, many parameters can affect the reaction performance. The effect of different parameters should be relatively independent of the droplet size, although some surface-related phenomena may include some size dependence. Therefore, we have studied the effect of a series of reaction parameters including droplet size on PCR performance.

Reagent concentration

Polymerase is a critical reagent that is responsible for catalyzing the PCR amplification. The result in Figure 3.4 shows that higher polymerase concentration is required for the droplet-based PCR to achieve on-chip amplification comparable to benchtop results. The optimum polymerase concentration is 0.175 U/μL for on-chip droplet PCR, while the recommended concentration for benchtop PCR is 0.025 U/μL. This observation indicates polymerase loss from the aqueous phase, similar to the effect reported for PCR in a single-phase microsystem[46-47]. This polymerase loss could be due to the partition of the polymerase to the aqueous/oil interface which reduces the

aqueous/oil interfacial tension[48]. The polymerase could also be non-specifically adsorbed to the device surface since previous studies have found that *Taq* polymerase has a high adsorption affinity to most surfaces[49].

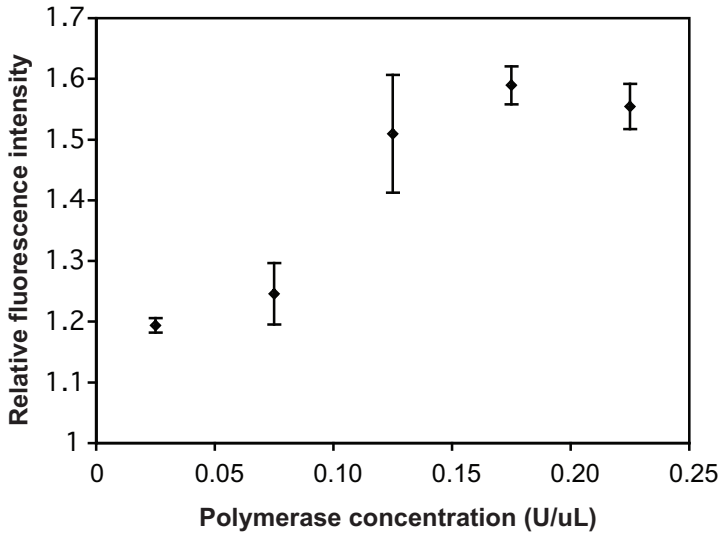

Figure 3.4 Effect of polymerase concentration on amplification efficiency. The template λDNA concentration is 3.5ng/μL (~6.69×10^7 copies/μL). The droplet size is ~150nL. The error bar represents the standard deviation.

The Mg^{2+} concentration in the PCR droplet was also varied to determine its effect on the amplification yield. Previous benchtop studies have shown that polymerase can only work with the presence of free Mg^{2+}, but that free Mg^{2+} can also bind to other reaction components such as dNTPs, primers and DNA. As shown in Figure 3.5, the optimum Mg^{2+} concentration for on-chip droplet-based PCR is 3.5mM, the same as that in the benchtop PCR and the single-phase on-chip PCR[47]. A higher (5.5mM) or lower (1.5mM) Mg^{2+} concentration results in significantly lower fluorescence intensity of reaction droplet, indicating the inhibition of amplification. However, in benchtop PCR the amplification efficiency is relatively insensitive to Mg^{2+} concentration within the range of 3.5-5.5mM (data not shown). One possible explanation to the different effects of

high Mg^{2+} concentration on benchtop and droplet-based PCR might be that as divalent cation, Mg^{2+} could bind to the O^- group on the chamber surface[50] of the microdevice and function as an ion bridge between the chamber surface and the negatively charged DNA, which reduces the free template DNA in the reaction mixture. When the Mg^{2+} concentration increases (> 3.5mM), the "DNA loss" could become more drastic due to the high surface-to-volume ratio of the microdevice, resulting in the decrease of PCR yield.

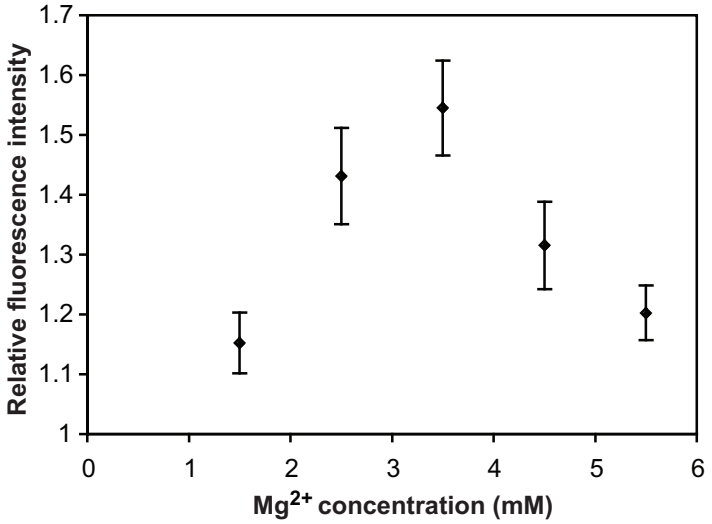

Figure 3.5 Effect of Mg^{2+} concentration on amplification efficiency. The template λDNA concentration is 3.5ng/μL (~$6.69x10^7$ copies/μL). The droplet size is ~150nL. The error bar represents the standard deviation.

Hold time at each temperature step

Rapid heat transfer in microfludic devices allows droplet-based PCR to achieve comparable efficiencies to the benchtop amplification with less reaction time. However, the hold time at each temperature step still needs to be optimized to ensure that the droplet reaches and maintains the desired temperature for a sufficient time required by the reaction kinetics. In addition, unlike the single-phase based microsystem where the

reaction solution is isolated by air, the PCR droplet is surrounded by oil that has higher thermal conductivity and thermal mass than air. Therefore, it may take a longer time for the reaction solution in the droplet to reach the desired temperature than that in the single-phase based microdevice.

Figure 3.6 shows the effect of hold time at each PCR step (activation, denaturation, and annealing/extension) on the amplification yield. The optimum thermal activation time is 10 min, while shorter or longer activation suppresses the reaction (Figure 3.6(a)). As shown in Figure 3.6(b), the fluorescence intensity of reaction droplet increases with the increase of denaturation time, and reaches a maximum value at about 9 sec. Moreover, the PCR yield will not be improved by further extending the denaturation time. At the annealing/extension step, the fluorescence intensity and the hold time show a relationship similar to that at the denaturation step (Figure 3.6(c)), with an optimum hold time of 30 sec. Although a hold time of 40 sec for annealing and extension further increases the amplification yield, 30 sec was chosen as the optimum hold time considering the tradeoff between the hold time and the reaction yield. Using the optimized hold time at each temperature, the total reaction time for on-chip droplet PCR is half of that for benchtop PCR. With the current system, the heating and cooling rate is 9^{o}C/s and 3.5^{o}C/s, respectively. Although it is possible to further accelerate the temperature transition by optimizing the heater design and achieving better local heating using thermal isolation techniques, the total reaction time may not be reduced since it is mainly limited by the reaction kinetics.

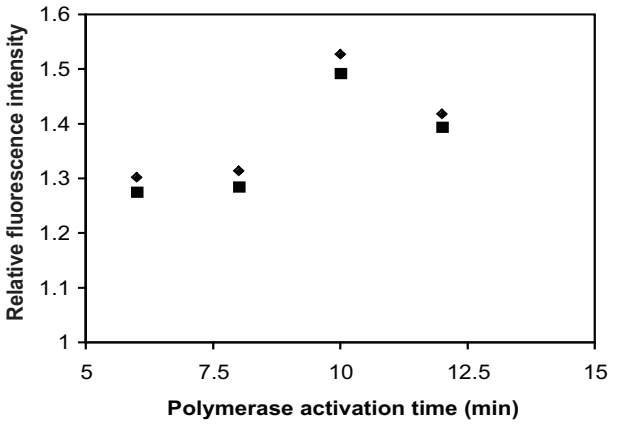

(a)

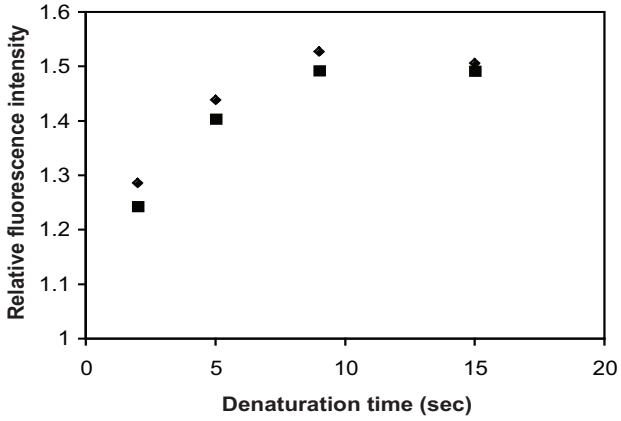

(b)

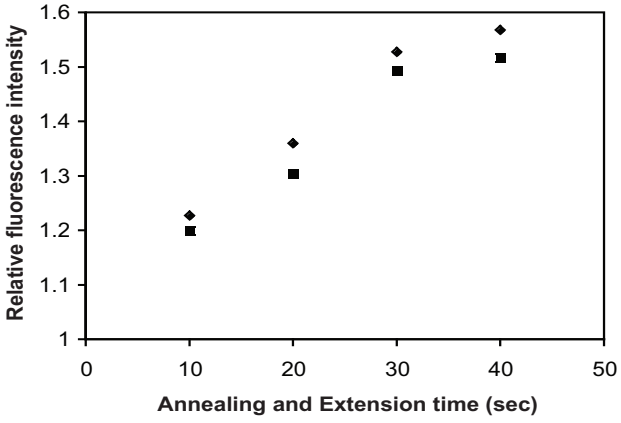

(c)

Figure 3.6 Effect of hold time at different temperature step on amplification efficiency. (a) Thermal activation step; (b) denaturation step; (c) annealing/extension step. The template λDNA concentration is 3.5ng/μL. The droplet size is ~150nL. The data are from duplicate experiments.

Template DNA quantity

PCR with different amounts of template (λDNA) have been performed using the optimized reaction parameters. The quantity of template DNA in the droplet is determined by the template concentration and the droplet size. As shown in Figure 3.7, the fluorescence intensity of the reaction droplet increases with increasing template DNA concentration. Also, for a given template concentration, larger droplets give higher fluorescence intensity (Figure 3.8(a)). Results in both Figure 3.7 and 8(a) indicate that, overall, there is a positive effect of template DNA quantity on the PCR yield. In addition, with the same quantity of template DNA (10^6 to 10^7 copies), the fluorescence intensity in the reactions with fixed droplet size is approximately the same as that in the reactions with fixed template DNA concentration.

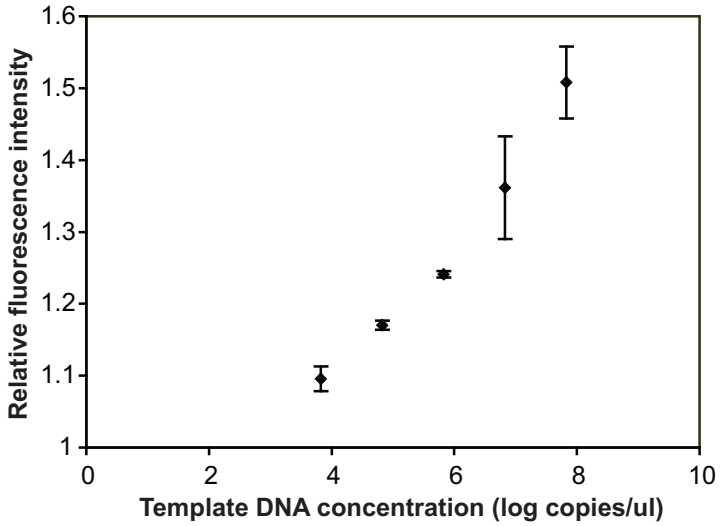

Figure 3.7 Fluorescence intensity of reaction droplet containing different concentrations of template λDNA after 16 PCR cycles. The droplet size is ~150nL. The error bar represents the standard deviation.

However, there is no clear trend for the relationship between the amplification yield (*i.e.*, fluorescence intensity) and the droplet size. Presumably, if adsorption of reagents on either the chamber walls or the liquid-liquid interface was occurring, reaction performance would decrease as the surface-to-volume ratio (S/V) increased. Figure 3.8(b) indicates the total S/V (S_T/V) as well as the contribution from the walls (S_w/V) and the interface (S_i/V). The fluorescence intensity is relatively constant in droplets smaller than 80nL (Figure 3.8(a)) even though in this region the S_i/V and S_T/V dramatically increase with decreasing droplet size (Figure 3.8(b)). However, since these droplets are disc-shaped (confined by the top and bottom chamber walls but free from the side walls), the wall surface-to-volume ratio (S_w/V) is relatively constant. These results suggest the adsorption to the chamber surface is more important than adsorption to the liquid interface. Note that, when droplets are larger than 80nL, the S_i/V and S_T/V still increase with decreasing drop size albeit at a lower rate. The apparent decrease in fluorescence intensity with decreasing droplet size may thus be explained by adsorption onto the chamber solid surfaces, but more studies need to be conducted to confirm this effect.

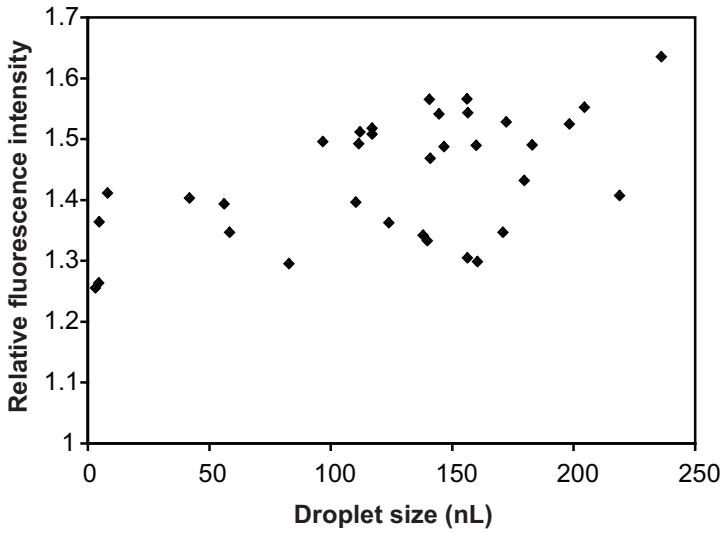

(a)

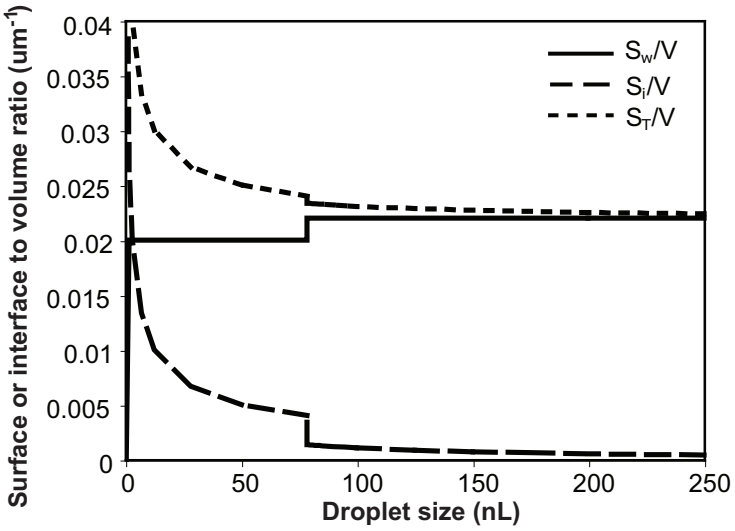

(b)

Figure 3.8 (a) Fluorescence intensity of different sized reaction droplet after 16 PCR cycles. The template DNA concentration is 3.5ng/μL (~6.69x10^7 copies/μL) in all the droplets. (b) Calculated surface to volume ratio of different sized droplets. V is the droplet volume; S_w is the area of the droplet surface confined by the chamber walls; S_i is the area of the unconfined liquid-liquid interface of the droplet; S_T is the total surface area of the droplet. The step in the curves indicates when the droplets become from disc-shaped (< 80μL) to plug-shaped (> 80μL).

Droplet-based real-time amplification

A series of PCR with template concentration from $6.69x10^3$ copies/μL to $6.69x10^7$ copies/μL have been performed. The real-time fluorescence intensity of the reaction droplet is plotted in Figure 3.9. The trendline of intensity data at each template concentration exhibits a typical amplification profile including an exponential, linear and plateau phase. Moreover, higher template DNA concentrations correspond to an earlier start point of the detectable increase in the fluorescence intensity of the reaction droplet. With a threshold value of fluorescence intensity equal to 1.13 (*i.e.*, the value at which the fluorescence intensity starts increasing above the background signal), the cycle threshold (Ct) is determined using interpolation in Figure 3.9 and plotted in Figure 3.10. The linear relationship between the template DNA concentration and Ct indicates the potential application of quantitative PCR using submicroliter droplets.

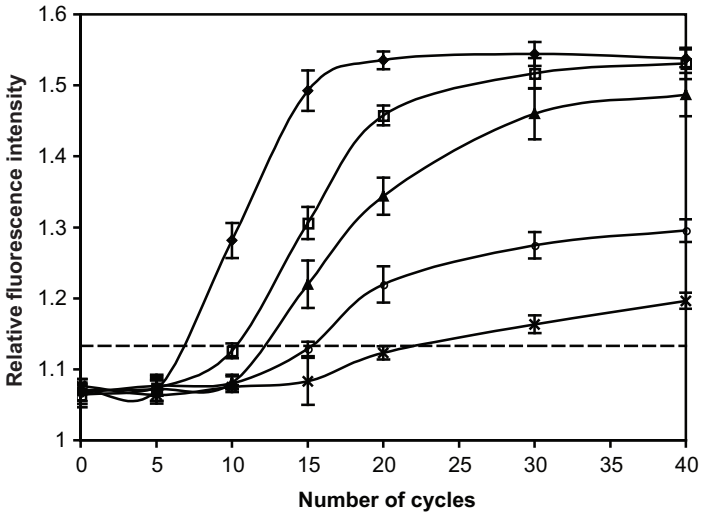

Figure 3.9 Real-time fluorescence intensity of reaction droplet with different template concentration. ◆ 3.5ng/μL (~$6.69x10^7$ copies/μL) of template λDNA; □ 0.35ng/μL (~$6.69x10^6$ copies/μL) of template λDNA; ▲ 0.035ng/μL (~$6.69x10^5$ copies/μL) of template λDNA; ○ $3.5x10^{-3}$ ng/μL (~$6.69x10^4$ copies/μL) of template λDNA; × $3.5x10^{-4}$ ng/μL (~$6.69x10^3$ copies/μL) of template λDNA. The droplet size for all different template concentrations is ~150nL.

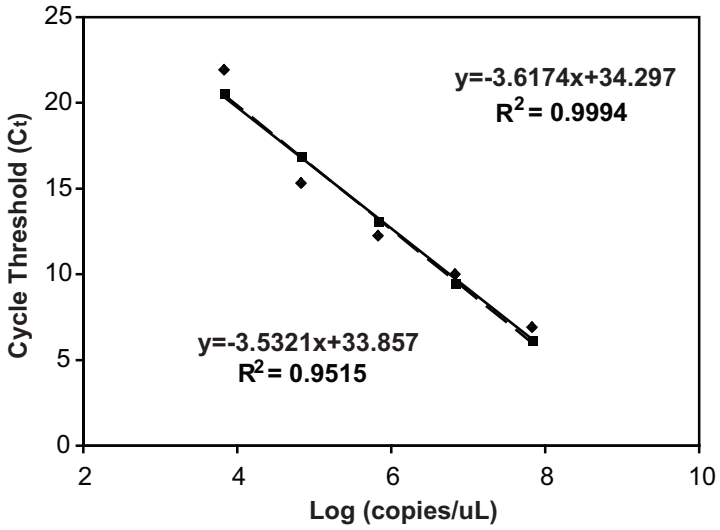

(a)

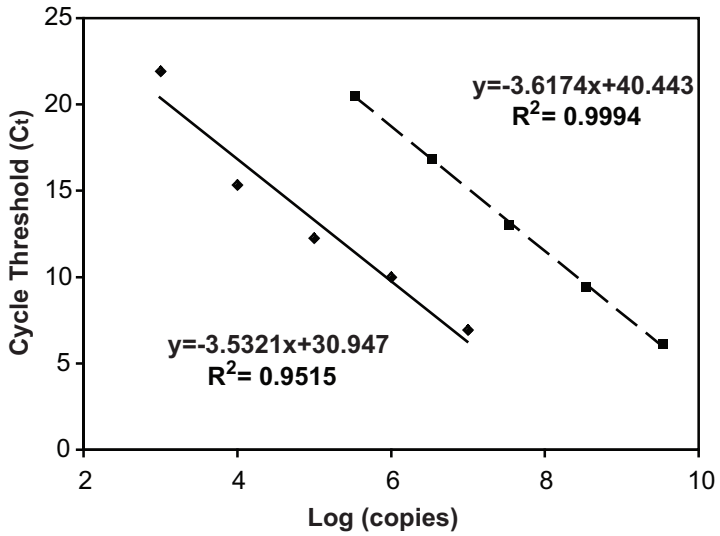

(b)

Figure 3.10 (a) Cycle threshold versus logarithm of template DNA concentration (copies/μL). (b) Cycle threshold versus logarithm of template DNA copy number. In both (a) and (b), ◆ denotes the data obtained using the microdevice, and ■ denotes the data generated on a benchtop instrument; the equation in the top right is for the trendline (dash line) of the benchtop data, and the equation in the bottom left is for the trendline (solid line) of the on-chip data. The benchtop reaction volume is 50μL.

The data with the same template concentration range collected on a benchtop real-time PCR instrument are also plotted in Figure 3.10, in order to compare the performance of the benchtop and droplet-based systems. As shown in Figure 3.10(a), the cycle thresholds obtained in the droplet-based PCR are approximately the same as those generated in the benchtop reactions with the same template DNA concentration. But with the same template DNA copy number, the cycle thresholds obtained in the droplet-based PCR are ~10 cycles earlier than those generated in the benchtop reactions (Figure 3.10(b)), which indicates a faster analysis using our microsystem.

Conclusions

We have successfully performed PCR in on-chip generated single nanoliter sized droplets with on-chip heating and temperature control. Without any microvalves or on-chip sealing components, no volume loss of the reaction droplet has been observed after 40 cycles of PCR. Most importantly, our study adds to previous studies that specifically addressed the dependence of droplet-based PCR amplification efficiency on many of the reaction parameters including reagent concentration, hold time at each temperature step and droplet size. These studies not only provide detailed information on the behavior of this well-characterized bioreaction in a small-scale droplet-based system, but also will aid in optimizing the design and operation of the microfluidic systems. With the optimized reaction parameters, our device demonstrates the sensitivity of detecting the template DNA concentration within a wide concentration range, and the capability of rapid detection using this droplet-based system for real-time quantitative PCR.

References

1. T. Thorsen, R. W. Roberts, F. H. Arnold and S. R. Quake, *Phys. Rev. Lett.*, 2001, **86**, 4163-4166.
2. T. Nisisako, T. Torii and T. Higuchi, *Lab Chip*, 2002, **1**, 24-26.
3. P. Garstecki, M. J. Fuerstman, H. A. Stone and G. M. Whitesides, *Lab Chip*, 2006, **6**, 437-446.
4. S. L. Anna, N. Bontoux, and H. A. Stone, *Appl. Phys. Lett.*, 2003, **82**, 364-366.
5. L. Yobas, S. Martens, W.-L. Ong and N. Ranganathan, *Lab Chip*, 2006, **6**, 1073-1079.
6. T. B. Jones, *J. Electrost.*, 2001, **51-52**, 290-299.
7. R. Ahmed and T. B. Jones, *J. Electrost.*, 2006, **64**, 543-549.
8. M. G. Pollack, R. B. Fair and A. D. Shenderov, *Appl. Phys. Lett.*, 2000, **77**, 1725-1726.
9. M. G. Pollack, A. D. Shenderov, R. B. Fair, *Lab Chip*, 2002, **2**, 96-101.
10. S. K. Cho, H. Moon and C.-J. Kim, *J. Microelectromech. Syst.*, 2003, **12**, 70-80.
11. S.-K. Hsiung, C.-T. Chen and G.-B. Lee, *J. Micromech. Microeng.*, 2006, **16**, 2403-2410.
12. C.-T. Chen and G.-B. Lee, *J. Micorelectromech. Syst.*, 2006, **15**, 1492-1498.
13. Z. Guttenberg, H. Müller, H. Habermüller, A. Geisbauer, J. Pipper, J. Felbel, M. Kielpinski, J. Scriba and A. Wixforth, *Lab Chip*, 2005, **5**, 308-317.
14. U. Lehmann, C. Vandevyver, V. K. Parashar and M. A. M. Gijs, *Angew. Chem. Int. Ed.*, 2006, **45**, 3062-3067.

15. J. Pipper, M. Inoue, L. F.-P. Ng, P. Neuzil, Y. Zhang and L. Novak, *Nat. Med.*, 2007, **13**, 1259-1263.

16. D. R. Link, S. L. Anna, D. A. Weitz and H. A. Stone, *Phys. Rev. Lett.*, 2004, **92**, 054503-1-054503-4.

17. T. H. Ting, Y. F. Yap, N.-T. Nguyen, T. N. Wong, J. C. K. Chai and L. Yobas, *Appl. Phys. Lett.*, 2006, **89**, 234101-234103.

18. H. Yang, C. C. Park, Y. T. Hu and L. G. Leal, *Phys. Fluids.*, 2001, **13**, 1087-1106.

19. L.-H. Hung, K. M. Choi, W.-Y. Tseng, Y.-C. Tan, K. J. Shea and A. P. Lee, *Lab Chip*, 2006, **6**, 174-178.

20. F. Sarrazin, L. Prat, N. D. Miceli, G. Cristobal, D. R. Link and D. A. Weitiz, *Chem. Eng. Sci.*, 2007, **62**, 1042-1048.

21. X. Niu, S. Gulati, J. B. Edel, and A. J. deMello, *Lab Chip*, 2008, **8**, 1837-1841.

22. E. Um and J.-K. Park, *Lab Chip*, 2009, **9**, 207-212.

23. H. Song, M. R. Bringer, J. D. Tice and C. J. Gerdts, *Appl. Phys. Lett.*, 2003, **83**, 4664-4666.

24. M. R. Bringer, C. J. Gerdts, H. Song, J. D. Tice and R. F. Ismagilov, *Phil. Trans. R. Soc. Lond.* A, 2004, **362**, 1087-1104.

25. Y.-C. Tan, J. S. Fisher, A. L. Lee, V. Cristini and A. P. Lee, *Lab Chip*, 2004, **4**, 292-298.

26. D. R. Link, E. Grasland-Mongrain, A. Duri, F. Sarrazin, Z. Cheng, G. Cristobal, M. Marquez and D. A. Weitz, *Angew. Chem. Int. Ed.*, 2006, **45**, 2556-2560.

27. I. Shestopalov, J. D. Tice and R. F. Ismagilov, *Lab Chip*, 2004, **4**, 316-321.

28. E. M. Chan, A. P. Alivisatos and R. A. Mathies, *J. Am. Chem. SOC.*, 2005, **127**, 13854-13861.

29. V. Srinivasan, V. K. Pamula and R.B. Fair, *Lab Chip*, 2004, **4**, 310-315.

30. M. He, J. S. Edgar, G. D. M. Jeffries, R. M. Lorenz, J. P. Shelby and D. T. Chiu, *Anal. Chem.*, 2005, **77**, 1539-1544.

31. M. Chabert and J.-L. Viovy, *Proc. Natl. Acad. Sci.*, 2008, **105**, 3191-3196.

32. P. Kumaresan, C. J. Yang, S. A. Cronier, R. G. Blazej and R. A. Mathies, *Anal. Chem.*, 2008, **80**, 3522-3529.

33. P. S. Dittrich, M. Jahnz and P. Schwille, *ChemBioChem.*, 2005, **6**, 811-814.

34. A. Huebner, M. Srisa-Art, D. Holt, C. Abell, F. Hollfelder, A. J. deMello and J. B. Edel, *Chem. Commun.*, 2007, 1218-1220.

35. B. Zheng, J. D. Tice, S. Roach and R. F. Ismagilov, *Angew. Chem. Int. Ed.*, 2004, **43**, 2508-2511.

36. M. Srisa-Art, A. J. deMello and J. B. Edel, *Anal. Chem.*, 2007, **79**, 6682-6689.

37. N. R. Beer, B. J. Hindson, E. K. Wheeler, S. B. Hall, K. A. Rose, I. M. Kennedy and B. W. Colston, *Anal. Chem.*, 2007, **79**, 8471-8475.

38. N. R. Beer, E. K. Wheeler, L. Lee-Houghton, N. Watkins, S. Nasarabadi, N. Hebert, P. Leung, D. W. Arnold, C. G. Bailey and B. W. Colston, *Anal. Chem.*, 2008, **80**, 1854-1858.

39. S. Mohr, Y.-H. Zhang, A. Macaskill, P. J. R. Day, R. W. Barber, N. J. Goddard, D. R. Emerson, P. R. Fielden, *Microfluid Nanofluid*, 2007, **3**, 611-621.

40. T. Ohashi, H. Kuyama, N. Hanafusa and Y. Togawa, *Biomed Microdevices*, 2007, **9**, 695-702.

41. M. A. Burns, *Science*, 2002, **296**, 1818-1819.

42. F. Wang, M. Yang and M. A. Burns, *Lab Chip*, 2008, **8**, 88-97.

43. V. Avettand-Fènoël, M.-L. Chaix, S. Blanche, M. Burgard, C. Floch, K. Toure, M.-C. Allemon, J. Warszawski and C. Rouzioux, *J. Med. Virol.*, 2009, **81**, 217-223.

44. S. Sivapalasingam, U. Patel, V. Itri, M. Laverty, K. Mandaliya, F. Valentine and S. Essajee, *J. Trop. Pediatrics*, 2007, **53**, 355-358.

45. R. Pal, M. Yang, R. Lin, B. N. Johnson, N. Srivastava, S. Z. Razzacki, K. J. Chomistek, D. Heldsinger, R. M. Haque, V. M. Ugaz, P. Thwar, Z. Chen, K. Alfano, M. Yim, M. Krishnan, A. O. Fuller, R. G. Larson, D. T. Burke, and M. A. Burns, *Lab Chip*, 2005, **5**, 1024-1032.

46. I. Erill, S. Campoy, N. Erill, J. Barbé and J. Aguiló, *Sens. Acutators. B.*, 2003, **96**, 685-692.

47. M. Krishnan, D. T. Burke and M. A. Burns, *Anal. Chem.*, 2004, **76**, 6588-6593.

48. C. J. Beverung, C. J. Radke and H. W. Blanch, *Biophy. Chem.*, 1999, **81**, 59-80.

49. A. R. Prakash, M. Amrein and K. V. I. S. Kaler, *Microfluid. Nanofluid.*, 2008, **4**, 295-305.

50. J. A. Voorthuyzen, K. Kesin, P. Bergveld, *Surf. Sci.*, 1987, **187**, 201-211.

CHAPTER 4

MULTI-LIQUID-PHASE BIOREACTION MICROSYSTEM WITH AUTOMATED ON-CHIP DROPLET OPERATIONS

Introduction

Droplet-based microfluidics is increasingly being studied for applications in chemical and biological assays. A variety of techniques have been exploited to generate and manipulate droplets on-chip.[1-19] For example, T-junction[1-3] and flow focusing[4-5] are two major mechanical approaches that depend on the channel geometry and flow rates to control droplet generation, while electrowetting on dielectric (EWOD) is an electrohydrodynamic (EHD) approach for generating droplets by electronically changing the interfacial energy.[6-8] Benefiting from the on-chip controllable droplet size and the isolation of individual droplets, chemical reactions and bioassays such as nanoparticle synthesis,[14,20-21] cell analysis,[22-23] protein expression[24-25] and DNA/RNA amplification,[26-33] have all been implemented in droplet-based microdevices.

While these droplet-based microsystems have been widely demonstrated to offer robust control and operation, fully automating microystems could make them more amenable to applications in portable, point-of-care diagnosis. A critical step in this automation is fluid detection that includes not only tracking the location and velocity of the fluid, but also, particularly for the droplet-based microsystems, monitoring the droplet

size and generation frequency. One of the most widely used detection methods is optical detection using either charge-coupled device (CCD) camera with microscopy and image analysis or photo diodes for detecting the laser diffraction caused by the presence of droplets.[34] However, the optical techniques usually rely on cumbersome or expensive accessory instruments and cannot be employed on opaque substrates.

Recently, thermal and electronic sensing have been used as alternative approaches to optical detection. Thermal sensing is based on the convective heat loss to the fluid as it passes over a predefined region.[35-37] Heating around the detection region is usually required during thermal sensing, and, therefore, this method may not be practical for biological applications since most bioreagents are temperature-sensitive. Electronic sensing is based on the change of electrical resistance, impedance or capacitance as different liquid phases pass over microfabricated electrode sensors.[37-45] In addition to measuring droplet size and generation frequency, electronic sensing has been used to analyze the composition of the droplets [42-44] and control the droplet flow according to the droplet size and content.[43] Automated droplet generation in electrowetting-based microsystems has also been achieved using electrical capacitance sensing, but most droplet generation using mechanical means are still manually controlled.

In this chapter, we present a droplet-based bioreaction microsystem with automated mechanical means of on-chip droplet generation and confinement. The system uses paired electrodes to electronically track the oil/aqueous interface. The sensor reading not only indicates the location of the liquid interface, but also can be used to control the pneumatic system to generate droplets of precise sizes and position droplets in desired

locations. This automated droplet-based microsystem can be used for a variety of applications including biochemical analysis (e.g., polymerase chain reaction (PCR)).

Materials and Methods

Device fabrication and assembly

Top side (channel) microfabrication

The detailed procedure for fabricating the fluid network on a glass wafer using photolithography and wet chemical etching have been outlined elsewhere.[46] Briefly, a thin metal film (500Å Cr/ 2500Å Au) is deposited and patterned on a glass wafer. The wafer is then etched to the desired depth in hydrofluoric acid (49%) (CMOS grade; J.T. Baker, Philipsburg, NJ). Next, the photoresist and metal layers are removed. The glass wafer is then diced to obtain individual top dies. The dies are coated with a 3μm thick layer of Parylene-C (PDS 1020 Labcoater, Speciality Coating Systems, IN) before bonding it to the bottom dies.

Bottom side (electronics) microfabrication

The electronic components including heaters, resistance temperature detectors (RTDs) and electrodes are fabricated on either a silicon wafer with a 5000Å thick silicon oxide layer or a glass wafer. Firstly, photoresist is patterned on the wafer using photolithography, followed with evaporating 300Å Ti/1000Å Pt for heaters and RTDs. The wafer is then left in acetone (CMOS grade; J.T. Baker, Philipsburg, NJ) to lift off unwanted metal. Next, a second lithography, evaporation and lift-off are conducted to

fabricate the electrodes (500Å Cr/2500Å Au). The wafer is then diced to yield individual bottom dies.

Device assembly

A custom designed printed circuit board (PCB, Advanced Circuits, Aurora, CO) serves as the platform for electrical connections. The bottom die is fixed on the PCB using standard quick cure epoxy, and then wire bonded (Kulicke & Soffa 4124 Ball Bonder) using 1.0 mil gold wire. After wire bonding, the top die is visually aligned to the bottom die, and UV curable optical glue is wicked between the top and bottom dies through the edges. The device is then cured in UV light for 1.5 hours.

Experimental setup and operation

Data acquisition

The setup for data acquisition of the automated droplet-based microsystem consists of a function generator (8165A, Hewlett Packard), a data acquisition (DAQ) board (National instruments PCI 6031E, Austin, TX), a digital relay board (National Instruments ER-16, Austin, TX), a computer and LabVIEW program (National instruments, Austin, TX) (Figure 4.1). Edge connectors from the PCB connect each pair of on-chip electrodes in series with a 120 kΩ external reference resistor; one of the electrodes in each pair is connected to the function generator *via* the digital relay board while the other is grounded. In most experiments, an AC signal (Amplitude = 1.5V, Frequency = 230Hz) from the function generator is applied across the electrodes. The digital relays can selectively shut off the power input to a pair of electrodes. The change

of electrical impedance between two electrodes in each pair is represented by the voltage drop across the reference resistor. This voltage drop is acquired by the LabVIEW VI using the analog input of the DAQ board.

Pneumatic control

The pneumatic control is carried out by adjusting the voltage input to electropneumatic regulators (VSO-EP or VSO-EV; Parker, Cleveland, OH): there is a linear relationship between the input control voltage and the output pressure/vacuum from the regulator. Lab air supply serves as the pneumatic source to the regulator. The pulsing of pressure or vacuum is controlled by a set of three-way solenoid valves (Numatech, Wixom, MI). Opening and closing of the solenoid valves are operated through a combination of a DC power supply (Electro Industries, Model Digi 35A) and a digital relay board (ER-16). Functioning of the relay board and the electropneumatic regulator are both feedback controlled by the voltage signal from the reference resistor through the LabVIEW program using a digital I/O card (National Instrument PCI-DIO-96, Austin, TX) and a DAQ board (National instruments PCI-6704, Austin, TX), respectively.

On-chip temperature control

The on-chip temperature control is also conducted through the LabVIEW program. The RTDs are calibrated by heating the device in a convection oven and recording the temperature-resistance data *via* the PCI 6031E board. The slope and intercept from a linear fit of the temperature and resistance data are read into the control

algorithms that use a proportional-integral (PI) module to control temperature *via* the PCI 6704 board. The heaters are connected to a DC power supply (B+K Precision Model 1760, Yorba Linda, CA) through a signal conditioning circuit that boosts the supply voltage from the computer with an op-amp gain of 3. The precision of temperature control is ± 0.2^{o}C.

Bioreaction and fluorescence detection

PCR amplification

The PCR mixture consists of λDNA template (Invitrogen, Carlsbad, CA) with the concentration of 3.5ng/μL, dNTPs (0.2mM each dATP, dGTP, dCTP and 0.4mM dUTP), 10mM Tris-HCl (pH 8.3), 50mM KCl, 0.01mM EDTA, 3.5mM $MgCl_2$, 0.9μM each primer, 0.25μM probe, 0.01units/μL AmpErase UNG, and 0.175units/μL AmpliTaq Gold® DNA polymerase (Applied Biosystems, Foster City, CA). The sequences of forward and reverse primers are 5'-CATCAAAGCCATGAACAAAGCA-3' and 5'-TCAGCAACCCCGGTATCAG-3', respectively. The sequence of probe is 5'6FAM-CCGCGCTGGATGA-3'MGBNFQA. This size of the target product is 56bp. The thermocycling protocol used in most of the on-chip droplet-based PCR consists of 50°C for 2min, 95°C for 9min, followed by 30 cycles of 95°C for 9s and 60°C for 30s. PCR grade mineral oil (Sigma Aldrich, St. Louis, MO) is used as the continuous oil phase.

Fluorescence detection and data analysis

An inverted fluorescence microscope (Nikon Eclipse TE2000-U) with a 2x objective (Nikon) is used to monitor fluorescence of the reaction droplet. An X-cite

Series 120 lamp (EXFO Life Science Divisions, Ontario, Canada) with FITC filter is used as the excitation source. The fluorescence images are captured using a digital CCD camera (Photometrics Cascade 512F; Roper Scientific, Tucson AZ) with a 500ms exposure time. The relative fluorescence intensity is used to quantify the amplification yield in the droplet, which is calculated by scaling the fluorescence intensity of the droplet by that of the reference area on the device. Data analysis is done by MetaVue Software.

Results and Discussions

Electronic sensing of the oil/aqueous interface

The approach for tracking the oil/aqueous interface in our device is based on the fact that the electrical impedance across two electrodes is dependent on the electrical properties of the fluid above those electrodes. Thus, using a simple electrical circuit (Figure 4.1), the liquid interface can be tracked by measuring the impedance change across a pair of electrodes (each 100μm wide, 50μm apart) microfabricated at pre-determined positions in a fluid channel. The arrangement of those electrodes will affect the way in which the interface location can be measured: electrodes orthogonal to the fluid path produce a "yes/no" signal and electrodes parallel to the fluid path can produce a more complex location signal.

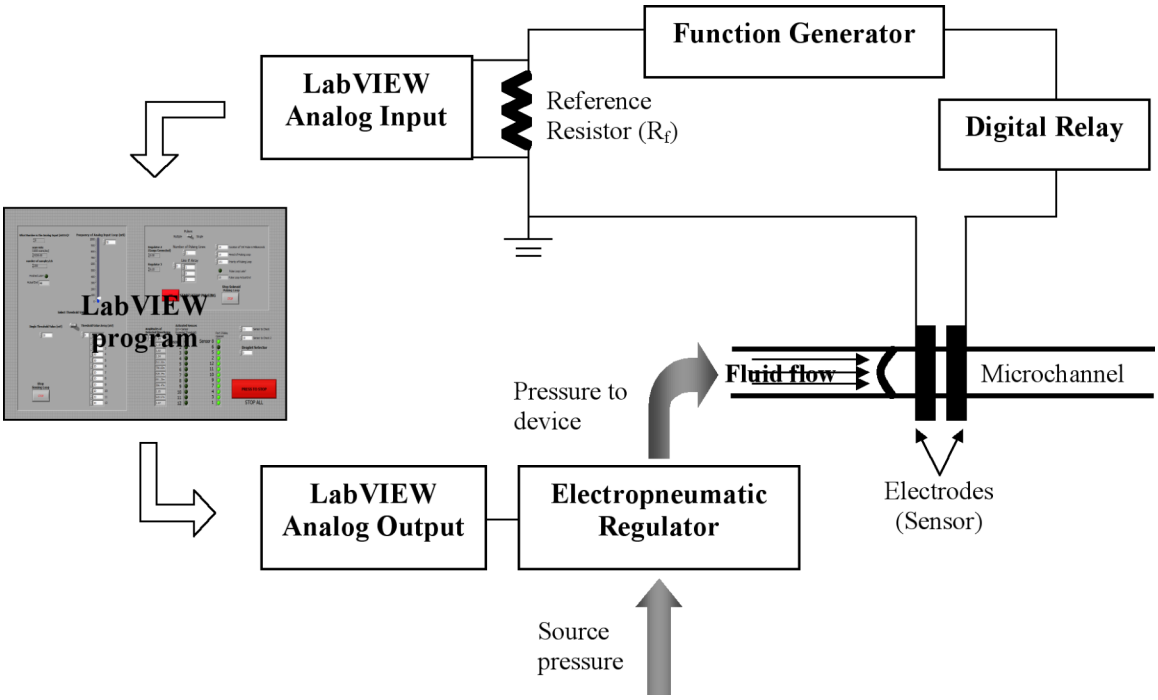

Figure 4.1 Schematic of the automated droplet-based system setup.

Figure 4.2 shows the arrangement and responses of four pairs of electrodes placed orthogonal to the fluid channel. The voltage responses from these sensors when DI water displaces mineral oil in the channel (Figure 4.2(b)) produce characteristic digital ("yes/no") signals. An increase in the output voltage (*i.e.*, the voltage across the reference resistor) is sequentially observed for the four digital sensors as the moving oil/aqueous interface crosses each one. Note that the input signal from the function generator was shut off once the voltage response was above a threshold value to prevent possible damages to the reaction solution.

In this digital sensing method, the digital signal can serve as a switch for the pneumatic control to drive the liquid flow in the device provided a proper voltage threshold is used. The setting of the voltage threshold is determined by the voltage response from the sensor and is affected by the input voltage signal. The output voltage

from a digital sensor with different input frequencies (150~7500Hz) is shown in Figure 4.2(c). The input signals used in the experiment have the same amplitude of 1.5V. With increasing input frequency, the output voltage signal rapidly increases and then gradually decreases when the input frequency is above ~2600 Hz while the base signal (i.e., with only the oil phase) monotonically increases within the tested frequency range. This result indicates that input signals with lower frequencies (< 1kHz) may be more amenable to be used for control since the background (i.e., base signal) is low. In addition, the total cost of the automated microsystem could also be reduced by not requiring high input power and frequency.

The voltage response from the digital sensor may be also affected by the properties of the fluids especially the aqueous phase. As shown in Figure 4.2(c), using buffer solution (10mM Tris·HCl) with different pH values (pH=7.0, 7.5, 8.0, 9.0), the voltage signal increases with the decreasing pH values at a fixed input frequency. This trend can be explained by the fact that the ion concentration of the buffer solution also increases with the decreasing pH values. Higher ion concentration results in lower electrical impedance across the electrodes and thus higher voltage drop across the reference resistor. This result also indicates a detection sensitivity of a pH difference of 0.5 or an ion concentration difference less than 1.5mM. Moreover, since the buffer solution is one of the most common reagents involved in bioreactions and its pH value varies according to the applications, this system can be used to track and sort droplets containing different solutions or reagents.

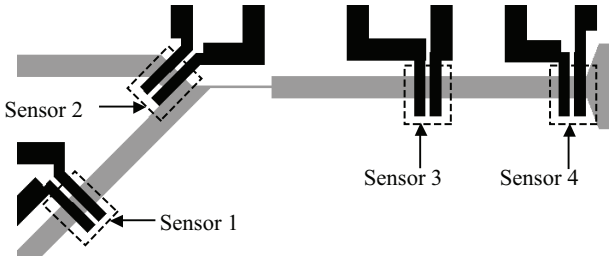

(a)

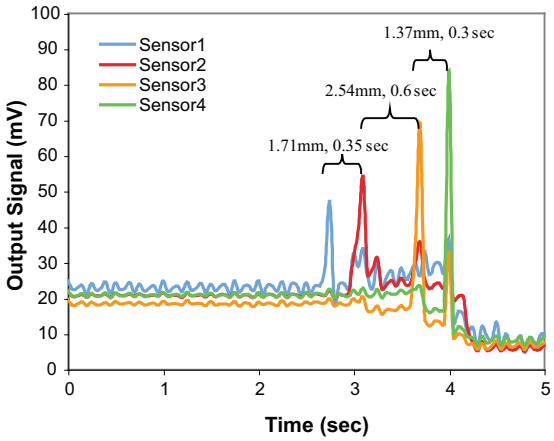

(b)

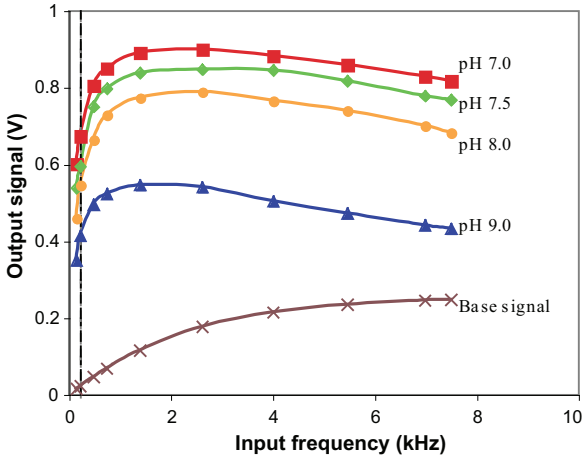

(c)

Figure 4.2 (a) Layout of the location of four digital sensors (outlined by dashed lines). (b) Output signal from the four sensors when the oil/water interface passes over. The input signal to the sensors is shut off if the output signal is above the threshold value of 40mV. The labels of length and time on top of the signal peaks denote the distance between the adjacent sensors and the time interval for tripping the adjacent sensors. (c) Effects of the frequency of input signal and the pH of buffer solution (10mM Tris·HCl). The input signal is a sine-wave AC signal with an amplitude of 1.5V. The ion concentration of buffer solution is 9.19mM, 7.84mM, 5.34mM and 1.03mM for pH equal to 7.0 (■), 7.5 (◆), 8.0 (●) and 9.0 (▲), respectively. The dashed line indicates the frequency (230 Hz) used in the automated device operation.

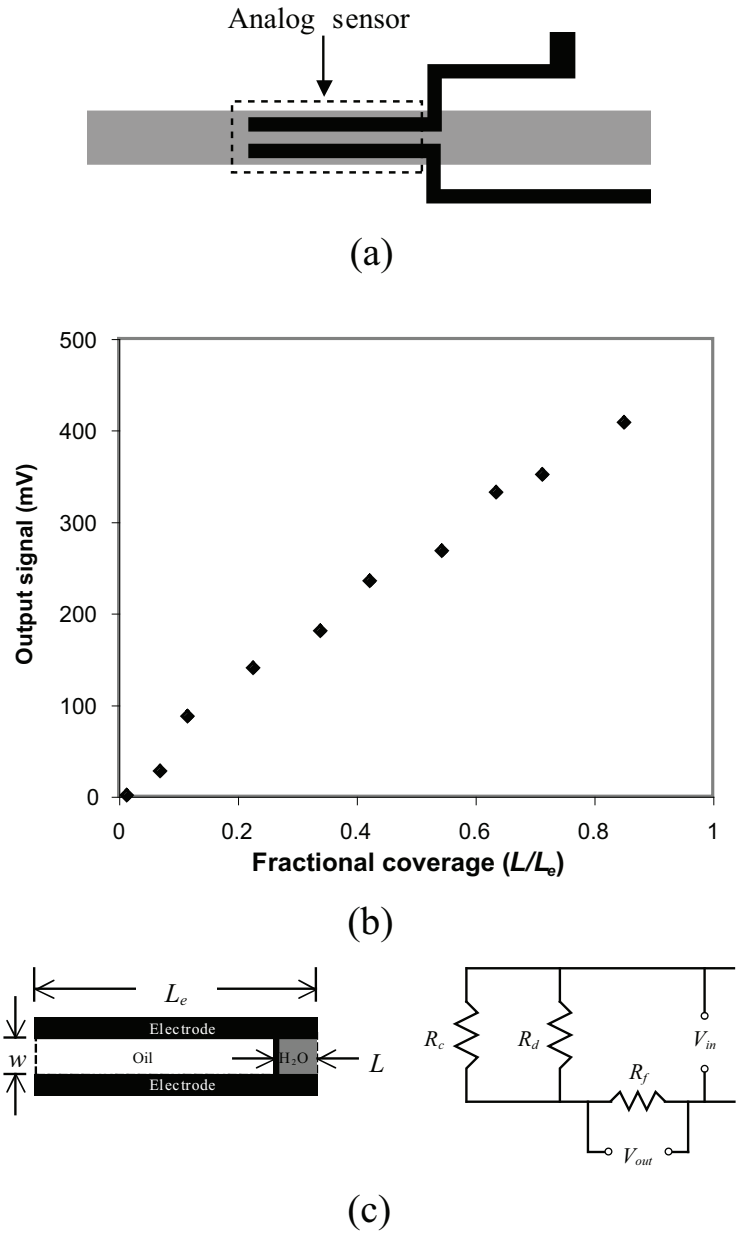

Figure 4.3 (a) Layout of the analog sensor (outlined by dash line). (b) Output signal of the analog sensor versus the droplet coverage across the electrodes. (c) Diagram of simplified circuit model for the analog sensing. w is the gap between the electrodes; L is the length of the aqueous phase covering the electrodes; L_e is the length of the electrode; R_c and R_d are the resistance of the oil and aqueous phase between the electrodes, respectively; R_f is the resistance of the external reference resistor; V_{in} is the voltage input to the analog sensors; V_{out} is the voltage drop across the reference resistor.

In the analog sensing method, the voltage response from electrodes parallel to the fluid channel (Figure 4.3(a)) is proportional to the coverage of aqueous phase over the two electrodes (Figure 4.3(b)). As shown in Figure 4.3(c), the oil and aqueous phases between the two electrodes can be treated as two resistors (R_c and R_d, respectively) connected in parallel. We also assume no phase shift between the voltage and current, and thus the impedance (Z) equals the resistance (R). Since the resistivity of mineral oil ($\sim 10^{11}$ Ω·m) is much higher than that of water (1.82×10^5 Ω·m), the current through R_c can be neglected. Moreover, the resistance of the reference resistor (R_f) is 120 kΩ, much smaller than that of the aqueous phase between the two electrodes (R_d) (on the order of at least 10^5 kΩ).

Therefore, the output signal (V_{out}) can be approximated using Eq. 4.1:

$$V_{out} = \frac{R_f}{R_d} V_{in}. \tag{4.1}$$

Here, V_{in} is the voltage signal input to the two electrodes and

$$R_d = \rho \frac{w}{Lh} \tag{4.2}$$

where ρ is the electrical resistivity of water, w is the gap between the two electrodes, L is the length of water coverage along the electrodes, and h is the depth of the channel. Substituting Eq. 4.2 into Eq. 4.1 produces

$$V_{out} = \frac{R_f V_{in} L h}{\rho w}. \tag{4.3}$$

Thus, V_{out} is linearly proportional to L or the fractional coverage L/L_e (L_e is the length of the electrode). This electronic signal accurately corresponds to the location of the oil/aqueous interface and can be used to precisely control the position of droplets.

However, calibration may be required for different aqueous phases based on their electrical conductivity for use in such control.

Automated droplet generation

This electronic sensing can be used to automate droplet generation in conjunction with computer-controlled pneumatic system, as shown in Figure 4.4. First, pneumatic control (P_{H2O}) is switched on to inject aqueous solution (DI water) into the oil-filled channel (Figure 4.4(a)), after desired droplet size is chosen. Once the oil/aqueous interface passes over the appropriate sensor (Sensor 11), pressure (P_{Oil}) is also applied to facilitate the aqueous solution passing the neck region and prevent the aqueous solution from entering the oil reservoir (Figure 4.4(b)). When the target sensor (Sensor 9) is tripped, P_{H2O} is switched off and P_{Oil} is increased to quickly break the aqueous stream (Figure 4.4(c) and (d)). Once the aqueous phase is sensed back to the reservoir (*i.e.*, Sensor 3 becomes untripped), vacuum is applied through the outlet to pull the aqueous slug into the chamber (Figure 4.4(e)). After the entire droplet has entered the chamber (*i.e.*, Sensor 7 becomes tripped and then untripped), both the pneumatic supply and digital sensing are turned off and the droplet generation is complete (Figure 4.4(f)).

Our device is designed to automatically generate four different sized droplets corresponding to four digital sensors (Sensor 7-10) in the main channel. As shown in Figure 4.5, the size of automatically generated droplets are quite close to the designed droplet size (a standard deviation less than 3% of the droplet size). Moreover, the pneumatic control is triggered by computer signals and is significantly faster than manual operations. This automated droplet generation can be completed in 2-3 seconds, and is

much faster than the manual generation (at least 10 seconds). In addition, since the only manual part of the operation is choosing droplet size in the program, even a user without any professional training should be able to generate droplets using this system.

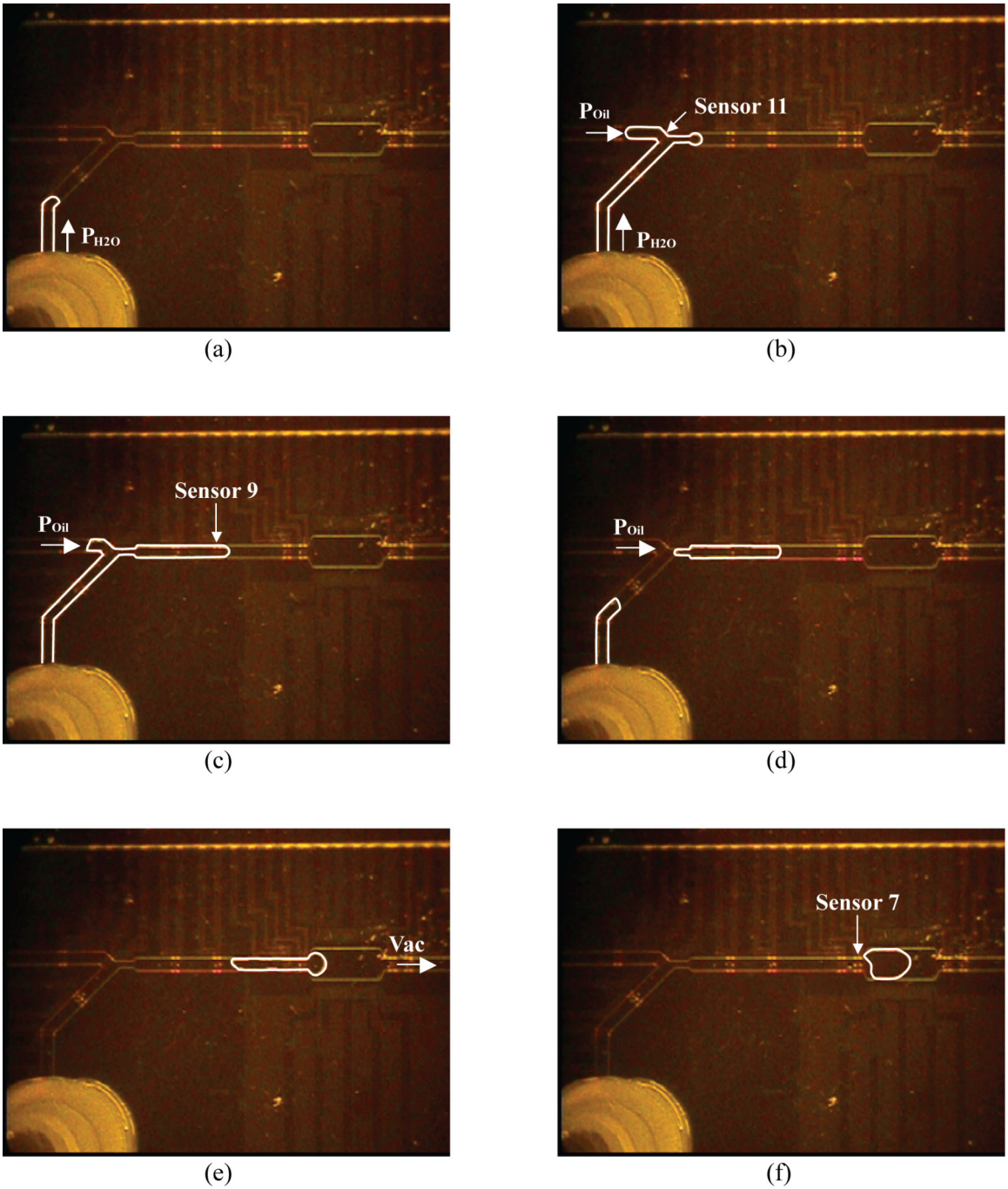

Figure 4.4 Snapshots of the automated droplet generation.

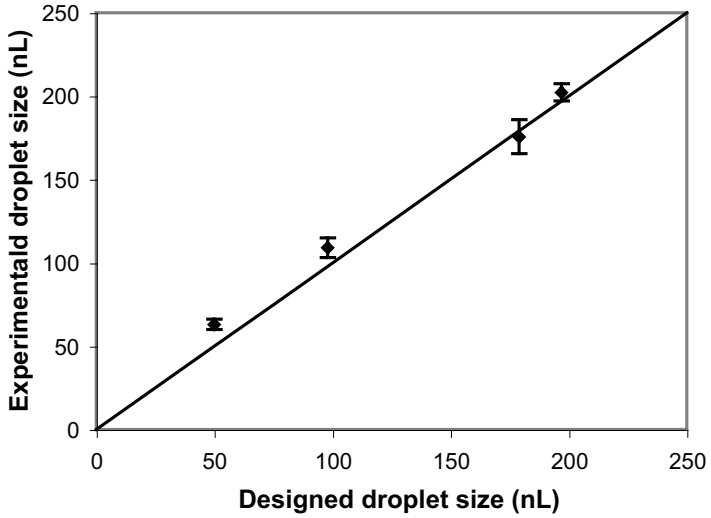

Figure 4.5 Comparison between the designed droplet size and the size of automated generated droplet. The straight line denotes that the experimental droplet size equals to the designed droplet size. The error bar represents the standard deviation.

The effect of pneumatic parameters on the droplet formation time and droplet size is shown in Figure 4.6. In this experiment, designed droplet sizes of 98nL and 197nL were used, and the ratio of pressure through both phases (P_{Oil} and P_{H2O}) was chosen as 1 to simplify system operation. The formation time for both sized droplets decreases with increasing pressures (Figure 4.6(a) and (b)). At high pressures, the actual droplet size varies from the original designed size with the larger droplets (197nL) being below their designed size and the smaller droplets (98nL) being above (Figure 4.6(c)). However, this size variation is not obvious within a pressure range of 0.6-0.75 psig, indicating that the pneumatic control responds rapidly enough that the applied pressure does not limit the performance of our system. In contrast, most droplet-based microsytems adjust the pressure to control droplet size. That technique then requires a calibration to relate the applied pressure to droplet size and produces non-uniform sized droplet during startup.

The size variation in our system with higher applied pressure could be associated with the neck region at the T-junction. This neck is designed to provide higher shear rate to facilitate the breakup of the aqueous stream, but it also increases flow resistance. When the aqueous phase reaches the T-junction, P_{Oil} is switched on to force the aqueous phase to flow through the neck region instead of into the oil phase channel. The left oil/aqueous interface needs to be maintained at the T-junction till the right interface reaches the target sensor in the main channel. However, when generating larger droplets (*e.g.*, 197nL), if P_{Oil} is too high, the aqueous stream may be split at the neck before the right interface reaches the target sensor, producing droplets smaller than the designed size. Also, when forming smaller droplets (*e.g.*, 98nL), if P_{H2O} is too high, the aqueous stream may overshoot the target sensor, making the actual droplet size larger.

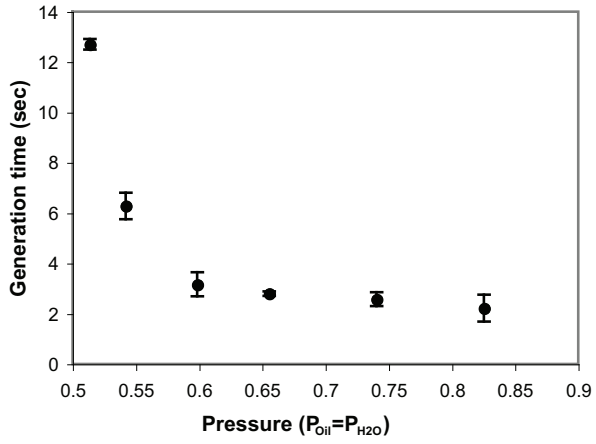

(a)

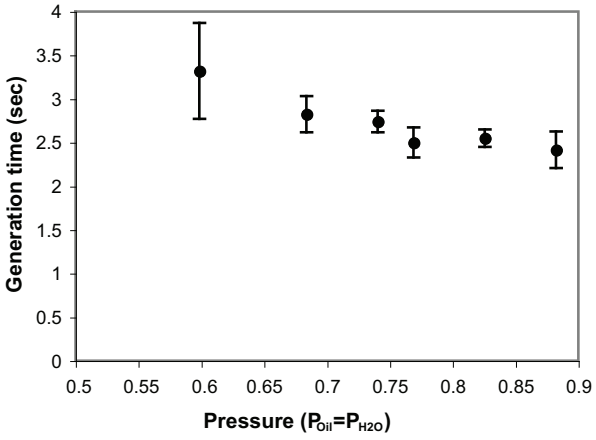

(b)

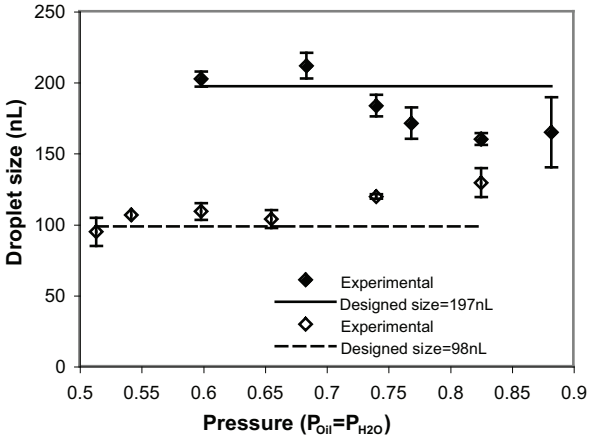

(c)

Figure 4.6 (a)-(b) Effect of pressure on the droplet formation time. (c) Effect of pressure on the droplet size.

Bioreaction with automated position control

In addition to automated droplet generation, the combination of droplet sensing and controlled pressure sources can be used to maintain droplet position in microfluidic bioreaction systems. Ideally, droplets need to stay in the temperature-controlled reaction region in order for the reagents to reach and maintain the desired temperature. However, temperature variations during liquid heating and cooling can cause droplet motion[47] and cause the droplet to be displaced from the reaction region. Confinement of the droplet is possible but requires additional fabrication steps in order to include valves or other sealing systems. Using our system, droplet location can be controlled using electronically triggered pneumatic pulses. The sensors indicate the location of the droplets and pressure pulses are used to prevent the droplets from leaving the reaction region.

The automated confinement of droplet using digital sensing during temperature cycling is shown in Figure 4.7. Pressure is applied from left to right when only Sensor 8 (Figure 4.7(a)) reads "True", and from right to left when only Sensor 5 reads "True". At room temperature, the droplet stays between Sensor 5 and 8 (Figure 4.7(b)). At 95^{o}C, the droplet expands and almost reaches Sensor 5, turning on the pneumatic control. The droplet then oscillates between Sensor 5 and 8 because one of the two sensors is always tripped (Figure 4.7(b)). When temperature decreases from 95^{o}C to 55^{o}C, the oscillation frequency and distance of the droplet also decrease. When the temperature reaches 55^{o}C, the droplet remains between Sensor 5 and 8, and the pneumatic oscillations cease.

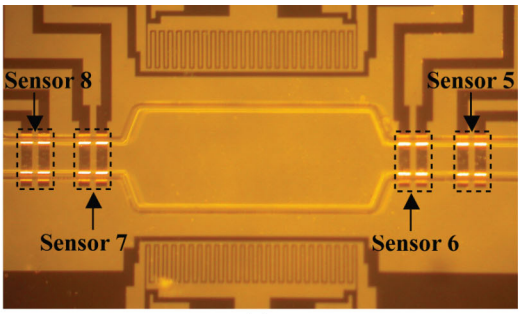

(a)

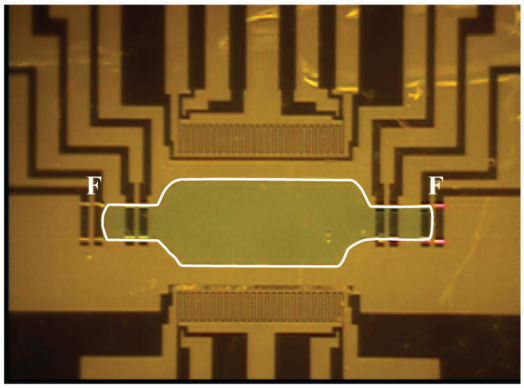

(b)

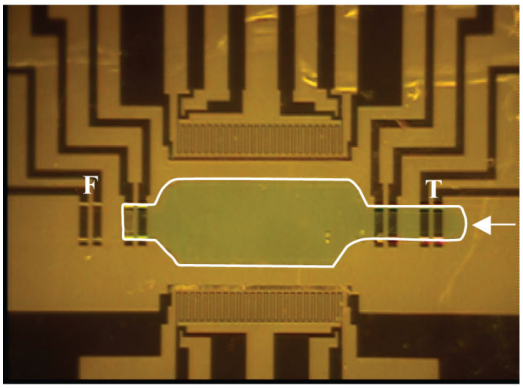

(c)

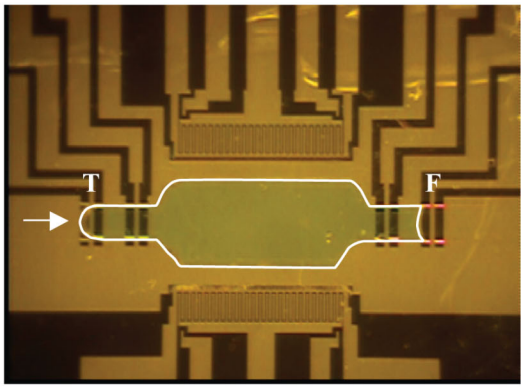

(d)

Figure 4.7 (a) Image of the reaction region with four digital confinement sensors. (b) Snapshot of the droplet at room temperature. (c)-(f) Confinement of the droplet during thermal cycling.

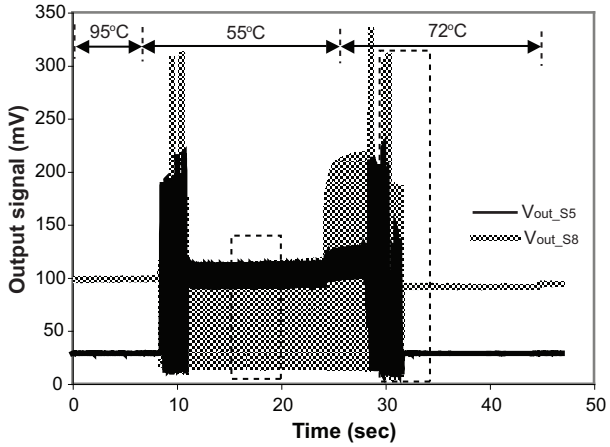

(a)

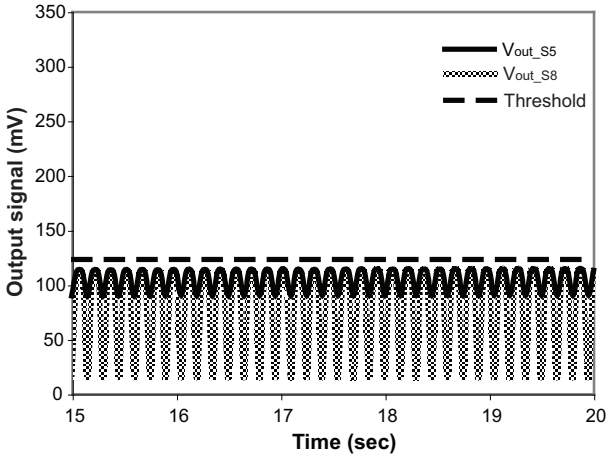

(b)

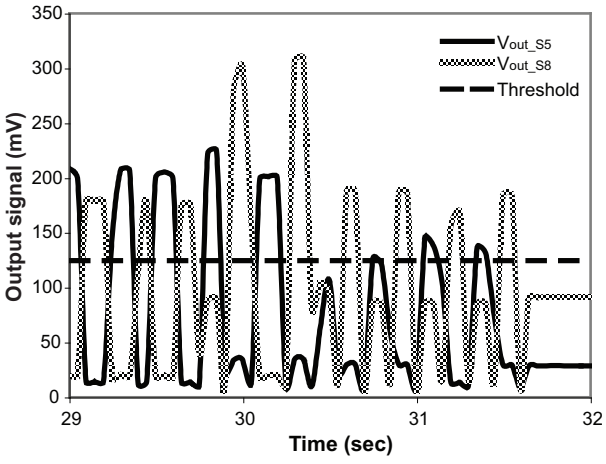

(c)

Figure 4.8 (a) The output signal from Sensor 5 and 8 during the automated droplet confinement. (b) Zoom-in of the left inset in (a). (c) Zoom-in of the right inset in (a).

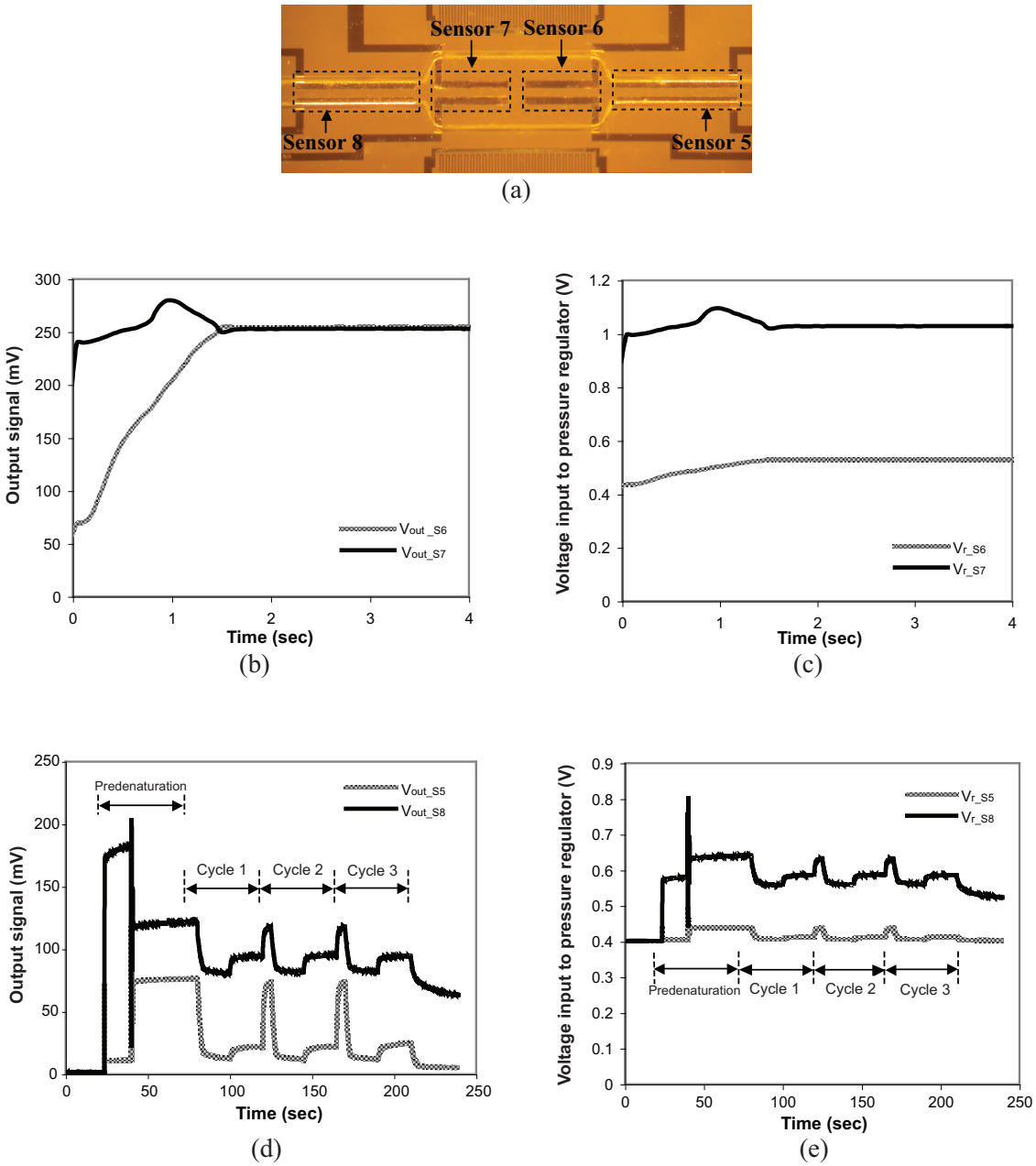

Figure 4.9 (a) Image of the reaction region with four analog confinement sensors. (b) Sensor output signal and (c) voltage input to the electropneumatic regulator when Sensor 6 and 7 are monitored during the droplet confinement. K_p=0.0005 (V_r_S6); K_p=0.0025 (V_r_S7); K_i=0. (d) Sensor output signal and (e) voltage input to the electropneumatic regulator when Sensor 5 and 8 are monitored during the droplet confinement with thermal cycling. K_p =0.0005 (V_r_S5); K_p =0.001 (V_r_S8); K_i=0.

The voltage signals of Sensor 5 and 8 during one thermal cycle with automated confinement are plotted in Figure 4.8(a). If both sensors read "T" or "F" at the same time

(Figure 4.8(b)), which indicates that the droplet is essentially centered in the chamber, the pneumatic control will remain off. If Sensor 5 and 8 read "T" alternatively (Figure 4.8(c)), pressure will be applied from right and left correspondingly thus causing the droplet to oscillate between the two sensors. It is difficult to completely prevent the droplet from oscillating while using digital sensing because the pressure is controlled digitally (i.e., either on or off). However, this oscillation can result in favorable mixing of the components inside the droplet.[48-49]

The droplet can also be positioned using analog sensing signals and feedback pneumatic control. The electrodes in Sensors 5-8 are parallel rather than orthogonal to the channel (Figure 4.9(a)). A proportional-integral (PI) control module (Eq. 4) is used to adjust the applied pressure in real time according to the location of the droplet and offers finer positioning than the digital sensing based approach.

$$V_{r,n} = K_p(V_{out,n} - V_{out,0}) + K_i \sum_n (V_{out,n} - V_{out,0}) \quad (4.4)$$

In Eq. 4.4, $V_{r,n}$ is the voltage input to the electropneumatic regulator, K_p and K_i are the proportional and integral coefficients, respectively, $V_{out,n}$ is the measured signal from the analog sensor, and $V_{out,0}$ is the base signal from the analog sensor (*i.e.*, the output signal when the sensor is completely covered by mineral oil).

With the analog sensing based feedback control, the droplet can be centered in the chamber without oscillation. As shown in Figure 4.9(b), the output signals from Sensor 6 and 7 reach the same value after ~1.5sec, indicating the droplet volumes covering Sensor 6 and 7 are equal, and thus the droplet is symmetrically located relative to the microheaters. The voltage input to the electropneumatic regulator shows a curve similar to the output signal of related sensors (Figure 4.9(c)). The difference between the two

input voltages even after 1.5sec is because different proportional coefficients are used for the two sensors, taking account of the different flow resistance in the left and right sides of the chamber. Another interesting result is that, during thermal cycling, both the sensor reading and regulator input voltage show a cycled profile similar to the temperature, indicating our system was able to capture and respond to the change of droplet volume caused by temperature changes (Figure 4.9(d) and (e)).

With the droplet generation and positioning automated by electronic sensing, bioreactions can be performed in the droplet-based system. Automatically generated droplets (98nL and 197nL) containing PCR reaction mixture show significant increase of fluorescence intensity after 30 temperature cycles (Figure 4.10(a)-(c)). This increase is approximately the same as that in manually generated droplets (data not shown), which suggests that the input voltage signal during droplet generation did not interfere with the reaction. During the droplet confinement, the amplification was inhibited, but the yield reduction was not significant (Figure 4.10(d)). On the other hand, the amplification yield was much lower in the analog sensing device, although no difference has been observed between with and without input electrical signals. A similar inhibition has been observed when using platinum electrodes.[50] One possible explanation to this yield drop is that the droplet is exposed to a much larger surface area of gold electrode in the analog sensing device, and the enzyme loss becomes more severe since the gold surface binds some functional groups of amino acids (*e.g.*, thiol (-SH)) with quite high affinity.[51] Indeed, the fluorescence intensity can be increased to approximately the same as in the digital sensing device by increasing the enzyme concentration (Figure 4.10(d)). Surface passivation or changing the electrode size could also reduce enzyme loss.

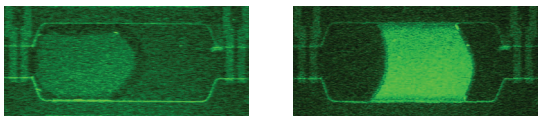

(a)

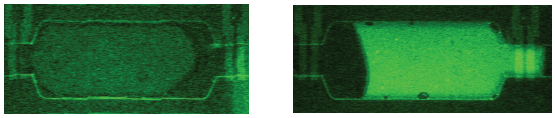

(b)

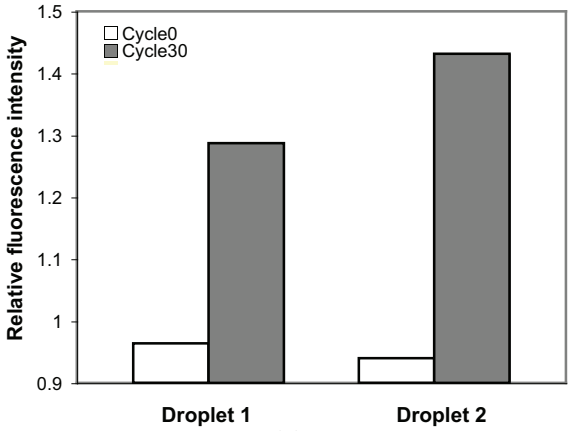

(c)

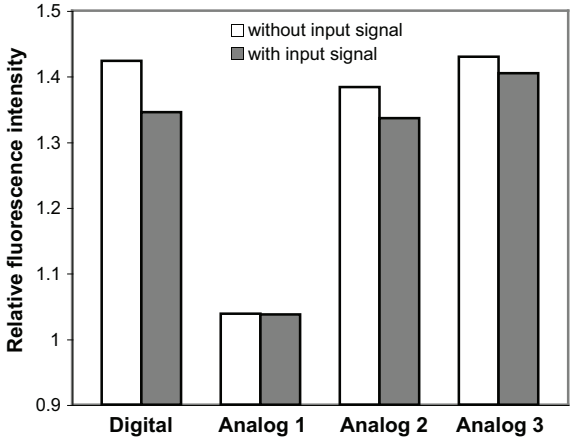

(d)

Figure 4.10 (a) Images of Droplet 1 (designed size of 98nL) at cycle 0 (left) and cycle 30 (right). (b) Images of Droplet 2 (designed size of 197nL) at cycle 0 (left) and cycle 30 (right). (c) The relative fluorescence intensity of the automated generated droplets at cycle 0 and cycle 30. (d) The relative fluorescence intensity of the droplets with and without input voltage in the digital and analog sensing devices. Digital denotes the reaction product with enzyme concentration of 0.175 U/μL in the digital sensing device. Analog 1, Analog 2 and Analog 3 denote the reaction product with enzyme concentration of 0.175 U/μL, 0.35U/μL, and 0.7 U/μL in the analog sensing device.

Conclusions

We have developed a droplet-based microsystem with automated mechanical means of droplet generation and manipulation. On-chip electronic sensing is employed to track the liquid-liquid interface and trigger the pneumatic control to generate and position droplets. With the electronic sensing, no visualization equipment is required, facilitating computerized operation of the microdevice. Moreover, in our system the automated generation of droplets is achieved using digital sensing, and the size of the droplets is in nanoliter scale. Indeed, the droplet size range can be easily expanded by controlling the geometry (including the electrode width and the gap between the paired electrodes) and location of the paired electrodes. For example, smaller droplets can be generated with two thinner electrodes located closer to the slanted T-junction. However, the capability and resolution of the fabrication tools also have to be taken into account for designing the geometry of the electrodes. PCR reaction in the automated generated droplet shows no inhibition caused by the electronic sensing during the droplet generation. Although the reaction was interfered adversely during the droplet confinement especially while using the analog sensing method, adding additional reagents can effectively alleviate the inhibition. Our system demonstrates a successful integration of the automated droplet operation and bioreaction, and could provide portable and automated operation of droplet-based bioassays.

References

1. T. Thorsen, R. W. Roberts, F. H. Arnold and S. R. Quake, *Phys. Rev. Lett.*, 2001, **86**, 4163-4166.
2. T. Nisisako, T. Torii and T. Higuchi, *Lab Chip*, 2002, **1**, 24-26.
3. P. Garstecki, M. J. Fuerstman, H. A. Stone and G. M. Whitesides, *Lab Chip*, 2006, **6**, 437-446.
4. S. L. Anna, N. Bontoux, and H. A. Stone, *Appl. Phys. Lett.*, 2003, **82**, 364-366.
5. L. Yobas, S. Martens, W.-L. Ong and N. Ranganathan, *Lab Chip*, 2006, **6**, 1073-1079.
6. M. G. Pollack, R. B. Fair and A. D. Shenderov, *Appl. Phys. Lett.*, 2000, **77**, 1725-1726.
7. M. G. Pollack, A. D. Shenderov, R. B. Fair, *Lab Chip*, 2002, **2**, 96-101.
8. S. K. Cho, H. Moon and C.-J. Kim, *J. Microelectromech. Syst.*, 2003, **12**, 70-80.
9. T. B. Jones, *J. Electrost.*, 2001, **51-52**, 290-299.
10. R. Ahmed and T. B. Jones, *J. Electrost.*, 2006, **64**, 543-549.
11. D. R. Link, S. L. Anna, D. A. Weitz and H. A. Stone, *Phys. Rev. Lett.*, 2004, **92**, 054503-1-054503-4.
12. T. H. Ting, Y. F. Yap, N.-T. Nguyen, T. N. Wong, J. C. K. Chai and L. Yobas, *Appl. Phys. Lett.*, 2006, **89**, 234101-234103.
13. H. Yang, C. C. Park, Y. T. Hu and L. G. Leal, *Phys. Fluids.*, 2001, **13**, 1087-1106.
14. L-H. Hung, K. M. Choi, W.-Y. Tseng, Y.-C. Tan, K. J. Shea and A. P. Lee, *Lab Chip*, 2006, **6**, 174-178.

15. F. Sarrazin, L. Prat, N. D. Miceli, G. Cristobal, D. R. Link and D. A. Weitiz, *Chem. Eng. Sci.*, 2007, **62**, 1042-1048.

16. H. Song, M. R. Bringer, J. D. Tice and C. J. Gerdts, *Appl. Phys. Lett.*, 2003, **83**, 4664-4666.

17. M. R. Bringer, C. J. Gerdts, H. Song, J. D. Tice and R. F. Ismagilov, *Phil. Trans. R. Soc. Lond.* A, 2004, **362**, 1087-1104.

18. Y.-C. Tan, J. S. Fisher, A. L. Lee, V. Cristini and A. P. Lee, *Lab Chip*, 2004, **4**, 292-298.

19. D. R. Link, E. Grasland-Mongrain, A. Duri, F. Sarrazin, Z. Cheng, G. Cristobal, M. Marquez, D. A. Weitz, Angew. Chem. Int. Ed. **45**, 2556-2560 (2006)

20. I. Shestopalov, J. D. Tice and R. F. Ismagilov, *Lab Chip*, 2004, **4**, 316-321.

21. E. M. Chan, A. P. Alivisatos and R. A. Mathies, *J. Am. Chem. SOC.*, 2005, **127**, 13854-13861.

22. M. He, J. S. Edgar, G. D. M. Jeffries, R. M. Lorenz, J. P. Shelby and D. T. Chiu, *Anal. Chem.*, 2005, **77**, 1539-1544.

23. M. Chabert and J.-L. Viovy, *Proc. Natl. Acad. Sci.*, 2008, **105**, 3191-3196.

24. P. S. Dittrich, M. Jahnz and P. Schwille, *ChemBioChem.*, 2005, **6**, 811-814.

25. A. Huebner, M. Srisa-Art, D. Holt, C. Abell, F. Hollfelder, A. J. deMello and J. B. Edel, *Chem. Commun.*, 2007, 1218-1220.

26. P. Kumaresan, C. J. Yang, S. A. Cronier, R. G. Blazej and R. A. Mathies, *Anal. Chem.*, 2008, **80**, 3522-3529.

27. M. Srisa-Art, A. J. deMello and J. B. Edel, *Anal. Chem.*, 2007, **79**, 6682-6689.

28. Z. Guttenberg, H. Müller, H. Habermüller, A. Geisbauer, J. Pipper, J. Felbel, M. Kielpinski, J. Scriba and A. Wixforth, *Lab Chip*, 2005, **5**, 308-317.

29. U. Lehmann, C. Vandevyver, V. K. Parashar and M. A. M. Gijs, *Angew. Chem. Int. Ed.*, 2006, **45**, 3062-3067.

30. J. Pipper, M. Inoue, L. F.-P. Ng, P. Neuzil, Y. Zhang and L. Novak, *Nat. Med.*, 2007, **13**, 1259-1263.

31. N. R. Beer, B. J. Hindson, E. K. Wheeler, S. B. Hall, K. A. Rose, I. M. Kennedy and B. W. Colston, *Anal. Chem.*, 2007, **79**, 8471-8475.

32. N. R. Beer, E. K. Wheeler, L. Lee-Houghton, N. Watkins, S. Nasarabadi, N. Hebert, P. Leung, D. W. Arnold, C. G. Bailey and B. W. Colston, *Anal. Chem.*, 2008, **80**, 1854-1858.

33. F. Wang and Mark A. Burns, *Biomed. Microdevices*, 2009, **11**, 1071-1080.

34. N.-T. Nguyen, S. Lassemono and F. A. Chollet, *Sens. Actuators. B*, 2006, **117**, 431-436.

35. H. Ernst, A. Jachimovicz and G. A. Urban, *Sens. Actuators. A*, 2002, 100, 54-62.

36. D. N. Pagonis, G. Kaltsas and A. G. Nassiopoulou, *J. Micromech. Microeng.*, 2004, **14**, 793-797.

37. N. Srivastava and M. A. Burns, *Lab Chip*, 2006, **6**, 744-751.

38. J. Z. Chen, A. A. Darhuber, S. M. Troain and S. Wagner, *Lab Chip*, 2004, **4**, 473-480.

39. H. Ren, R. B. Fair and M. G. Pollack, *Sens. Actuators. B*, 2004, **98**, 319-327.

40. J. Collins and A. P. Lee, *Lab Chip*, 2004, **4**, 7-10.

41. J. D. Salgado, K. Horiuchi and P. Dutta, *J. Micormech. Microeng.*, 2006, **16**, 920-928.

42. C. Luo, X. Yang, Q. Fu, M. Sun, Q. Ouyang, Y. Chen and H. Ji, *Electrophoresis*, 2006, **27**, 1977-1983.

43. X. Niu, M. Zhang, S. Peng, W. Wen and P. Sheng, *Biomicrofluidics*, 2007, **1**, 044101-044112.

44. S. Liu, Y. Gu, R. B. Le Roux, S. M. Matthews, D. Bratton, K. Yunus, A. C. Fisher and W. T. S. Huck, *Lab Chip*, 2008, **8**, 1937-1942.

45. J. Gong and C.-J. Kim, *Lab Chip*, 2008, **8**, 898-906.

46. R. Pal, M. Yang, R. Lin, B. N. Johnson, N. Srivastava, S. Z. Razzacki, K. J. Chomistek, D. Heldsinger, R. M. Haque, V. M. Ugaz, P. Thwar, Z. Chen, K. Alfano, M. Yim, M. Krishnan, A. O. Fuller, R. G. Larson, D. T. Burke, and M. A. Burns, *Lab Chip*, 2005, **5**, 1024-1032.

47. T. S. Sammarco and M. A. Burns. *AICHE Journal*, 1999, **45**, 350-366.

48. K. Handique and M. A. Burns. *J. Micromech. Microeng.*, 2001, **11**, 548-554.

49. M. Rhee and M. A. Burns. *Langmuir*, 2008, **24**, 590-601.

50. T. H. Fang, N. Ramalingam, X.-D. Dong, T. S. Ngin, X. Zeng, A. T. L. Kuan, E. Y. P. Huat and H.-Q Gong, *Biosens. Bioelectron.*, 2009, **24**, 2131-2136.

51. H. Elwing, *Biomaterials*, 1998, **19**, 397-406.

CHAPTER 5

DROPLET-BASED MICROSYSTEM FOR MULTI-STEP BIOREACTIONS

Introduction

Over the past decade, microfluidic formation of liquid droplets in a second liquid phase has found many applications in chemical and biochemical reactions and assays[1-11]. The size and generation frequency of these droplets are mostly controlled by adjusting the flow rates and channel geometry of the microfabricated device[12-13]. In electrowetting-on-dielectric (EWOD) systems, the control is performed by electronically changing the interfacial energy [13-16]. Splitting, merging and sorting of droplets have also been achieved using these control methods[3, 5, 17-22]. Other driving sources for droplet generation and manipulation have been used such as dielectrophoresis (DEP)[23-24], surface acoustic wave (SAW)[25-26] and magnetic force[27-28]. Relying on the controllable two-phase microfluidics, the droplet-based microsystems offer advantages in reducing and isolating reaction volumes, preventing evaporation and adsorption, and improving mixing and reaction efficiencies.

Controllable droplet merging and mixing are crucial to successfully performing chemical and biochemical reactions in the droplets, and both passive and active methods have been developed. In passive droplet merging, the drainage of the continuous phase between two droplets is promoted by changing the channel geometry or adding channel

structures[5, 18-20, 22]. Active droplet merging can be achieved by actively guiding the droplets towards each other in EWOD[14], SAW[25] or magnetic-based[27-28] systems. As is known, diffusive mixing is dominant in microscale and can be excessively slow in spite of the short diffusion distances. In a droplet-based microsystem, mixing can be accelerated using passive methods by flowing the droplets through certain shaped channels to induce internal circulation and chaotic advection[19, 29-32]. In EWOD, SAW and magnetic-based droplet systems, mixing can also be completed by actively moving the droplets along a certain path[25, 27-28, 33].

Droplet-based microsystems integrated with droplet merging and mixing are ideal for chemical and biochemical applications that require controllable addition of reagents, for example, in aggressive or fast reaction and kinetic studies[5, 25, 28, 34-35]. These systems are also highly amenable to multi-step reactions. In fact, many bioassays include more than one reaction step. However, only synthesis of core-shell nanoparticles has been reported using a droplet-based two-step reaction[36]. Moreover, most droplet-based applications use small (*e.g.*, picoliter-sized) droplets, but nano- to microliter droplets still need to be employed in cases where target molecules with very low concentration need to be detected[37-38]. Passive mixing strategies employed in previous works may not be practical in these large droplets since the mixing channel need to be very long[30], thus increasing the device size. In addition, chaotic advection may not enhance mixing in these long, plug-shaped droplets because the striation is only formed in the front half of the plug[29]. Therefore, alternative mixing strategies need to be explored for applications involving large droplets.

In this chapter, we present studies on droplet merging and mixing in a microfluidic platform for multi-step biochemical reactions. Submicroliter-sized droplets generated separately from three different channels can easily merge together in a central chamber. The chamber also serves as a compartment for conducting mixing and reactions. Different mixing strategies have been studied to enhance mixing in the merged droplet. Furthermore, we demonstrate the application of this droplet-based platform by performing nested TaqMan® PCR, a two-step bioreaction, with on-chip droplet generation, merging and mixing.

Materials and Methods

Device fabrication

The fabrication procedure for the fluid network has been outlined in details elsewhere[39]. Briefly, a thin metal film (500Å Cr/ 2500Å Au) is deposited and patterned on a glass wafer. The glass wafer is then etched to the desired depth in 49% hydrofluoric acid (CMOS grade; J.T. Baker, Philipsburg, NJ). Next, the photoresist and the metal layer are removed. The glass wafer is then diced to obtain individual dies. The dies are coated with a 3μm thick layer of Parylene-C (PDS 1020 Labcoater, Speciality Coating Systems, IN) before bonded to the bottom dies.

Four sets of heaters and resistance temperature detectors (RTDs) on each die are fabricated on a silicon wafer with a 5000Å thick silicon oxide layer. Firstly, photoresist is patterned on the silicon wafer using photolithography. Next, 300Å Ti/ 1000Å Pt is evaporated on the silicon wafer. The wafer is then left in acetone (CMOS grade; J.T.

Baker, Philipsburg, NJ) to liftoff unwanted metal. The diced individual silicon dies are fixed on the custom designed printed circuit board (PCB, Advanced Circuits, Aurora, CO), and then wire bonded (Kulicke & Soffa 4124 Ball Bonder) using 1.0 mil gold wire. The assembled silicon die and PCB are also coated with a 3μm thick layer of Parylene-C. Finally, the glass and silicon dies are visually aligned and then bonded using UV curable optical glue.

Instrumentation

The setup for on-chip temperature control consists of two data acquisition (DAQ) boards (National instruments PCI 6031E and PCI-6704, Austin, TX), two connector blocks (National instruments SCB-100 and SCB-68, Austin, TX), a signal conditioning circuit, a DC power supply (B+K Precision Model 1760, Yorba Linda, CA), a computer and two LabVIEW programs (National instruments, Austin, TX). One LabVIEW program is used to calibrate the RTDs by recording the temperature-resistance data when the device is heated in a convection oven. The slope and intercept from a linear fit of the temperature and resistance data are read into the control algorithms that use a proportional-integral (PI) module to control temperature. The heaters are connected to the power supply through the signal conditioning circuit that boosts the supply voltage from the computer with an op-amp gain of 3. The precision of temperature control is ± 0.2^{o}C. During the experiments, the device is placed on a copper block that sits on a probe station with temperature maintained at 15^{o}C.

Lab air supply serves as the pneumatic source for driving the fluid flow and is controlled using electropneumatic regulators (VSO-EP or VSO-EV; Parker, Cleveland,

OH). Pressure or vacuum is applied through syringes connected to each port on the device. The Pulsing of pressure or vacuum is controlled by a set of three-way solenoid valves (Numatech, Wixom, MI). Opening and closing of the solenoid valves are operated through a relay board (Model ER-16; National Instruments, Austin, TX). Functioning of the relay board is controlled in conjunction with a Digital I/O card (National Instrument PCI-DIO-96, Austin, TX) by a LabVIEW program.

Measurement of micromixing

Aqueous solution with 1.4g/L fluorescein (Sigma Aldrich, St. Louis, MO) and colorless DI water are used to characterize mixing in the merged droplet. During the mixing process, in situ imaging is recorded using a digital camera (Nikon Coolpix 4500) with a capture rate of 30 frames/s. The captured RGB images are converted into grayscale images using Image J (NIH). The grayscale value of each pixel's intensity is processed using a program written in MATLAB (MathWorks, Natick, MA), and the standard deviation ($SD = \left\langle (I - \langle I \rangle)^2 \right\rangle^{1/2}$) of the droplet area is used to quantify the degree of mixing as described in previous work[40]. Due to the limitations in our imaging setup, the standard deviation for the unmixed and perfectly mixed cases is SD_1=0.385 and SD_2=0.1 (instead of the ideal value SD_1=0.5 and SD_2=0), respectively.

PCR amplification

The reaction mixture for regular TaqMan® PCR consists of λDNA template (Invitrogen, Carlsbad, CA) with the concentration ranging from 3.5ng/μL to 3.5×10^{-8}ng/μL, 0.2mM dNTPs, 10mM Tris-HCl (pH 8.3), 50mM KCl, 0.01mM EDTA, 3.5mM

$MgCl_2$, 0.9μM each primer, 0.25μM probe, 0.175units/μL AmpliTaq Gold® DNA polymerase (Applied Biosystems, Foster City, CA) and DI H_2O. The sequences of forward and reverse primers are 5'-CATCAAAGCCATGAACAAAGCA-3' and 5'-TCAGCAACCCCGGTATCAG-3', respectively. The sequence of probe is 5'6FAM-CCGCGCTGGATGA-3'MGBNFQA. The size of the target product is 56bp. The thermal cycling protocol used in the on-chip droplet-based reaction consists of 95°C for 9min, followed by 16-45 cycles of 95°C for 9s and 60°C for 30s. PCR grade mineral oil (Sigma Aldrich, St. Louis, MO) is used as the continuous oil phase.

The reaction mixture for the first-run amplification of nested TaqMan® PCR involves a new set of primers with the concentration of 0.3μM each. All the other reagents have the same concentrations as in the mixture of regular TaqMan® PCR, except no probe included. The sequences of the new forward and reverse primers are 5'-AACCGACATGTTGATTTCCT-3' and 5'-AACCTGACTGTTCGATATATTCACT-3', respectively. The product from the first-run amplification is 112bp. The thermal cycling protocol used in the on-chip droplet-based reaction consists of 95°C for 9min, followed by 15 cycles of 95°C for 5s, 50°C for 15s and 72°C for 20s. For the second-run amplification with the TaqMan® probe, the composition of the reaction mixture and the thermal cycling protocol are the same as the regular TaqMan® PCR, except no template DNA included.

Fluorescence detection of the reaction droplet

The fluorescence of the reaction droplet is monitored using an inverted fluorescence microscope (Nikon Eclipse TE2000-U) with a 2x objective (Nikon). An X-

cite Series 120 lamp (EXFO Life Science Divisions, Ontario, Canada) with FITC filter is used as the excitation source. The fluorescence images are captured using a digital CCD camera (Photometrics Cascade 512F; Roper Scientific, Tucson AZ) with a 500ms exposure time. The relative fluorescence intensity is used to quantify the amplification yield in the droplet, which is calculated by scaling the fluorescence intensity of the droplet by that of the reference area on the device. Data analysis is done by MetaVue Software.

Results and Discussions

Droplet generation and merging

The device design for droplet generation and merging is shown in Figure 5.1(a). There are three identical droplet-generation components each consisting of slanted (45-degree) T-junctions followed by neck regions. Nanoliter-sized droplets with different size and content can be produced from the three components using the sequential injection mode[41]. To do this, the entire fluid network is filled with mineral oil by capillary force, and then pulsed pressure (1psig, on for 15ms, off for 500ms) is applied to the aqueous phase (Figure 5.1(b)). Once the oil/aqueous interface reaches the junction, pulsed pressure is applied to both phases to flow the aqueous phase towards the chamber instead of the oil reservoir (Figure 5.1(c)). When the interface reaches the desired position, pressure is only applied to the oil phase to break the aqueous phase into droplet and push the droplet into the chamber while simultaneously pushing the rest of the aqueous phase back to the reservoir (Figure 5.1(d)-(e)).

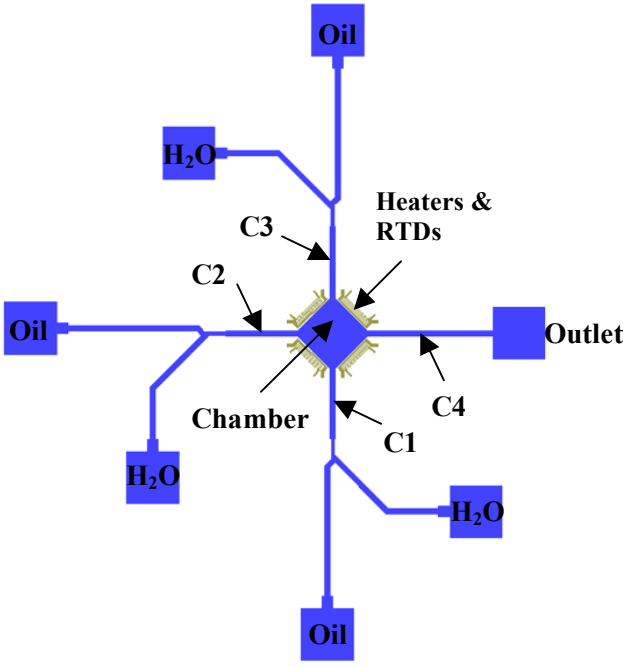

(a)

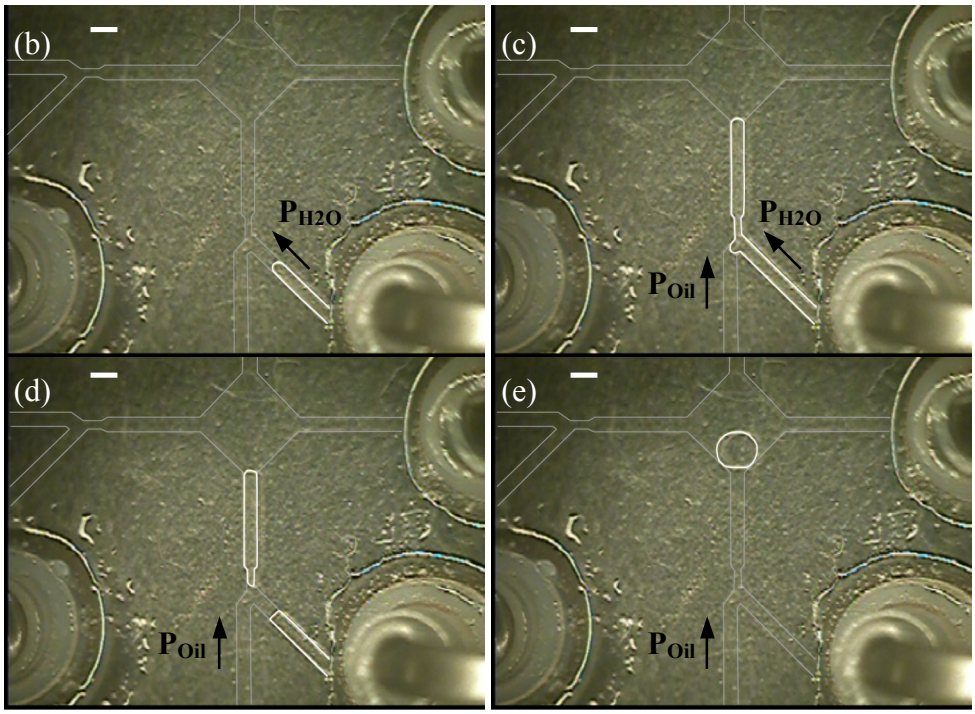

Figure 5.1 (a) Schematic of the device design. The four channels connected to the chamber are labeled as C1, C2, C3 and C4, respectively. The four sets of heaters and RTDs are positioned along the edges of the chamber. (b)-(e) Generation of one droplet. The scale bar represents 800μm.

After the droplets are generated, they can be trapped and merged in the central chamber connected to the three droplet generation channel (C1-C3). As shown in Figure 5.2, once the first droplet (D1) enters the middle chamber, the pressure that drives the flow is stopped and the surface tension keeps the droplet inside the chamber because of the expanded geometry. Then D1 remains in the chamber and "waits" for the second droplet (D2) to enter the chamber. During the generation and motion of D2, the unblocked channels (C3 and C4) serves as fluid bypass channels to allow the continuous oil phase to flow through. The drainage of the continuous oil phase guides D2 to merge with D1 into a larger droplet (D12). The third droplet (D3) can be generated and merge with D12 using the same method.

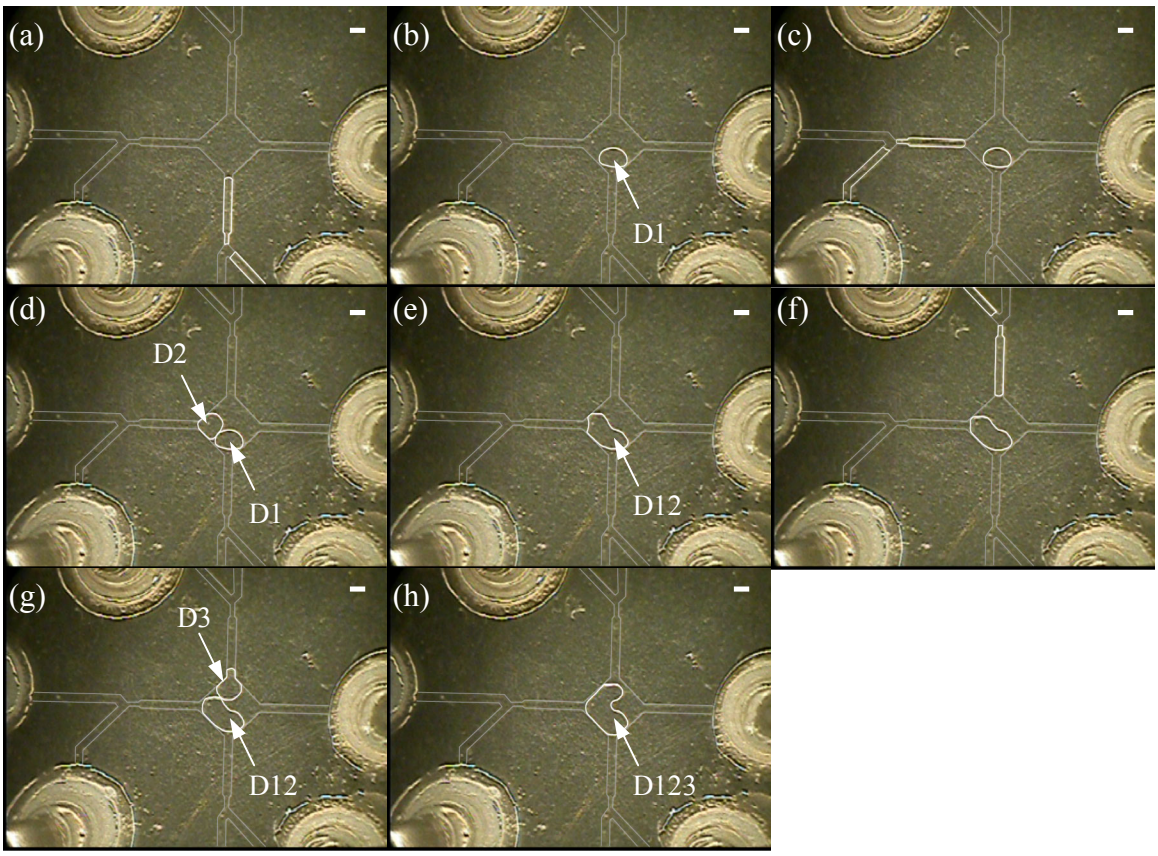

Figure 5.2 Generation and merging of droplets (D1, D2, and D3). The scale bar represents 800μm.

There are several advantages in using this device design for applications involving large (nano- to microliter-scale) droplets. The chamber serves as a compartment not only for entrapping and merging droplets, but also for droplet mixing and reaction. This single multi-functional chamber design offers advantages in conservation of device space. Moreover, since the droplet-generation components are connected to the chamber separately, the droplets can be produced either sequentially, as shown above, or synchronously, depending on the application. For example, to carry out a multi-step reaction, reagents for different steps need to be kept separate until the proper conditions are available, so the droplets need to be generated one by one. This design can also be used for small monodispersed droplet-based applications such as high throughput screening, with multiple droplets containing different reactants from and trapped in the same chamber.

Mixing in the merged droplet

Three major approaches can be used to homogenize a droplet: diffusive mixing, passive mixing and active mixing. Mixing purely by diffusion in the submicroliter merged droplet is excessively slow. As shown in Figure 5.3, it took about 10 min to homogenize a merged droplet with a volume of ~200nL purely by diffusion. In this experiment, fluorescein, with a diffusion coefficient on the order of 10^{-5} cm^2/s, was used to quantify the mixing. Some reagent molecules (*e.g.*, protein and long-strand DNA) have diffusion coefficients lower than fluorescein by an order of magnitude or more and would thus take even longer to diffusively mix.

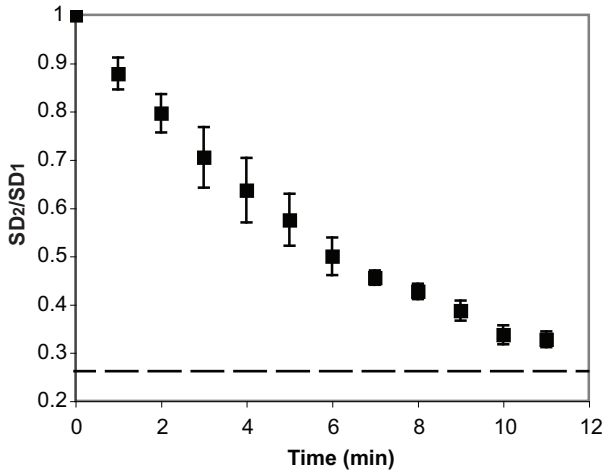

Figure 5.3 Evolution of the standard deviation (SD) of the merged droplet versus time during diffusive mixing. SD_1 is the standard deviation just after the droplet merging. SD_2 is the standard deviation during mixing. The dashed line (SD_2/SD_1=0.259) represents the ratio of the standard deviations between off-chip perfectly mixed and unmixed cases. The error bar represents the standard deviation.

Mixing in the droplet can be enhanced by applying pressure through the oil phase in the four channels (C1-C4) while the droplet remains in the chamber. As above-mentioned, the merged droplet tends to remain inside the expanded chamber because of surface tension. The oil film between the droplet and the top/bottom chamber walls is very thin due to the small chamber depth, so the applied pressure mostly drives the oil phase around the unconfined sides of the droplet. The oil flow shears the oil/water interface and causes internal recirculation in the droplet that results in mixing. This mixing strategy is similar to using internal recirculation by moving the droplet through a channel. When we start applying pressure through the oil phase, the merged droplet deforms to minimize its surface-to-volume ratio and internal recirculation inside the droplet is observed. One thing to be pointed out is that mixing mainly happened in the x-y plane, because the solutes were originally distributed uniformly along the z direction,

and the thin oil film between the droplet and the top/bottom chamber walls suppressed shear on those surface and the internal recirculation in that direction.

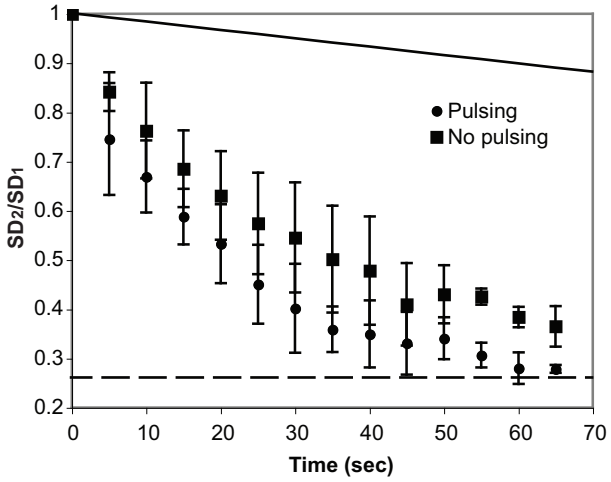

Figure 5.4 Evolution of the standard deviation (SD) of the merged droplet versus time during mixing with the droplet remaining in the chamber. ● Mixing with pulsed pressure; ■ mixing with continuous pressure. The solid line represents the case of diffusive mixing. SD_1, SD_2 and the dashed line are defined in the caption of Fig.2. The error bar represents the standard deviation.

We have quantified the mixing in the merged droplet with pressure applied in pulsing and continuous modes (Figure 5.4). The results show that the droplet can be homogenized within ~65 sec using both modes, which is about one tenth the mixing time by diffusion. The results also indicate that mixing using pulsed pressure is slightly faster than using continuous pressure. The reason for this could be related to the presence of non-circulating or static points (*i.e.*, the "dead zones") inside the droplet, especially in large sized droplets[19]. The recirculation loop cannot reach the "dead zones", so these areas can only mix with the rest of the fluid in the droplet by diffusion. While applying pressure continuously, the recirculation loops and the "dead zones" are relatively constant. In contrast, with pulsed pressure, some chaotic fluid motion may be introduced

into droplet, allowing the convective mixing to take place between the loops and the "dead zones".

Another mixing strategy is moving the merged droplet back and forth from the chamber to the channel. This strategy is similar to the electrically controlled active mixing achieved with droplet oscillating between electrodes in an EWOD device[33]. As shown in Figure 5.5, mixing can be completed much faster (<10 sec), compared to mixing with the droplet in the chamber. The result also indicates that the pulsing parameters for the applied pressure in both directions (Table 5.1) needs to be balanced in order to obtain efficient mixing. For pressure with the same "ON" time in each pulse, the "OFF" time had no significant effect on the mixing efficiency. One thing to be pointed out is that there was a time lag between each pulsing cycle due to the processing speed of the computer program. In addition, although stronger pressure could enhance mixing, if the pressure was too strong (*i.e.*, the pulsing "ON" time is too long and the pulsing frequency is too high), the droplet became unstable and then split while moving back and forth (data not shown).

Table 5.1 The pulsing parameters for the applied pressure during mixing with bidirectional droplet motion. ◆, ■, ▲ and ● correspond to the markers in Figure 5.5.

Pulsing Cycle	Out			In		
	On (ms)	Off (ms)	Times	On (ms)	Off (ms)	Times
◆	20	200	8	40	200	4
■	30	200	4	40	200	4
▲	40	200	4	40	200	4
●	40	100	4	40	100	4

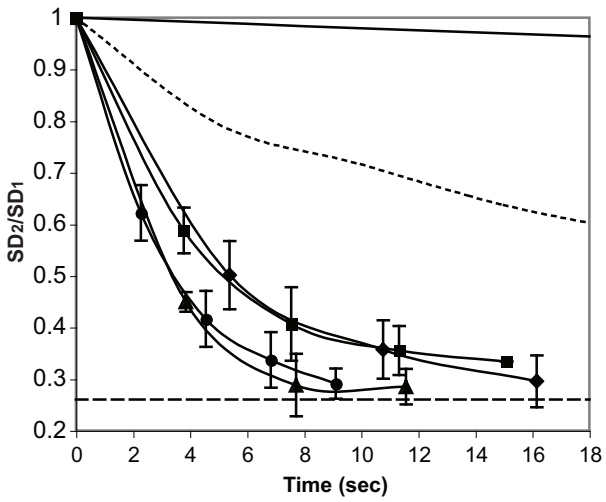

Figure 5.5 Evolution of the standard deviation (SD) of the merged droplet versus time during mixing with the bidirectional droplet motion. The solid line and dotted line represent the cases of diffusive mixing and mixing with droplet in the chamber, respectively. SD_1, SD_2 and the dashed line are defined in the caption of Fig.2. Each data point was obtained just before the next pulsing cycle. The pulsing parameters are shown in Table 1. Surfactant (Span 80, 0.3% v/v) was added in the oil phase to facilitate the droplet motion without leaving residues on the channel and chamber walls. The error bar represents the standard deviation.

The bidirectional droplet motion can enhance mixing by increasing the interfacial area between the two miscible fluids. The interfacial area is extended not only by inducing the internal recirculation, but also by stretching the droplet into a long plug while moving it into the channel. For large solute molecules, mixing in the droplet is more likely dispersion-dominated because of the low diffusivity ($D \sim 10^{-6}$-10^{-9} cm^2s^{-1}). Therefore, a long displacement distance is required to complete the mixing[30-31]. With the bidirectional droplet motion, the long displacement distance can be achieved within a limited region instead of through a long channel, thus offering an advantage in conservation of device space. In addition, for convection dominated mixing in our device, the internal recirculation induced by motion in one direction will not be completely reset to the original state when the droplet moves in the opposite direction, because the

chamber and channel have different geometry. Therefore, unlike in a uniform channel[30], the bidirectional motion between the chamber and channel works for mixing solutes with low molecular weight (*e.g.*, D ~ 10^{-5} cm^2s^{-1}) even when the mixing is dominated by convection.

Two-step bioreaction (nested TaqMan® PCR) in droplets

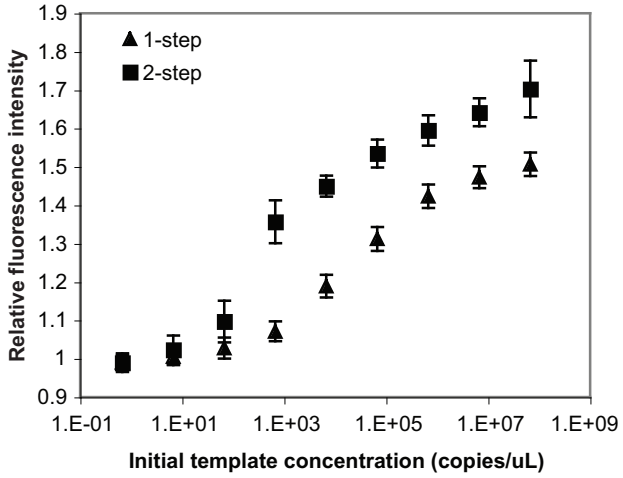

Figure 5.6 Performance of regular TaqMan® PCR (▲) and nested TaqMan® PCR (■) in a thermal cycler. The regular TaqMan® PCR was carried out for 31 cycles. The two steps in nested TaqMan® PCR were carried out for 15 and 16 cycles, respectively. The initial concentration of template λDNA ranges from 3.5ng/μL (~$6.69x10^7$copies/μL) to $3.5x10^{-8}$ng/μL (~0.669copies/μL). The reaction volume is 10μL. The error bar represents the standard deviation.

A two-step bioreaction – nested TaqMan® PCR of λDNA – has been chosen to demonstrate the utility of this droplet-based microfluidic platform. Nested TaqMan® PCR involves two successive runs of amplification: the first run is a regular PCR and the second one is a TaqMan® PCR that amplifies a secondary fragment within the first run product. With the two amplification steps, nested TaqMan® PCR can increase the reaction sensitivity and specificity of the overall amplification. The results of both regular TaqMan® PCR and nested TaqMan® PCR conducted in a thermal cycler were compared

in Figure 5.6. With the same initial concentration of template DNA and the same total number of temperature cycles, nested TaqMan® PCR not only increased the fluorescence intensity (*i.e.*, the amplification yield), but also detected target molecules with lower copy number (*e.g.*, 10^2 copies/μL). In contrast, regular TaqMan® PCR was only able to detect template DNA with concentration higher than 10^3 copies/μL.

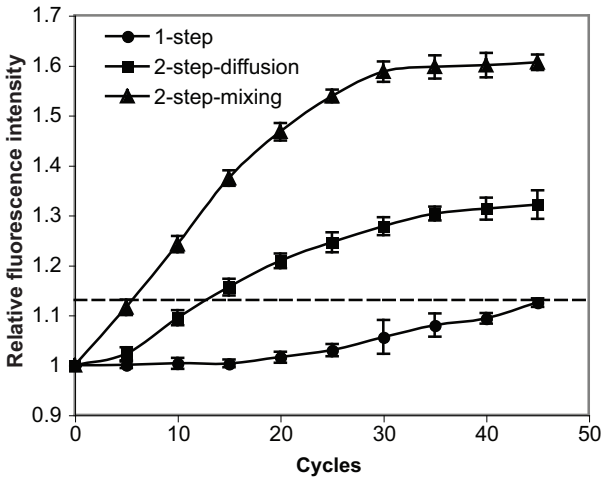

(a)

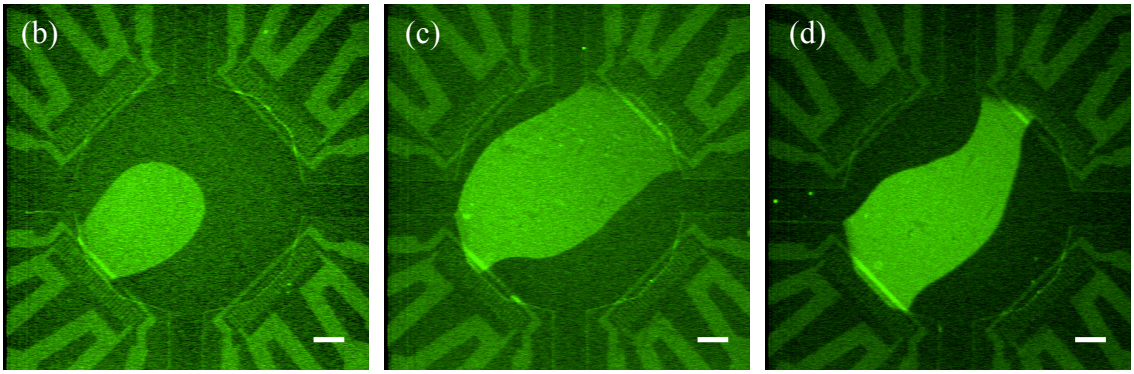

Figure 5.7 (a) Performance of the droplet-based regular TaqMan® PCR (▲) and the nested TaqMan® PCR in a well-mixed droplet (■) and diffusively mixed droplet (●). The dashed line represents the cycle threshold (Ct=1.13). (b) Fluorescent image after 31 cycles of regular TaqMan® PCR in a droplet. (c)-(d) Fluorescent images of nested TaqMan® PCR in a well-mixed and diffusively mixed droplet, respectively. The two steps in nested TaqMan® PCR were carried out for 15 and 16 cycles, respectively. The initial concentration of template λDNA is 3.5×10^{-5}ng/μL (~6.69×10^2copies/μL). The error bar represents the standard deviation. The scale bar represents 400μm.

Nested TaqMan® PCR has also been successfully performed in our droplet-based microsystem. In this experiment, 15 cycles of regular PCR was conducted in the droplet containing the reaction solution for the first step. Then, another droplet with the same size containing the reagents for the second step was generated, and merged with the first droplet in the chamber. The fluorescence intensity of the merged droplet was monitored in real time through 45 temperature cycles. The results in Figure 5.7 show that the amplification yield in the merged droplet with sufficient mixing is significantly higher than that in the droplet of regular TaqMan® PCR and also higher than that in the merged droplet mixed only by diffusion. Also, the two-step amplification in the well-mixed droplet is comparable to the off-chip result. The cycle threshold obtained in the well-mixed merged droplet is ~40 cycles earlier than that obtained in the droplet of regular TaqMan® PCR, and ~6 cycles earlier than that obtained in the merged droplet mixed only by diffusion. Therefore, with sufficient on-chip mixing, nested TaqMan® PCR in the droplet-based microsystem can offer faster and more sensitive analysis than regular TaqMan® PCR.

Conclusions

We have implemented the generation, merging and mixing of submicroliter-sized droplets on a droplet-based microfluidic platform. In the platform the chamber connected to the three identical droplet-generation channels serves as a compartment not only for merging droplets, but also for carrying out mixing and reaction in the merged droplets. This single multi-functional chamber design offers advantages in conservation of device

area and substrate cost. Mixing in the droplet has been characterized with the droplet either staying inside the chamber or moving bidirectionally between the chamber and channel. Both mixing strategies have advantages and disadvantages in practical use. Mixing with the droplet staying in the chamber does not take any additional space. The mixing time is rather long, but it is acceptable for reactions with relatively long reaction time (*e.g.*, DNA amplification). Mixing with the bidirectional droplet motion is much faster, but it requires space in both the chamber and channel, limiting the device flexibility. This mixing strategy is also not amenable for mixing aqueous solution containing surfactant because the interfacial tension will be further reduced with the surfactant already in the oil phase thus significantly reducing the droplet stability. We have also successfully applied this droplet-based platform to a two-step thermal cycled bioreaction (nested TaqMan® PCR). Our platform can certainly be extended to applications in other multi-step reactions and assays.

References

1. N. R. Beer, B. J. Hindson, E. K. Wheeler, S. B. Hall, K. A. Rose, I. M. Kennedy and B. W. Colston, *Anal. Chem.*, 2007, **79**, 8471-8475.
2. N. R. Beer, E. K. Wheeler, L. Lee-Houghton, N. Watkins, S. Nasarabadi, N. Hebert, P. Leung, D. W. Arnold, C. G. Bailey and B. W. Colston, *Anal. Chem.*, 2008, **80**, 1854-1858.
3. M. Chabert and J.-L. Viovy, *Proc. Natl. Acad. Sci.*, 2008, **105**, 3191-3196.
4. A. Huebner, M. Srisa-Art, D. Holt, C. Abell, F. Hollfelder, A. J. deMello and J. B. Edel, *Chem. Commun.*, 2007, **12**, 1218-1220.
5. L.-H. Hung, K. M. Choi, W.-Y. Tseng, Y.-C. Tan, K. J. Shea and A. P. Lee, *Lab Chip*, 2006, **6**, 174-178.
6. P. Kumaresan, C. J. Yang, S. A. Cronier, R. G. Blazej and R. A. Mathies, *Anal. Chem.*, 2008, **80**, 3522-3529.
7. S. Mohr, Y.-H. Zhang, A. Macaskill, P. J. R. Day, R. W. Barber, N. J. Goddard, D. R. Emerson and P. R. Fielden, *Microfluid Nanofluid*, 2007, **3**, 611-621.
8. T. Ohashi, H. Kuyama, N. Hanafusa and Y. Togawa, *Biomed Microdevices*, 2007, **9**, 695-702.
9. Y. Schaerli, R. C. Wootton, T. Robinson, V. Stein, C. Dunsby, M. A. A. Neil, P. M. W. French, A. J. deMello, C. Abell and F. Hollfelder, *Anal. Chem.*, 2009, **81**, 302-306.
10. M. Srisa-Art, A. J. deMello and J. B. Edel, *Anal. Chem.*, 2007, **79**, 6682-6689.

11. B. Zheng, J. D. Tice, S. Roach and R. F. Ismagilov, *Angew. Chem. Int. Ed.*, 2004, **43**, 2508-2511.

12. S. L. Anna, N. Bontoux and H. A. Stone, *Appl. Phys. Lett.*, 2003, **82**, 364-366.

13. T. Thorsen, R. W. Roberts, F. H. Arnold and S. R. Quake, *Phys. Rev. Lett.*, 2001, **86**, 4163-4166.

14. S. K. Cho, H. Moon and C.-J. Kim, *J. Microelectromech. Syst.*, 2003, **12**, 70-80.

15. M. G. Pollack, R. B. Fair and A. D. Shenderov, *Appl. Phys. Lett.*, 2000, **77**, 1725-1726.

16. M. G. Pollack, A. D. Shenderov and R. B. Fair, *Lab Chip*, 2002, **2**, 96-101.

17. D. R. Link, S. L. Anna, D. A. Weitz and H. A. Stone, *Phys. Rev. Lett.*, 2004, **92**, 054503-1-054503-4.

18. X. Niu, S. Gulati, J. B. Edel and A. J. deMello, *Lab Chip*, 2008, **8**, 1837-1841.

19. F. Sarrazin, L. Prat, N. D. Miceli, G. Cristobal, D. R. Link and D. A. Weitz, *Chem. Eng. Sci.*, 2007, **62**, 1042-1048.

20. Y.-C. Tan, Y. L. Ho and A. P. Lee, *Microfluid Nanofluid*, 2007, **3**, 495-499.

21. T. H. Ting, Y. F. Yap, N.-T. Nguyen, T. N. Wong, J. C. K. Chai and L. Yobas, *Appl. Phys. Lett.*, 2006, **89**, 234101-234103.

22. E. Um and J.-K. Park, *Lab Chip*, 2009, **9**, 207-212.

23. R. Ahmed and T. B. Jones, *J. Electrost.*, 2006, **64**, 543-549.

24. T. B. Jones, *J. Electrost.*, 2001, **51-52**, 290-299.

25. Z. Guttenberg, H. Müller, H. Habermüller, A. Geisbauer, J. Pipper, J. Felbel, M. Kielpinski, J. Scriba and A. Wixforth, *Lab Chip*, 2005, **5**, 308-317.

26. T. Franke, A. R. Abate, D. A. Weitz and A. Wixforth, *Lab Chip*, 2009, **9**, 2625-2627.

27. U. Lehmann, C. Vandevyver, V. K. Parashar and M. A. M. Gijs, *Angew. Chem. Int. Ed.*, 2006, **45**, 3062-3067.

28. J. Pipper, M. Inoue, L. F.-P. Ng, P. Neuzil, Y. Zhang and L. Novak, *Nat. Med.*, 2007, **13**, 1259-1263.

29. M. R. Bringer, C. J. Gerdts, H. Song, J. D. Tice and R. F. Ismagilov, *Phil. Trans. R. Soc. Lond. A*, 2004, **362**, 1087-1104.

30. K. Handique and M. A. Burns, *J. Micromech. Microeng.*, 2001, **11**, 548-554.

31. M. Rhee and M. A. Burns, *Langmuir*, 2008, **24**, 590-601.

32. H. Song, M. R. Bringer, J. D. Tice and C. J. Gerdts, *Appl. Phys. Lett.*, 2003, **83**, 4664-4666.

33. P. Paik, V. K. Pamula, M. G. Pollack and R. B. Fair, *Lab Chip*, 2003, **3**, 28-33.

34. L. Frenz, A. E. Harrak, M. Pauly, S. Bégin-Colin, A. D. Griffiths and J.-C. Baret, *Angew. Chem. Int. Ed.*, 2008, **47**, 6817-6820.

35. V. Srinivasan, V. K. Pamula and R.B. Fair, *Lab Chip*, 2004, **4**, 310-315.

36. I. Shestopalov, J. D. Tice and R. F. Ismagilov, *Lab Chip*, 2004, **4**, 316-321.

37. V. Avettand-Fènoël, M.-L. Chaix, S. Blanche, M. Burgard, C. Floch, K. Toure, M.-C. Allemon, J. Warszawski and C. Rouzioux, *J. Med. Virol.*, 2009, **81**, 217-223

38. S. Sivapalasingam, U. Patel, V. Itri, M. Laverty, K. Mandaliya, F. Valentine and S. Essajee, *J. Trop. Pediatrics*, 2007, **53**, 355-358.

39. R. Pal, M. Yang, R. Lin, B. N. Johnson, N. Srivastava, S. Z. Razzacki, K. J. Chomistek, D. Heldsinger, R. M. Haque, V. M. Ugaz, P. Thwar, Z. Chen, K. Alfano, M. Yim, M. Krishnan, A. O. Fuller, R. G. Larson, D. T. Burke and M. A. Burns, *Lab Chip*, 2005, **5**, 1024-1032.

40. S.-J. Kim, F. Wang, M. A. Burns and K. Kurabayashi, *Anal. Chem.*, 2009, **81**, 4510-4516.

41. F. Wang and M. A. Burns, *Biomed Microdevices*, 2009, **11**, 1071-1080.

CHAPTER 6

CONCLUSIONS AND FUTURE WORK

Conclusions

The objective of this dissertation is to investigate and develop techniques to improve the performance of biochemical reactions and simplify the fabrication and operation of the microreaction systems. Three valveless strategies were first developed to reduce the evaporation loss during thermal bioreactions such as PCR in air-liquid (*i.e.*, single-liquid-phase) based microdevices. Employing two immiscible liquid phases (*i.e.*, aqueous-in-oil droplets), a microfluidic platform with much simpler fabrication was then used to carry out PCR with no evaporation loss. Performance of PCR was also characterized in the droplet-based microdevice. Furthermore, the operation of the droplet-based microsystem, including droplet generation and positioning was automated relying on the pneumatic feedback control by electronic sensing, to improve the system controllability and efficiency as well as simplify the system setup. Finally, the droplet-based microfluidic platform was used to perform droplet generation, merging and mixing for multi-step biochemical reactions.

Preventing evaporative sample loss during thermal bioreactions is one of the critical issues especially while carrying out the reaction in microdevices. The most

common solution is using sealing agents or microvalves to physically seal the reaction chamber. Relying on the principle of vapor diffusion-limited evaporation, evaporation loss can be reduced without sealing agents and microvalves, thus simplifying the fabrication and fluidic handling of PCR microdevices. Adding long narrow diffusion channels on both sides of the reaction region can significantly slow down the vapor diffusion and thus the evaporation at the PCR solution meniscus. Evaporation can be further suppressed by reducing the driving force for liquid evaporation: decreasing the interfacial temperature by thermal isolation technique using silicon back etching and reducing the vapor concentration gradient by replenishing water vapor into the diffusion channels. The combination of long vapor diffusion path with thermal isolation or vapor replenishment techniques can limit the sample evaporative loss to approximately 1% of the reaction content. Eliminating microvalves, the PCR component can be readily integrated into more advanced microfluidic DNA analysis systems.

With oil surrounding the aqueous reaction solution, the multi-liquid-phase (droplet-based) microfluidics provides a platform with even simpler fabrication for preventing evaporation loss, although issues related to the existence of a second liquid phase may also be introduced into the microsystem. To optimize the design and operation of the droplet-based bioreaction microsystem, we characterized the performance of droplet-based PCR in a microdevice that can reproducibly generate droplets with a volume range of 5-250nL. The existence of continuous oil phase completely prevents the evaporation loss, thus significantly simplifying the fabrication and operation of the microsystem since no additional components are needed. Our characterization studies on polymerase concentration and droplet size indicate that there is still reagent loss possibly

due to adsorption. In the droplet-based microsystems, besides adsorption on the oil/aqueous interface, there could also be adsorption on the channel surface if the oil phase could not wet the surface very well or the thin oil film could not stay stable during thermal cycling. With the optimized reaction parameters including the reagent concentrations and hold time, the droplet-based PCR shows amplification efficiency comparable to the benchtop reactions with half of the benchtop reaction time. Including FRET probes in the reaction mixture, the droplet-based PCR provides rapid detection (*i.e.*, a cycle threshold of ~10 cycles earlier than the benchtop reactions) of template concentration within a wide range of 10^3~10^7 copies/μL.

To further improve the operation efficiency and make the microsystem more user-friendly towards the point-of-care applications, on-chip electronic sensing was used to track the oil/aqueous interface in real time, and the droplet generation and positioning were automated by controlling the pneumatic supply for the fluid network using the sensing signals. We can obtain digital and analog signals depending on the arrangement of the electronic sensors. Digital sensing was employed for automatically generating four different sized droplets. The actual droplet size is very close to the designed droplet size with a standard deviation less than 3% of the droplet size. This automation can generate the droplets 5 times faster than in manual operation. During automated droplet positioning with digital sensing, droplets tend to oscillate between monitored sensors since the pressure is also controlled digitally. This oscillation can favor the mixing (especially when the mixing is Taylor dispersion dominated) in the droplets. With analog sensing, the positioning can be conducted more precisely using more sophisticated feedback control modules (*e.g.*, PI control), but larger exposed area of the electrodes

could inhibit the bioreactions. The size of the droplets that can be automatically operated in this microsystem is also limited by the fabrication capability for the electrodes. Since all the droplet operations are controlled through a computer program, a user without any professional training should be able to operate the system. In addition, cumbersome optical instruments can be eliminated, saving the system manufacture cost and making it easier to package the entire system into a portable point-of-care device.

Compared to the single-liquid-phase-based microsystem, fluidic handing is much easier and controllable in the droplet-based microsystem. Relying on the droplet manipulations such as merging and mixing, the droplet-based microsystem provide an ideal platform for performing more complex analyses (*e.g.*, analysis that includes multi-step reactions and requires controllable addition of reagents). We used a droplet-based microdevice to generate and merge submicroliter-sized droplets, and also investigated three strategies for mixing the merged droplet: pure diffusion, flow around the stationary droplet and bidirectional droplet motion. The latter two strategies offer much faster mixing (1 min and 10 sec, respectively) than pure diffusion (10 min). Mixing by the bidirectional droplet motion can be even faster (less than one second) if not limited by the computer processing speed. However, this mixing method is not amenable to mix aqueous solution containing surfactant and does require additional space in the microdevice, unlike mixing with the stationary droplet. This droplet-based microplatform was then applied for performing a two-step thermalcycled bioreaction, nested TaqMan® PCR. With the same concentration of template DNA, nested TaqMan® PCR in a well-mixed merged droplet provides much faster detection than the droplet-based single-step TaqMan® PCR, and also than the nested TaqMan® PCR in the diffusively mixed merged

droplet. This droplet-based microplatform can certainly be extended to other multi-step DNA analyses such as PCR-restriction fragment length polymorphism (PCR-RFLP) and ligation detection reaction (LDR).

Future work

The studies conducted in this dissertation raised issues worthy of further investigation and research in the following three aspects: (1) effects of different types of adsorptions and the droplet size on the reagent loss from the aqueous phase; (2) automation of the droplet operations in the multi-step bioreaction microsystem; (3) further integration of biochemical reactions in the droplet-based DNA analysis microsystem.

Effects of adsorption and droplet size

One of the proposed advantages for performing biochemical reactions in the droplet-based microsystem is that the thin oil film between the droplet and the channel surface could prevent the surface adsorption that commonly exists in the single-liquid-phase-based microsystems. However, our preliminary results in Chapter 3 and other previous work[1] indicate that there is still reagent loss from aqueous phase possibly due to adsorption, because a higher polymerase concentration is required to ensure the reaction efficiency and the fluorescence intensity in the reaction droplet decreases with decreasing droplet size (*i.e.*, increasing total surface-to-volume ratio (S_T/V)). There are probably two types of adsorptions in the droplet-based systems: adsorption on the oil/aqueous

interface and adsorption on the channel surface. Moreover, the oil/aqueous interface-to-volume ratio (S_i/V) and the channel surface-to-volume ratio (S_w/V) are strongly associated with the droplet size and shape.

The future work could focus on understanding the effects of different types of adsorptions on the reagent loss and the relationship between these effects and the droplet size. Fluorescently labeled reagents in combination with confocal microscopy could be used to confirm the adsorption type by tracking the location of the labeled reagents. Since the partition of protein to the liquid-liquid interface reduces the surface tension, drop tensiometry could also be used to detect and quantify the adsorption at the interface[2,3]. Theoretical model could be built to predict the adsorption loss in the different droplet size and shape regimes (*i.e.*, sphere-, plug- or disc-shaped). Droplet-based PCR need to be further tested to determine the importance of different types of adsorptions in these different regimes.

The future works could also focus on preventing or reducing the adsorption. Oil-soluble surfactant with a neutral functional group (*e.g.*, oligoethylene glycol (OEG) that can resist protein adsorption could be used to prevent the adsorption at the liquid/liquid interface and maintain full enzymatic activity[4]. In the droplet-based system, the adsorption on the channel surface is most likely caused by the nonuniform and unstable wetting of the oil phase on the channel surface, while the wetting could be controlled by adding oil soluble surfactant. The adsorption on the channel surface could also be alleviated by surface treatment (*e.g.*, modification with functional groups) or dynamic passivation with adhesion proteins such as bovine serum albumin (BSA).

Automation of droplet-based multi-step bioreaction microsystem

Involvement of electronic-sensing-based automation can improve the efficiency of system operation, reduce the manufacture cost, and make the DNA analysis microsystem more amenable to portable, point-of-care diagnosis. In Chapter 4, we have presented an automated droplet-based microsystem for carrying out single-step biochemical reactions. In the future work, the similar automation scheme could be extended to multi-step bioreaction microsystems.

Comparing to the previous automated droplet-based microsystem, the additional automation to be achieved in the multi-step bioreaction microsystem is the triggering of pneumatic control for droplet mixing. Therefore, major efforts will be spent on the detection of the droplet merging and the automation of pneumatic control for droplet mixing. The impedance based electronic sensing method used in Chapter 4 may not be sensitive enough for detecting the droplet merging. Alternative sensing strategies such as electric capacitance-based method could be used. Although the data acquisition and processing for the capacitance-based sensing may be more complex, the electrodes could be covered by the dielectric layer and the inhibition caused by the exposed electrodes would be eliminated. Moreover, the arrangement of electrodes may need to be optimized to minimize the potential cross talk among the electronic sensors in different droplet-generation components.

Integrated droplet-based DNA analysis microsytem

The future work also includes employing the droplet-based microsystem for more complex DNA analyses, for example, ligation detection reaction (LDR). LDR involves

three biochemical reactions (PCR, protease digestion and ligation) and can be applied in multiplex analysis of single nucleotide polymorphisms (SNPs)[5]. LDR products are usually detected using gel electrophoresis or microarray[6,7]. Based on the work presented in this dissertation, the droplet-based microplatform has been ready for performing three-step thermal bioreactions. But the reaction parameters may need to be optimized to ensure the droplet-based reaction efficiency.

Sensitive detection methods also need to be developed to verify the reaction products. For example, fluorescence quenching effect could be used to in situ detect the products. In the ligation step of LDR, different pairs of oligos are added to detect specific SNPs. Labeling the paired oligos with reporter and quencher dye respectively, fluorescence intensity will decrease if the two oligos are ligated. Or we can detect the ligated products by detecting the increase of fluorescence intensity by adding molecular beacons after the ligation step. Another method could be extracting the products from the droplets for electrophoresis or hybridization based detection. A possible approach to extract the reaction products is using surface treatment such as hydrophilic patch to separate the aqueous phase from the oil phase.

The future work could also focus on developing DNA analysis microsystems by combining the droplet microfluidics with other techniques to improve the analysis integrity and sensitivity. For example, particles with certain coating or labeling can be encapsulated uniformly together with samples and reagents into individual droplets. These particles can be used for sample purification to extract concentrated template DNA, providing a simpler platform especially for integrated DNA analysis starting from raw clinic samples. They can also enable immobilization based reactions in the droplets,

and can be used for locally magnifying the product detection signal by trapping the products using specific binding. On the other hand, unlike flowing the particles continuously, the combination of droplets and particles avoids channel clogging and particle adhesion, and reduces the diffusion distances between particles and molecules in the reaction mixture so that the reaction or incubation time could be reduced without sacrificing the analysis efficiency.

References

1. N. R. Beer, B. J. Hindson, E. K. Wheeler, S. B. Hall, K. A. Rose, I. M. Kennedy and B. W. Colston, *Anal. Chem.*, 2007, **79**, 8471-8475.
2. C. J. Beverung, C. J. Radke and H. W. Blanch, *Biophy. Chem.*, 1999, **81**, 59-80.
3. L. S. Roach, H. Song and R. F. Ismagilov, *Anal. Chem.*, 2005, **77**, 785-796.
4. K. L. Prime and G. M. Whitesides, *Science*, 1991, **252**, 1164-1167.
5. F. Barany, *Proc. Natl. Acad. Sci. USA*, 1991, **88**, 189-193.
6. G. Thomas, R. Sinville, S. Sutton, H. Farquar, R. P. Hammer, S. A. Soper, Y.-W. Cheng, F. Barany, *Electrophoresis*, 2004, **25**, 1668-1667.
7. M. Hashimoto, M. L. Hupert, M. C. Murphy, S. A. Soper, *Anal. Chem.*, 2005, **77**, 3243-3255.